KLOE Note n^o 225
June 2, 2011

Measurement of $\sigma(e^+e^- \to \pi^+\pi^-)$ for $M^2_{\pi\pi}$ between 0.1 and 0.85 GeV^2 using the Initial State Radiation method with the KLOE detector

Paolo Beltrame[a,d], Achim Denig[a], Stefan E. Müller[a,e], Wolfgang Kluge[b], Federico Nguyen[c]

[a] *Institut für Kernphysik, Universität Mainz, Germany*
[b] *Institut für Experimentelle Kernphysik, Universität Karlsruhe, Germany*
[c] *Dipartimento di Fisica dell'Università "Roma Tre" e Sezione INFN, Rome, Italy*
[d] now at: *UCLA Physics and Astronomy Dept., Los Angeles, California 90095-1547, USA*
[e] now at: *KVI, Rijksuniversiteit Groningen, The Netherlands*

Abstract

The KLOE experiment at the ϕ-factory DAΦNE has measured the pion form factor in the range $0.1 < M^2_{\pi\pi} < 0.85$ GeV^2 for the squared invariant mass of the two-pion system $M^2_{\pi\pi}$ using events taken at $\sqrt{s} = 1$ GeV with a photon emitted in the initial state at large polar angle. This measurement extends the $M^2_{\pi\pi}$ region covered by previous KLOE ISR measurements down to the two-pion production threshold. It allows to compute the dipion contribution $\Delta a^{\pi\pi}_\mu$ to the anomaly of the muon magnetic moment $a_\mu = (g_\mu - 2)/2$. Our value of $\Delta a^{\pi\pi}_\mu = (478.5 \pm 2.0_{\mathrm{stat}} \pm 5.0_{\mathrm{syst}} \pm 4.5_{\mathrm{theo}}) \times 10^{-10}$ further confirms the discrepancy between the Standard Model evaluation for a_μ and the experimental value measured by the $(g_\mu - 2)$-collaboration at BNL.

Contents

1 Introduction

The anomaly of the magnetic moment of the muon, a_μ, is one of the best known quantities in particle physics. Recent theoretical evaluations [2, 3] find a discrepancy of 3 - 4 standard deviations from the value obtained from the $(g_\mu - 2)$ experiment at Brookhaven [1]. A large part of the uncertainty on the theoretical estimates comes from the leading order hadronic contribution $\Delta a_\mu^{\mathrm{had,lo}}$. This quantity is not calculable by perturbative QCD, but has to be evaluated with a dispersion integral using measured hadronic cross sections as input. The use of initial state radiation (ISR) allows to obtain these cross sections at particle factories operating at fixed energies [4]. The region below 1 GeV, which is accessible with the KLOE experiment in Frascati, is dominated by the $\pi^+\pi^-$ final state and contributes with $\sim 70\%$ to $\Delta a_\mu^{\mathrm{had,lo}}$, and $\sim 60\%$ to its uncertainty. Therefore, improved precision in the $\pi\pi$ cross section would result in a reduction of the uncertainty on the leading order hadronic contribution to a_μ, and in turn improve its Standard Model prediction.

The KLOE collaboration has already published two ISR measurements of the $\pi\pi$ cross section for $M^2_{\pi\pi}$ between 0.35 and 0.95 GeV^2 using data collected in 2001 [5] and 2002 [6]. The new measurement, discussed in the following, is based on a KLOE data set taken in 2006 for which the center-of-mass energy of the DAΦNE collider was set to $W \simeq 1$ GeV, 20 MeV below the ϕ resonance, and it uses different acceptance cuts for the radiated photons. While in previous KLOE results, the photon in the initial state has been required to be emitted at small polar angles respect to the beamline, and therefore escapes detection, in the measurement presented in this paper, we require the initial state photon to be detected by KLOE's electromagnetic calorimeter at large polar angles. This allows to extend the $M^2_{\pi\pi}$ region covered down to 0.1 GeV^2, close to the threshold for two-pion production.

2 Measurement of the cross section $e^+e^- \to \pi^+\pi^-$ with initial state radiation at DAΦNE

The KLOE experiment operates at the Frascati ϕ-factory DAΦNE, an e^+e^--collider with small crossing angle running mainly at a center-of-mass energy W equal to the ϕ-meson mass of $M_\phi \simeq 1020$ MeV. As a meson-factory, the center-of-mass energy of DAΦNE can be changed only little away from the ϕ-resonance energy, and scan measurements of hadronic cross sections over a wider energy range are not possible. Instead, one determines the cross section from events in which a photon emitted in the intial state from the electron or the positron reduces the energy available for hadron production in the collision. In the analyses performed at KLOE, one measures the differential cross section for $e^+e^- \to \pi^+\pi^-\gamma$ as a function of the $\pi^+\pi^-$ invariant mass, $M_{\pi\pi}$, for ISR events, and obtains the dipion cross section

$\sigma_{\pi\pi} \equiv \sigma(e^+e^- \to \pi^+\pi^-)$ from (see Ref. [7]):

$$\left.\frac{\mathrm{d}\sigma(ee \to \pi\pi\gamma)}{\mathrm{d}M^2_{\pi\pi}}\right|_{\mathrm{ISR}} = \frac{\sigma_{\pi\pi}(M^2_{\pi\pi})}{s}\ H(M^2_{\pi\pi}, s) \tag{1}$$

Eq. 1 defines the dimensionless "radiator function" H. It can be obtained from QED calculations and depends on the e^+e^- center-of-mass energy squared s. Final state radiation (FSR) terms are neglected in Eq. 1, but are taken into account properly in the analysis. The KLOE detector, used in the analyses and depicted in Fig. 1,

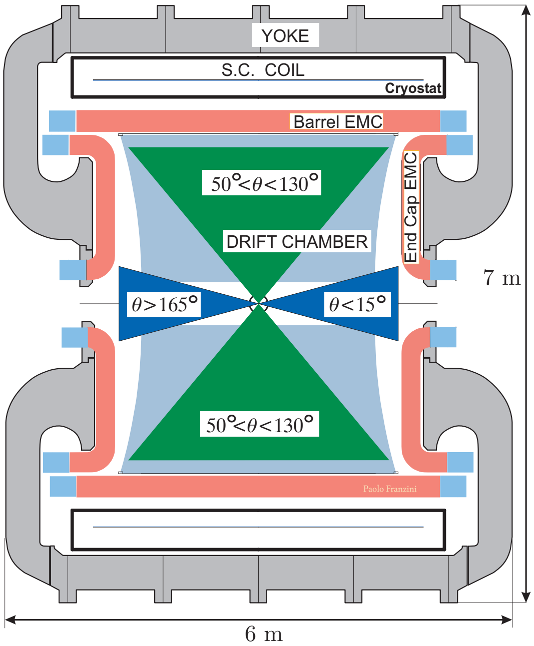

Figure 1: Vertical cross section in the $y - z$ plane of the KLOE detector, showing the small and large angle regions for photons and pions used in the different KLOE analyses.

consists of a cylindrical drift chamber (DC) [9] surrounded by an electromagnetic calorimeter (EMC) [10]. The drift chamber has a momentum resolution of $\sigma_{p_t}/p_t \sim$ 0.4% for tracks with polar angle $\theta > 45°$, and track points are measured with a resolution in r-ϕ of ~ 0.15 mm and ~ 2 mm in the z direction.[1] The calorimeter has an energy resolution of $\sigma_E/E \sim 5.7\%/\sqrt{E\ (\mathrm{GeV})}$ and an excellent time resolution of $\sigma_t \sim 54\ \mathrm{ps}/\sqrt{E\ (\mathrm{GeV})} \oplus 100$ ps, and energy deposits close in space and time are grouped together to form "clusters". A superconducting coil provides an axial magnetic field of 0.52 T along the z-axis.

The previous KLOE analyses [5, 6] used selection cuts in which photons are emitted within a cone of $\theta_\gamma < 15°$ around the beamline (narrow cones in Fig. 1) and the two charged pion tracks have $50° < \theta_\pi < 130°$ (wide cones in Fig. 1). In this configuration, the photon is not explicitly detected, its direction is reconstructed from the tracks' momenta by closing kinematics: $\vec{p}_\gamma \simeq \vec{p}_{\mathrm{miss}} = -(\vec{p}_{\pi^+} + \vec{p}_{\pi^-})$. While

[1]The angle bisector between the two colliding beams is taken as the z-axis of the KLOE coordinate system with incoming positrons going along positive values of z, the x-axis is horizontal, pointing to the center of the collider rings, while the y-axis is vertical, directed upwards.

these cuts guarantee a high statistics for ISR signal events, and a reduced contamination from the resonant process $e^+e^- \rightarrow \phi \rightarrow \pi^+\pi^-\pi^0$ in which the π^0 mimics the missing momentum of the photon(s) as well as from the final state radiation process $e^+e^- \rightarrow \pi^+\pi^-\gamma_{\rm FSR}$, a highly energetic photon emitted at small angle forces the pions also to be at small angles (and thus outside the selection cuts). This results in a kinematical suppression of events with $M^2_{\pi\pi} < 0.35$ GeV^2. To access the two-pion threshold, the new analysis presented in this paper requires events that are selected to have a photon detected in the calorimeter at large polar angles between $50° < \theta_\gamma < 130°$ (wide cones in Fig. 1). The pion tracks are also required to have $50° < \theta_\pi < 130°$. However, these acceptance cuts imply a reduction in statistics of about a factor 5, as well as an increase of events with final state radiation and from ϕ radiative decays compared to the small angle photon acceptance criterion. The uncertainty on the model dependence of the ϕ radiative decays to the scalars $f_0(980)$ and $f_0(600)$ together with $\phi \rightarrow \rho\pi \rightarrow (\pi\gamma)\pi$ has a strong impact on the measurement [11]. As a way out of this dilemma, the new analysis uses the data taken at a value of $\sqrt{s} = 1$ GeV, about 5 Γ_ϕ outside the narrow peak of the ϕ resonance ($\Gamma_\phi = 4.26 \pm 0.04$ MeV [12]). This reduces the effect due to contributions from $f_0\gamma$ and $\varrho\pi$ decays of the ϕ-meson to the level of some percent, allowing to extract the pion form factor with high precision.

3 Event selection

3.1 Preselection

The final data sample consists of $\int\mathcal{L}$dt=232.6 pb^{-1} of data taken in the years 2005/2006 at $\sqrt{s} \sim 1$ GeV, which have been preselected by a streaming algorithm using the following cuts [13]:

- at least 2 charged tracks with opposite charge and a point-of-closest approach (PCA) to the interaction point within a cylinder of
  - $|z_{\rm PCA}| < 15.$ cm
  - $r_{\rm PCA} = \sqrt{x^2_{\rm PCA} + y^2_{\rm PCA}} < 8.$ cm
- at least one combination of two selected tracks has to fulfill the following cuts on kinematical variables[2] [3]:
  - $150.$ MeV $< |\vec{p}_1| + |\vec{p}_2| < 1020.$ MeV
  - $(-220.$ MeV$) < \Delta M_{\rm M\mathit{iss}} < 120.$ MeV
  - $80.$ MeV $< M_{{\rm T}rk} < 400.$ MeV

[2]The kinematical variable $\Delta M_{\rm Miss}$ is represented by $\Delta M_{\rm Miss} = \sqrt{E^2_{\rm Miss} - |\vec{P}_{\rm Miss}|^2}$, where $E_{\rm Miss} = \sqrt{s} - \sqrt{|\vec{p}_1|^2 + m^2_\pi} - \sqrt{|\vec{p}_2|^2 + m^2_\pi}$ and $|\vec{P}_{\rm Miss}|^2 = (\vec{p}_\phi - (\vec{p}_1 + \vec{p}_2))^2$. $\Delta M_{\rm Miss}$ is peaked at the π^0 mass for $\pi^+\pi^-\pi^0$ events.

[3]The kinematical track mass variable $M_{{\rm T}rk}$ corresponds to the mass of the charged tracks under the hypothesis that the final state consists of two particles with the same mass and one photon. It is calculated from the reconstructed momenta $\vec{p}_+$, $\vec{p}_-$ and the center-of-mass energy $\sqrt{s}$ via $\left(\sqrt{s} - \sqrt{\vec{p}^2_+ + M^2_{{\rm T}rk}} - \sqrt{\vec{p}^2_- + M^2_{{\rm T}rk}}\right)^2 - (\vec{p}_+ + \vec{p}_-)^2 = 0.$

All momenta are evaluated at the "point of closest approach" (PCA) of each track, obtained by extrapolating the track inwards to the beam interaction point.

To ensure a good data quality and homogeneity of the data sample in use, data runs with integrated luminosity smaller than 25 nb^{-1} were excluded from the analysis.

3.2 Event selection

In addition to the preselection cuts described above, data events have to fulfill the following selection criteria:

- The trigger condition of two energy deposits larger than 50 MeV in two sectors of the barrel calorimeter must be fired by clusters associated to the charged tracks in the event [14] .
- Events have to pass the software L3 trigger implemented to preserve events rejected by the trigger veto for cosmic ray events.
- Events have to pass an offline reconstruction filter, which removes machine background events.
- The presence of two tracks with opposite sign curvature is required, crossing a cylinder centered around the interaction point with 8 cm radius and 14 cm length, and satisfying $50° < \theta_{\mathrm{tr}} < 130°$. Cuts on $|\vec{p}| > 200$ MeV and ($p_t > 160$ MeV or $|p_z| > 90$ MeV) are required to avoid spiralizing tracks in the drift chamber and ensure good reconstruction and efficiency.
- The detection of at least one photon with $50° < \theta_\gamma < 130°$ and $E_\gamma > 20$ MeV in the calorimeter.
- A particle identification method using a pseudo-likelihood estimator [15] for each track, based on time-of-flight and energy and shape of the calorimeter cluster associated to the track, is used to separate signal events from the high rate of radiative Bhabha events. Events with both tracks identified as electrons are rejected (see Fig. 3).
- The calorimeter clusters associated to both tracks must have a minimum distance of 90 cm to avoid a bias in the likelihood estimator.
- A cut in the kinematical variable M_{trk} [4](see Fig.2):
  - $M_{\mathrm{trk}} > 120$ MeV to reject $\mu^+\mu^-\gamma$ events

[4] M_{trk} is computed from the measured momenta of the two charged particles $\mathbf{p}_\pm$ using energy and momentum conservation under the assumptions that both particles have the same mass and that there is only one photon present in the event:

$$\left(\sqrt{s} - \sqrt{|\mathbf{p}_+|^2 + M_{\mathrm{trk}}^2} - \sqrt{|\mathbf{p}_-|^2 + M_{\mathrm{trk}}^2}\right)^2 - (\mathbf{p}_+ + \mathbf{p}_-)^2 = M_\gamma^2 = 0$$

Only one of the four solutions is physical.

– a $M^2_{\pi\pi}$-dependent cut:

$$M_{\text{trk}} < 150 \cdot (1. + 0.4 \cdot (\frac{(M^2_{\pi\pi})^2}{GeV^2} + \frac{(M^2_{\pi\pi})^4}{GeV^4}))MeV \quad (2)$$

– $M_{\text{trk}} < 200$ MeV

- A cut in the angle Ω [5]:

  – $\Omega < 90°$

  – a $M^2_{\pi\pi}$-dependent cut:

$$\Omega < 2. + e^{\left(4 \cdot \frac{M^2_{\pi\pi}}{GeV^2}\right)} \quad (4)$$

About 0.6 million events in the $M^2_{\pi\pi}$ range between 0.1 and 0.85 GeV^2 are selected with these requirements (see Fig. 4).

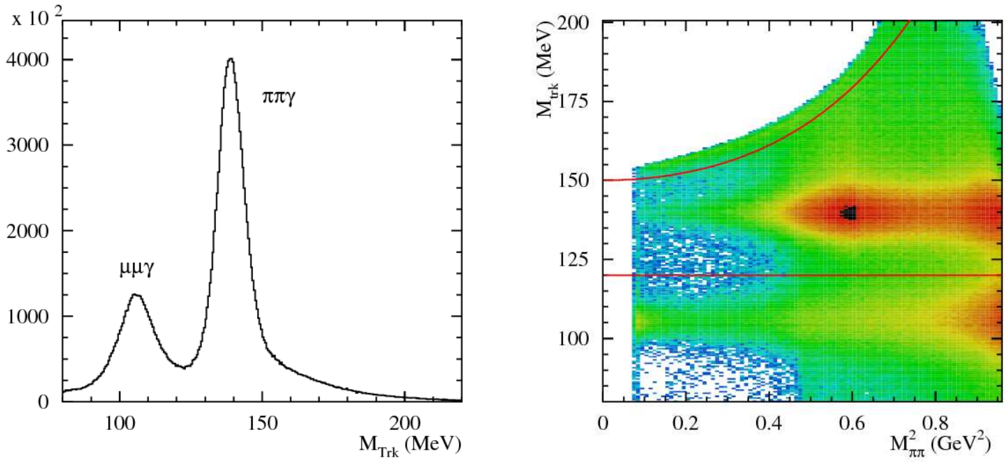

(a) (b)

Figure 2: Trackmass distribution for data sample after Large Angle acceptance cuts and `ppgtag` filter: (a) inclusive in the two pions invariant mass and (b) M_{trk} vs. $M^2_{\pi\pi}$. The $\pi^+\pi^-\gamma$ and $\mu^+\mu^-\gamma$ peaks are visible, while the very small $\pi^+\pi^-\pi^0$ contribution is hidden under the $\pi^+\pi^-\gamma$ radiative tail, on the right of the m_π-peak. The red lines represent the cuts applied: regions outside the area shown are rejected.

4 The analysis

Fig. 5 shows the complete analysis flow from the observed spectrum towards the differential cross section $d\sigma_{\pi\pi\gamma}/dM^2_{\pi\pi}$, the two-pion cross section $\sigma_{\pi\pi}$ and the pion form factor $|F_\pi|^2$.

[5] Ω is the three-dimensional angle between the direction of the selected photon γ_i and the missing momentum:

$$\Omega_i = \text{acos}\left(\frac{\vec{p}_{\text{miss}} \cdot \vec{p}_{\gamma,i}}{|\vec{p}_{\text{miss}}||\vec{p}_{\gamma,i}|}\right) \quad (3)$$

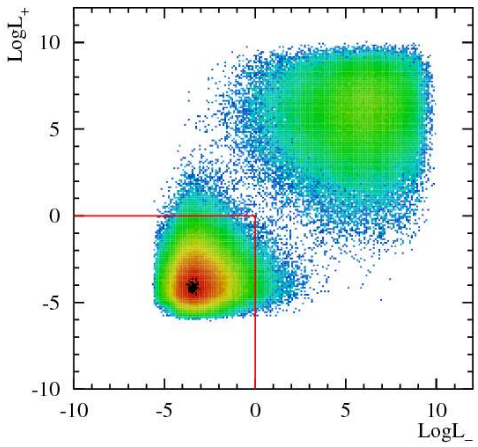

Figure 3: Distribution of $Log\mathcal{L}$ of the positive vs. the negative tracks. Events inside the red square, corresponding to $Log\mathcal{L}_+ < 0$ and $Log\mathcal{L}_- < 0$, are rejected in the analysis. These events are predominantly Bhabha events.

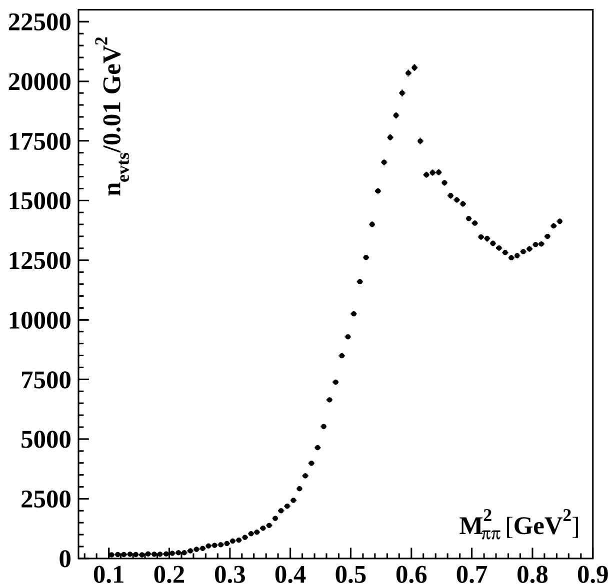

Figure 4: Spectrum of observed events after the selection. 600 000 events survive the cuts.

4.1 FILFO (offline background filter) efficiency

The FILFO filter identifies background events, such as poorly reconstructed Bhabhas, cosmic ray events and machine background events, at a very early stage of data taking and rejects them before they enter the CPU-consuming pattern recognition and track fitting algorithms [22]. The offline background filter has been completely rewritten, and as a consequence the systematic uncertainty was reduced to a negligible level, and moreover the efficiency was significantly increased. This is achieved by retaining an unbiased downscaled sample during the data taking and the deactivation of the BHABREJ subfilter [23]. Fig. 6 shows the efficiency obtained in this way. Due to the reduced statistics in the downscaled sample below 0.4 GeV^2, a larger binning of Δbin$= 0.05$ GeV^2 was used below 0.4 GeV^2.

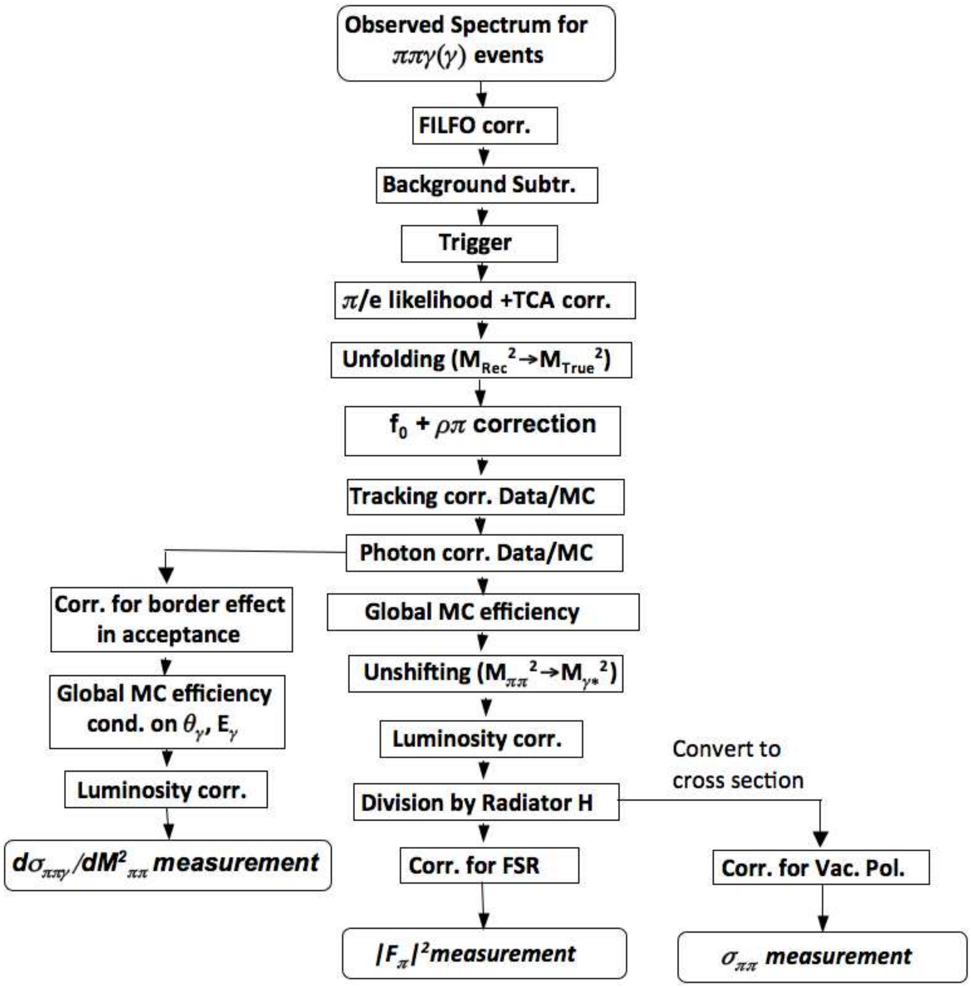

Figure 5: The description of the analysis flow.

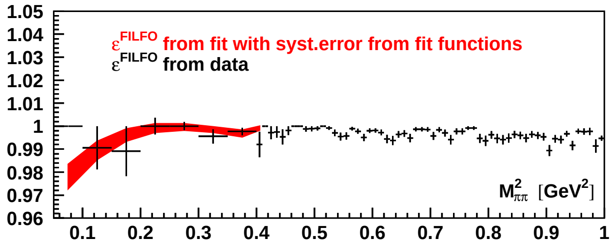

Figure 6: Efficiency of the `FILFO` reconstruction filter for pions. The red band represents the function used to fit the efficiency below 0.4 GeV^2, its error was obtained propagating the error of the fit parameters.

The efficiency was fitted below 0.4 GeV^2 with a third order polynomial, while above this value the data points themselves were used. After the fit, the FILFO efficiency can be parameterized below 0.4 GeV^2 in $x \simeq M^2_{\pi\pi}$ using

$$\epsilon^{FILFO}(x) = 0.95011 + 0.47385 \cdot x - 1.4440 \cdot x^2 + 1.3671 \cdot x^3 \tag{5}$$

The systematic error on the FILFO efficiency below 0.4 GeV^2 is obtained by propagating the errors of the fit parameters. The result can be seen in Fig. 7. Above 0.4 GeV^2, because the efficiency is obtained directly from the unbiased control sample, the systematic uncertainty is negligible.

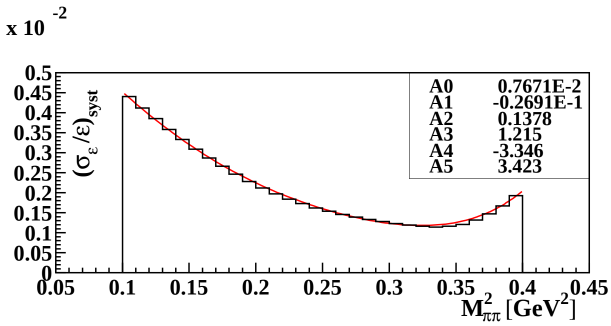

Figure 7: Fractional systematic uncertainty on the FILFO efficiency. The red line is a polynomial parameterization of the histogram.

4.2 Residual background subtraction

After the selection cuts, the main background sources are

- $e^+e^- \to \mu^+\mu^-\gamma(\gamma)$
- $e^+e^- \to \pi^+\pi^-\pi^0$
- $e^+e^- \to e^+e^-\gamma(\gamma)$
- a small fraction of $\phi \to K^+K^-$ and $\phi \to \eta\gamma$ decays contributing at $M^2_{\pi\pi} < 0.3$ GeV^2

Their combined $M_{\rm trk}$ shapes from Monte Carlo in slices of $M^2_{\pi\pi}$ together with the signal one are fitted to the data $M_{\rm trk}$ shape, to estimate their relative contributions.

The weights, $w_{ch}(j)$, are obtained as the free normalization parameters in the fit, for each channel ch in each j^{th} slice in $M^2_{\pi\pi}$. The fit procedure follows the method described in [16], using the `HBOOK` [17] routine `HMCMLL` with small modifications (see [18, 19]).
The following Monte Carlo samples are used in the fitting procedure:

- 1400 pb^{-1} of $\pi\pi\gamma(\gamma)$ events, with both ISR and FSR at NLO;
- 1400 pb^{-1} of $\mu\mu\gamma(\gamma)$ events, with both ISR and FSR at NLO;
- 225 pb^{-1} of $\pi^+\pi^-\pi^0$ events;
- 222 pb^{-1} of $\phi \to K^+K^-, \eta\gamma$ events.

$e^+e^-\gamma$ events are obtained directly from data, asking for both of the tracks to be recognized as electrons (the area delimited by the red square in Fig. 3). In the following this will be called "`nor`-configuration" of the $\pi - e$ PID.
Monte Carlo distributions are adjusted using the corrections described in [8] to give better agreement with the data distributions.
The fit is performed after the data sample has been corrected for the `FILFO` efficiency, see Sec. 4.1. To increase the sensitivity, the fit is done without the cuts in M_{trk}, shown in Fig. 2. This allows to include the full peak of $\mu^+\mu^-\gamma$, around 110 MeV, and to be more inclusive in $\pi^+\pi^-\pi^0$ events. All the other selection cuts are applied.
The fit procedure is performed in two steps. The first one is dedicated to obtain the $e^+e^-\gamma$ background contamination, evaluating $w_{ee\gamma}$, while in the second one $w_{\mu\mu\gamma}$ and $w_{\pi\pi\pi}$ are determined.

4.2.1 Step A. $e^+e^-\gamma$ contribution

The fit is performed for 15 slices in $M^2_{\pi\pi}$ (each slice of 0.05 GeV^2) between 0.1 and 0.85 GeV^2. In the standard analysis selection, at least one track has to be identified as a pion:

$$\text{"}\mathtt{or}\text{" of the } \pi - e \text{ PID likelihood}$$
$$Log\mathcal{L}_+ > 0 \ \cup \ Log\mathcal{L}_- > 0$$

According to this requirement, the background due to the $e^+e^-\gamma$ channel corresponds to those events where one track is recognized as an electron and the other as a pion, since the probability that both electrons are identified as pions by the $\pi - e$ PID estimator is negligible:

$$\text{"}\mathtt{xor}\text{" of the } \pi - e \text{ PID likelihood}$$
$$(Log\mathcal{L}_+ < 0 \ \cap \ Log\mathcal{L}_- > 0) \ \cup \ (Log\mathcal{L}_+ > 0 \ \cap \ Log\mathcal{L}_- < 0)$$

Requiring the `xor`-configuration in the data sample gives higher sensitivity to $e^+e^-\gamma$ events, because it reduces the amount of the other channels and leaves the number of radiative Bhabha unchanged.[6] Radiative Bhabha are selected directly from data events, asking both tracks to be identified as electrons ("`nor`"-configuration of the $\pi - e$ likelihood function), while for the Monte Carlo samples

[6] A check on the equivalence between ($e^+e^-\gamma$ | `xor`) and ($e^+e^-\gamma$ | `or`) has been done applying the two PID requests to the Bhabha Monte Carlo sample, proving this assumption.

the standard "`or`" PID requirement is applied. Thus fitting $e^+e^-\gamma$, $\pi^+\pi^-\gamma$, $\mu^+\mu^-\gamma$ and $\pi^+\pi^-\pi^0$ trackmass shapes to the data one obtains a precise estimation of the $e^+e^-\gamma$ amount and, consequently, of the $w_{ee\gamma}(j)$. At this step, the other channels are included only to contribute to the overall shape of $M_{\rm trk}$, and the obtained weights relative to $\pi^+\pi^-\gamma$ $\mu^+\mu^-\gamma$ and $\pi^+\pi^-\pi^0$ are not considered further in the analysis. Their correct values will be evaluated in the step B of the background fit procedure, which will be explained in the next section.
Some technical details on the fitting procedure:

1. $M^2_{\pi\pi}$ in [(0.1 − 0.60) GeV^2]: a bin-width of 2.5 MeV is used in $M_{\rm trk}$
   - $\pi^+\pi^-\gamma$, $\mu^+\mu^-\gamma$ and $\pi^+\pi^-\pi^0$ Monte Carlo samples and $e^+e^-\gamma$ events fitted to data;
2. $M^2_{\pi\pi}$ in [(0.60 − 0.85) GeV^2]: a bin-width of 1. MeV is used in $M_{\rm trk}$
   - $0.6 < M^2_{\pi\pi} < 0.65$ GeV^2: $\pi^+\pi^-\gamma$, $\mu^+\mu^-\gamma$ and $\pi^+\pi^-\pi^0$ Monte Carlo samples and $e^+e^-\gamma$ events fitted to data;
   - $0.65 < M^2_{\pi\pi} < 0.85$ GeV^2: $\pi^+\pi^-\gamma$ and $\mu^+\mu^-\gamma$ Monte Carlo samples and $e^+e^-\gamma$ events fitted to data.

The $\pi^+\pi^-\pi^0$ contribution in $M_{\rm trk}$ vanishes above 0.7 GeV^2, therefore above this value the fit is performed for only 3 sources. The result on the $e^+e^-\gamma$ weights is shown in Tab. 1, together with the $\mu^+\mu^-\gamma$ $\pi^+\pi^-\gamma$ and $\pi^+\pi^-\pi^0$weights.

Events from ϕ decays ($\phi \to \eta\gamma, K^+K^-$) do not contribute to the spectrum in the "`xor`"-condition of the $\pi - e$ PID likelihood estimator.

4.2.2 Step B. $\mu^+\mu^-\gamma$ and $\pi^+\pi^-\pi^0$ contributions

Also this second fit is performed for 15 slices in $M^2_{\pi\pi}$ (each slice of 0.05 GeV^2) between 0.1 and 0.85 GeV^2. As in the step A, all the selection cuts except for the cuts in trackmass are applied to the data sample. Again Monte Carlo in the `or`-configuration of the $\pi - e$ likelihood is used for the $\pi^+\pi^-\gamma$, $\mu^+\mu^-\gamma$ $\pi^+\pi^-\pi^0$ and $\phi \to K^+K^-, \eta\gamma$ channels while $e^+e^-\gamma$ events are obtained from data. Then all the channels are fitted together to the data $M_{\rm trk}$ histogram. For Bhabha events the normalization parameters are fixed to values of $w_{ee\gamma}(j)$ which have been evaluated previously in step A.
In addition to the corrections from [8] which act on θ and ϕ angles as well as the momenta of the two oppositely charged tracks, in this second step, the MC distributions in $M_{\rm trk}$ are adjusted to provide better agreement in the tails of the distribution and ensure a good quality of the fit (reflected in the χ^2-probability). The only effect of this additional correction is an increase in the background by 1-2% in the region below 0.15 GeV^2, where a shift of the $M_{\rm trk}$ peak for muons by +700 keV moves a larger number of MC muon events into the selection region for $M_{\rm trk} > 120$ MeV.

1. $M^2_{\pi\pi}$ in [(0.1 − 0.6) GeV^2]: bin-width of 2.5 MeV in $M_{\rm trk}$
   - $0.1 < M^2_{\pi\pi} < 0.3$ GeV^2: $\pi^+\pi^-\gamma$, $\mu^+\mu^-\gamma$ and $\pi^+\pi^-\pi^0$ Monte Carlo samples fitted to data, $\phi \to K^+K^-, \eta\gamma$ Monte Carlo and $e^+e^-\gamma$ added

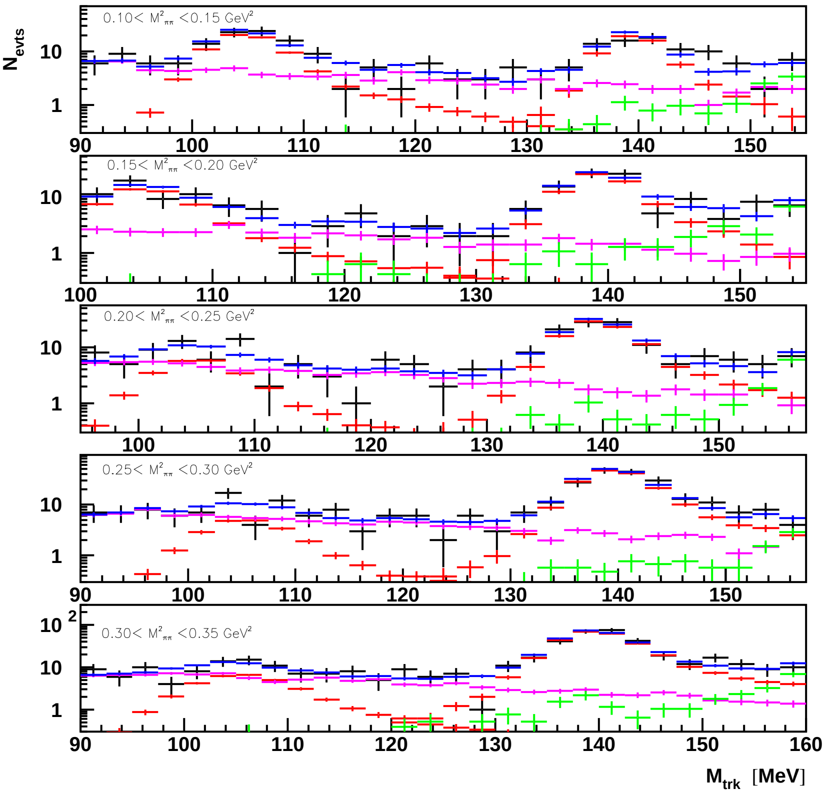

Figure 8: Trackmass shapes in different slices of $M^2_{\pi\pi}$ from 0.1 to 0.35 GeV^2 after step A of the fitting procedure described in Sec. 4.2.1. The black histogram represents the data sample, with the `xor`-configuration of the $\pi - e$ PID. The red circles represent the $\pi^+\pi^-\gamma$ and $\mu^+\mu^-\gamma$ Monte Carlo sample, the green circles the $\pi^+\pi^-\pi^0$ events. Pink circles represent the $e^+e^-\gamma$ events selected applying the `nor`-configuration of the $\pi - e$ PID to the data sample. The blue histogram contains the sum of all Monte Carlo sources and of the $e^+e^-\gamma$ channel.

($\phi \to K^+K^-, \eta\gamma$ with simple normalization to int. luminosity, $e^+e^-\gamma$ with weight parameters obtained in step A);

- $0.3 < M^2_{\pi\pi} < 0.55$ GeV^2: $\pi^+\pi^-\gamma$, $\mu^+\mu^-\gamma$ and $\pi^+\pi^-\pi^0$ Monte Carlo samples fitted to data, $e^+e^-\gamma$ added with weight parameters obtained in step A);
- $0.55 < M^2_{\pi\pi} < 0.6$ GeV^2: $\pi^+\pi^-\gamma$and $\mu^+\mu^-\gamma$ Monte Carlo samples fitted to data, $\pi^+\pi^-\pi^0$ Monte Carlo and $e^+e^-\gamma$ added ($\pi^+\pi^-\pi^0$ with simple normalization to int. luminosity, $e^+e^-\gamma$ with weight parameters obtained in step A);

2. $M^2_{\pi\pi}$ in [(0.6 – 0.85) GeV^2]: bin-width of 1.0 MeV in $M_{\rm trk}$

- $0.60 < M^2_{\pi\pi} < 0.70$ GeV^2: $\pi^+\pi^-\gamma$and $\mu^+\mu^-\gamma$ Monte Carlo samples fitted to data, $\pi^+\pi^-\pi^0$ Monte Carlo and $e^+e^-\gamma$ added ($\pi^+\pi^-\pi^0$ with simple normalization to int. luminosity, $e^+e^-\gamma$ with weight parameters obtained in step A);

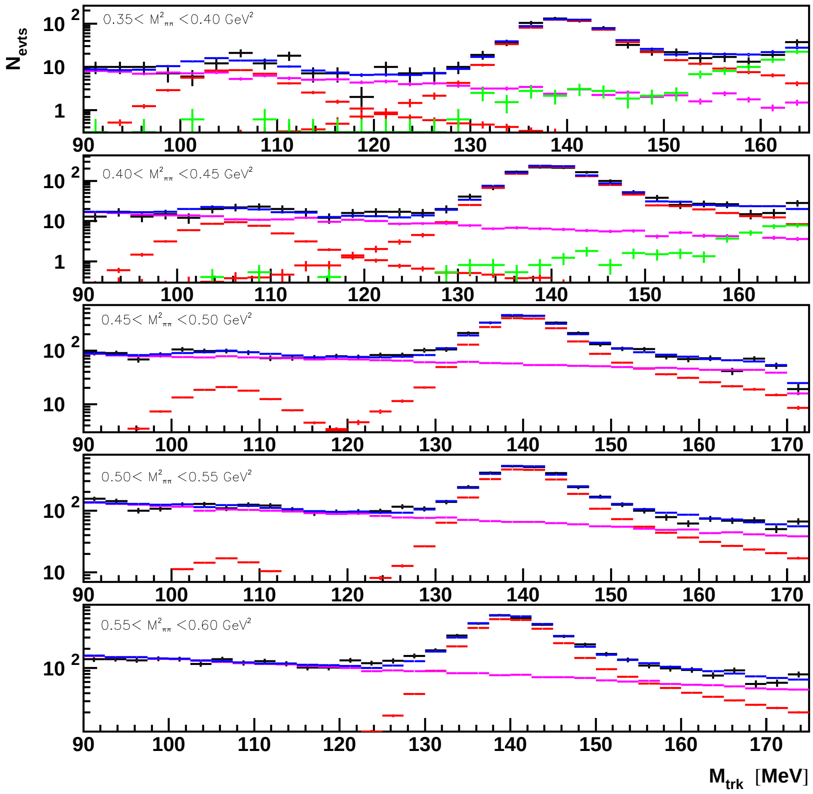

Figure 9: Trackmass shapes in different slices of $M^2_{\pi\pi}$ from 0.35 to 0.60 GeV^2 after step A of the fitting procedure described in Sec. 4.2.1. The black histogram represents the data sample, with the `xor`-configuration of the $\pi - e$ PID. The red circles represent the $\pi^+\pi^-\gamma$ and $\mu^+\mu^-\gamma$ Monte Carlo sample, the green circles the $\pi^+\pi^-\pi^0$ events. Pink circles represent the $e^+e^-\gamma$ events selected applying the `nor`-configuration of the $\pi - e$ PID to the data sample. The blue histogram contains the sum of all Monte Carlo sources and of the $e^+e^-\gamma$ channel.

- $0.70 < M^2_{\pi\pi} < 0.85$ GeV^2: $\pi^+\pi^-\gamma$and $\mu^+\mu^-\gamma$ Monte Carlo samples fitted to data and $e^+e^-\gamma$ added (with weight parameters obtained in step A);

4.2.3 Results of the background fitting procedure

The weights $w_{ch}(j)$ ($j = 1, 2, ...15$) obtained from the background fitting procedure for each slice in $M^2_{\pi\pi}$ are shown in Tab. 1, together with the errors on each weight value and the χ^2/ndof of the fit for both the two steps.

In Fig. 8,9,10 and in Fig. 14,15,16 the trackmass shapes after the fitting procedure are shown, for step A and for step B, respectively.

The upper plots of Fig. 11(a), (b), (c) and (d) show the results of the background fitting procedure, $w_{ch}(j)$. The error bars correspond to the errors reported in Tab. 1.

The smallness of $w_{ee\gamma}$ weights is due to the fact that selecting $e^+e^-\gamma$ events by means of the `nor`-configuration of the $\pi - e$ PID increases the Bhabha yield relatively to the other channels by about a factor 20 with respect to the `or`-configuration, which is applied in the analysis. Thus a factor of approximatly 1/20 must be recovered in

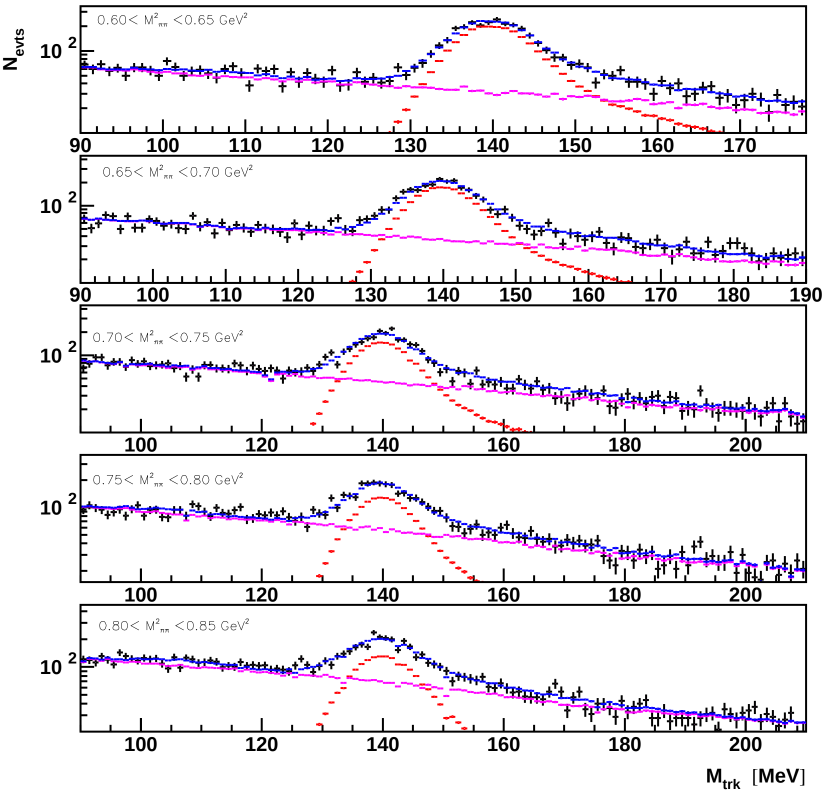

Figure 10: Trackmass shapes in different slices of $M^2_{\pi\pi}$ from 0.60 to 0.85 GeV^2 after step A of the fitting procedure described in Sec. 4.2.1. The black histogram represents the data sample, with the `xor`-configuration of the $\pi - e$ PID. The red circles represent the $\pi^+\pi^-\gamma$ Monte Carlo sample. Pink circles represent the $e^+e^-\gamma$ events selected applying the `nor`-configuration of the $\pi - e$ PID to the data sample. The blue histogram contains the sum of all Monte Carlo sources and of the $e^+e^-\gamma$ channel.

$M^2_{\pi\pi}$ (GeV^2)	$w_{\mu\mu\gamma} \pm \delta w_{\mu\mu\gamma}$	$w_{\pi\pi\pi} \pm \delta w_{\pi\pi\pi}$	$w_{ee\gamma} \pm \delta w_{ee\gamma}$	χ^2_{min}/ndof step A	$P(\chi^2 > \chi^2_{min})$ step A (%)	χ^2_{min}/ndof step B	$P(\chi^2 > \chi^2_{min})$ step B (%)
0.10-0.15	0.96±0.02	0.59±0.16	0.059±0.011	16.2/22	80.8	16.9/21	71.6
0.15-0.20	0.93±0.03	0.78±0.22	0.043±0.017	9.8/18	93.8	13.4/17	70.6
0.20-0.25	0.95±0.03	0.76±0.18	0.065±0.015	14.8/21	83.1	20.2/20	44.8
0.25-0.30	1.00±0.03	0.58±0.32	0.055±0.009	17.8/23	76.8	19.6/22	60.8
0.30-0.35	0.96±0.02	0.62±0.22	0.043±0.008	24.5/24	43.3	22.5/24	54.8
0.35-0.40	0.92±0.02	1.08±0.18	0.035±0.006	33.8/26	13.9	30.6/26	24.2
0.40-0.45	0.96±0.02	1.07±0.24	0.048±0.006	33.5/27	18.2	48.2/27	0.7
0.45-0.50	0.96±0.02	2.07±0.34	0.056±0.002	33.6/29	25.6	39.6/29	9.1
0.50-0.55	0.96±0.02	0.82±0.73	0.041±0.001	41.3/29	6.5	44.5/29	3.3
0.55-0.60	0.99±0.01	1.00±0.00	0.040±0.001	46.0/30	3.1	47.9/30	2.0
0.60-0.65	0.97±0.01	1.00±0.00	0.033±0.001	71.2/84	83.9	102.8/84	8.0
0.65-0.70	0.96±0.01	1.00±0.00	0.031±0.001	107.3/97	22.3	123.2/96	3.2
0.70-0.75	0.94±0.01	0.00±0.00	0.031±0.001	137.6/117	9.4	112.6/117	59.9
0.75-0.80	0.93±0.01	0.00±0.00	0.031±0.001	129.4/117	20.4	136.3/117	10.7
0.80-0.85	0.97±0.01	0.00±0.00	0.030±0.001	122.1/117	35.4	140.3/117	7.0

Table 1: Weights for each background source obtained from the background fitting procedure.

the weights.

For $\mu^+\mu^-\gamma$, $\pi^+\pi^-\gamma$ and $\pi^+\pi^-\pi^0$ the value of w_{ch} is a direct test of how well the Monte Carlo prediction works: a value of w_{ch} equal to 1 implies that the luminosity scaled Monte Carlo is excellent. From Tab. 1 one sees that the simulation, even if rather well reproducing the data, needs to be adjusted by few percent.

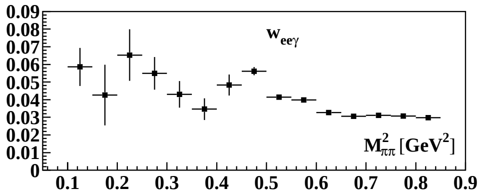

(a)

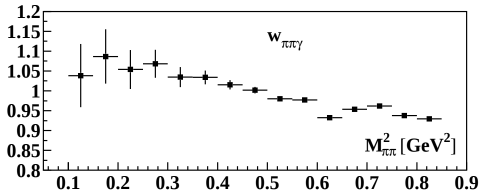

(b)

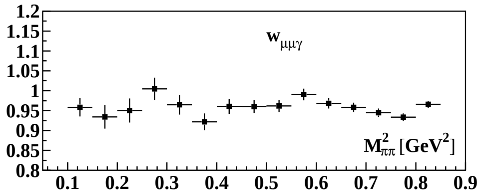

(c)

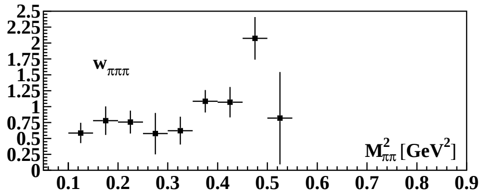

(d)

Figure 11: Weights for $e^+e^-\gamma$ (a), $\pi^+\pi^-\gamma$ (b), $\mu^+\mu^-\gamma$ (c) and $\pi^+\pi^-\pi^0$ (d) obtained from the fit procedures.

The normalization parameters $w_{ch}(k)$ are applied to each sample (Monte Carlo and $e^+e^-\gamma$) in the standard selection, where all the analysis cuts are applied, including the cuts in trackmass. The bin width in $M^2_{\pi\pi}$ for the analysis is 0.01 GeV^2, which is five times the number of slices for $w_{ch}(k)$, so each weight of the k^{th} slice in $M^2_{\pi\pi}$ acts on five consecutive bins contained in that specific interval.

The fraction of background events is obtained as

$$f_{\text{tot}} \equiv N_{\text{bkg}}/N_{\text{dat}} = \frac{w_{\mu\mu\gamma} \cdot N_{\mu\mu\gamma} + w_{ee\gamma} \cdot N_{ee\gamma} + w_{\pi\pi\pi} \cdot N_{\pi\pi\pi} + N_{K^+K^-+\eta\gamma}}{N_{\text{dat}}}, \tag{6}$$

for each bin of $M^2_{\pi\pi}$, relative to the number of data events N_{tot} found in the bin. The data spectrum is then corrected in each bin with the factor $(1 - f_{\text{tot}})$:

$$N_{M^2_{\pi\pi}} = N_{\text{dat}} \cdot (1 - f_{\text{tot}}). \tag{7}$$

The statistical error of the combined background fraction in each bin i of $M^2_{\pi\pi}$ is calculated by

$$\begin{aligned}
(\delta f_i)^2 = &\left(\frac{w_{\mu\mu\gamma,i} \cdot \delta N_{\mu\mu\gamma,i}}{N_{\text{dat},i}}\right)^2 + \left(\frac{w_{\mu\mu\gamma,i} \cdot N_{\mu\mu\gamma,i} \cdot \delta N_{\text{dat},i}}{N^2_{\text{dat},i}}\right)^2 + \\
&\left(\frac{w_{ee\gamma,i} \cdot \delta N_{ee\gamma,i}}{N_{\text{dat},i}}\right)^2 + \left(\frac{w_{ee\gamma,i} \cdot N_{ee\gamma,i} \cdot \delta N_{\text{dat},i}}{N^2_{\text{dat},i}}\right)^2 + \\
&\left(\frac{w_{\pi\pi\pi,i} \cdot \delta N_{\pi\pi\pi,i}}{N_{\text{dat},i}}\right)^2 + \left(\frac{w_{\pi\pi\pi,i} \cdot N_{\pi\pi\pi,i} \cdot \delta N_{\text{dat},i}}{N^2_{\text{dat},i}}\right)^2 +
\end{aligned}$$

$$\left(\frac{\delta N_{K^+K^-+\eta\gamma,i}}{N_{\mathrm{dat},i}}\right)^2 + \left(\frac{N_{K^+K^-+\eta\gamma,i}\cdot\delta N_{\mathrm{dat},i}}{N^2_{\mathrm{dat},i}}\right)^2 \tag{8}$$

The different values for the integrated luminosity for data and Monte Carlo events are taken into account properly in the procedure.

In Fig. 12(a) the spectra in $M^2_{\pi\pi}$ for data (black circles), signal $\pi^+\pi^-\gamma$ (empty blue circles), $\mu^+\mu^-\gamma$ (green circles), $e^+e^-\gamma$ (red circles), $\pi^+\pi^-\pi^0$ (pink circles) and $\phi \to K^+K^-, \eta\gamma$ (yellow circles) are shown. The sum of all background sources is represented by the blue points. The peculiar trend of $e^+e^-\gamma$ events, which dramatically drop for $M^2_{\pi\pi}$ values below 0.4 GeV^2, is due to the momenta cuts introduced to avoid spiralising tracks in the drift chamber. In Fig. 12(b) the relative amount of background over data events, i.e. the f_{tot} value of Eq. 6, is shown. In Fig. 13 the ratios

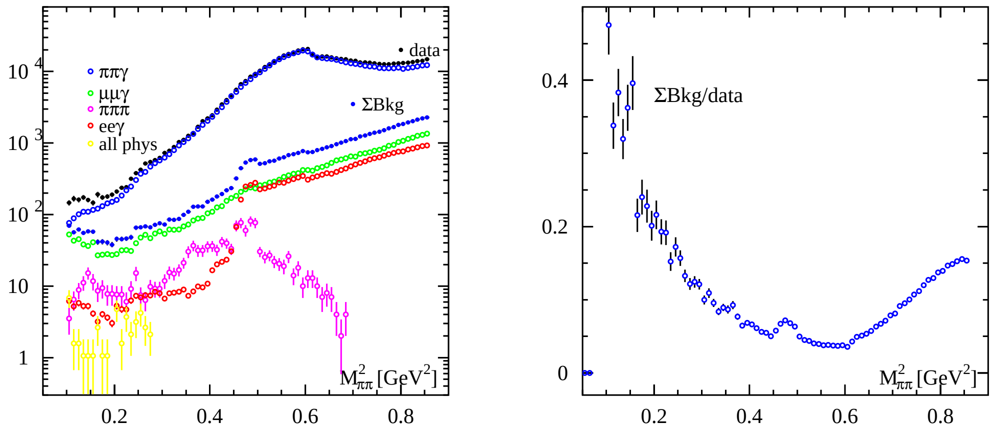

(a) (b)

Figure 12: Plot of the $M^2_{\pi\pi}$ spectra for different channels after the background fitting procedure, in (a). Ratio between the sum of all the background sources over data is shown in (b).

between each background source, ch, and selected data events, $f_{ch} = (w_{ch}\cdot N_{ch})/N_{\mathrm{dat}}$, is shown.

4.2.4 Systematic error of the background fit procedure

The systematic uncertainty due to the background estimation is derived from the errors on the weights w obtained in the fit procedures. The errors on the weights w obtained in the fit are enlarged if the probability $P_{\chi^2>\chi^2_{min}}$ is smaller than 5% according to

$$\delta w \longrightarrow \sqrt{\frac{\chi^2_{min}}{\mathrm{ndf}}}\cdot\delta w \tag{9}$$

Since $\delta\sigma_{\pi\pi\gamma}$ is proportional to $(1-f) = 1 - f_{\mu\mu\gamma} - f_{\pi\pi\pi} - f_{ee\gamma}$, the relative uncertainty of the cross section from the weights is given by:

$$\frac{\delta\sigma_{\pi\pi\gamma}}{\sigma_{\pi\pi\gamma}} = \frac{\sqrt{\left(\frac{\delta w_{\mu\mu\gamma}}{w_{\mu\mu\gamma}}f_{\mu\mu\gamma}\right)^2 + \left(\frac{\delta w_{\pi\pi\pi}}{w_{\pi\pi\pi}}f_{\pi\pi\pi}\right)^2 + 2\cdot\varrho_{\mu\mu\gamma,\pi\pi\pi}\frac{\delta w_{\mu\mu\gamma}}{w_{\mu\mu\gamma}}f_{\mu\mu\gamma}\frac{\delta w_{\pi\pi\pi}}{w_{\pi\pi\pi}}f_{\pi\pi\pi} + \left(\frac{\delta w_{ee\gamma}}{w_{ee\gamma}}f_{ee\gamma}\right)^2}}{1 - f_{\mu\mu\gamma} - f_{\pi\pi\pi} - f_{ee\gamma}} \tag{10}$$

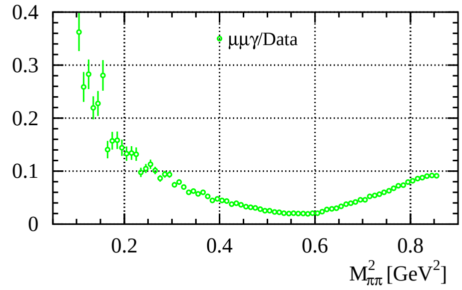

(a)

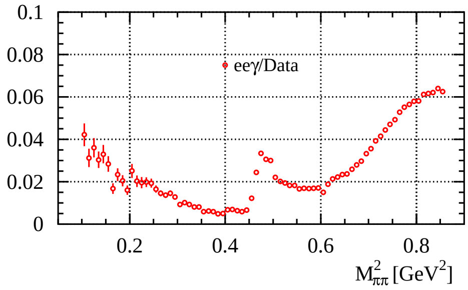

(b)

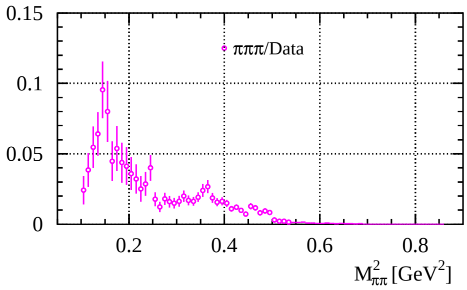

(c)

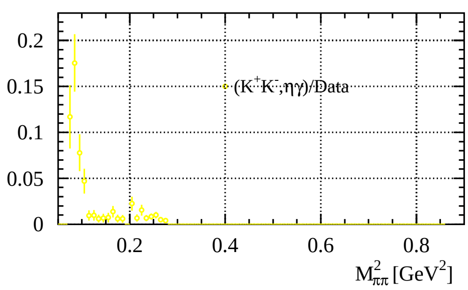

(d)

Figure 13: Fraction of background sources with respect to the data events after the analysis cuts described in Sec. 3.2. The errors shown are defined via the individual terms in eq. 8.

The parameter $\varrho_{\mu\mu\gamma,\pi\pi\pi}$ describes the correlation between the fit parameters $w_{\mu\mu\gamma}$ and $w_{\pi\pi\pi}$. Its value varies between -0.05 and +0.05. Fig. 17 shows the systematic uncertainty of the cross section measurement due to the background estimation.

4.3 Additional backgrounds

Despite the fact that the 2006 dataset has been taken with DAΦNE running 20 MeV below the mass of the ϕ-meson, the effect from the processes $e^+e^- \to \phi \to f_0\gamma \to \pi^+\pi^-\gamma$ and $e^+e^- \to \phi \to \varrho^\pm\pi^\mp \to (\pi^\pm\gamma)\pi^\mp$ is not fully suppressed. To estimate the effect of these channels, a modified version of the PHOKHARA generator containing the description of these processes [20], has been used. Fig. 18 (a) shows the fractional contribution of the processes $e^+e^- \to \phi \to f_0\gamma \to \pi^+\pi^-\gamma$ and $e^+e^- \to \phi \to \varrho^\pm\pi^\mp \to (\pi^\pm\gamma)\pi^\mp$ to the signal.

The systematic uncertainty due to the f_0 and $\varrho^\pm\pi^\mp$ decays has been estimated comparing the outcome from the different parameter variants with the outcome from the variant giving the best fit result in [21]. Variant 4 was found to give the biggest deviation, and the systematic uncertainty has been fitted below 0.45 GeV^2 with a fourth order polynomial in $M^2_{\pi\pi} \simeq x$ (see Fig. 18 (b)):

$$\Delta\sigma_{\pi\pi\gamma}(x) = 0.2701 - 3.2686 \cdot x + 15.263 \cdot x^2 - 31.418 \cdot x^3 + 23.769 \cdot x^4 \qquad (11)$$

Above 0.45 GeV^2, the deviation between different variants is compatible with (1.000±0.0002), and is considered negligible for this analysis.

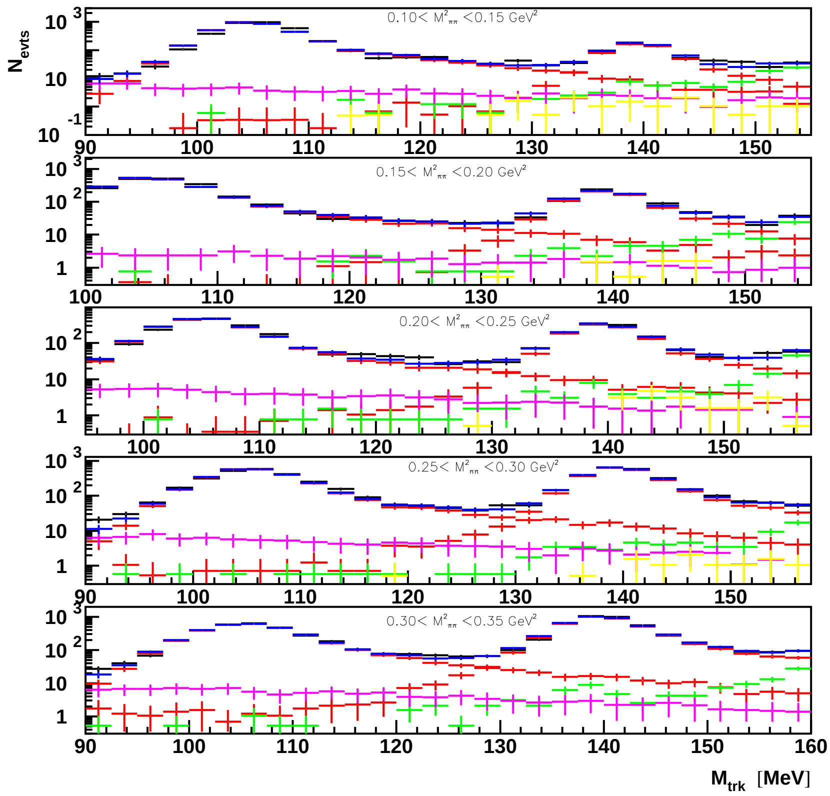

Figure 14: Trackmass shapes in different slices of $M^2_{\pi\pi}$ from 0.1 to 0.35 GeV^2 after step B of the fitting procedure described in Sec. 4.2.1. The black histogram represents the data sample, with the `or`-configuration of the $\pi - e$ PID. The red histos represent the $\pi^+\pi^-\gamma$ and $\mu^+\mu^-\gamma$ Monte Carlo samples, the green histogram the $\pi^+\pi^-\pi^0$ one and the pink histogram the $e^+e^-\gamma$ events, as obtained from step A. The yellow entries represent the $K^+K^-, \eta\gamma$ background. The blue histogram indicates the sum of all Monte Carlo sources and of the $e^+e^-\gamma$ channel.

4.4 Trigger efficiency

In the 2006 data sample only the calorimeter trigger is used. An event, to be acquired, has to fire at least two *trigger sectors*, see [24]. The fired sectors can be located either both in the barrel, or in the two endcaps (not in the same) or one in the barrel and the other in one of the two endcaps. However, because of the large angle acceptance cuts, the trigger sectors in the endcaps are not involved in this analysis.

Since one cluster can consist of more than one trigger sector, it may happen that one single particle can trigger the event. In this case one has a so-called "self triggering" particle, e.g. pion or photon.

The trigger efficiency, $\varepsilon_{\rm trg}$, is evaluated using ca. 50 pb^{-1} of data. Signal Monte Carlo is used only for testing and for evaluating the systematic uncertainty.

To evaluate the single particle efficiency (for π^+, π^- and γ) and to obtain an unbiased sample of the considered particle, two particles are required to trigger the event, then the trigger sectors fired by the remaining one are counted. An example is sketched

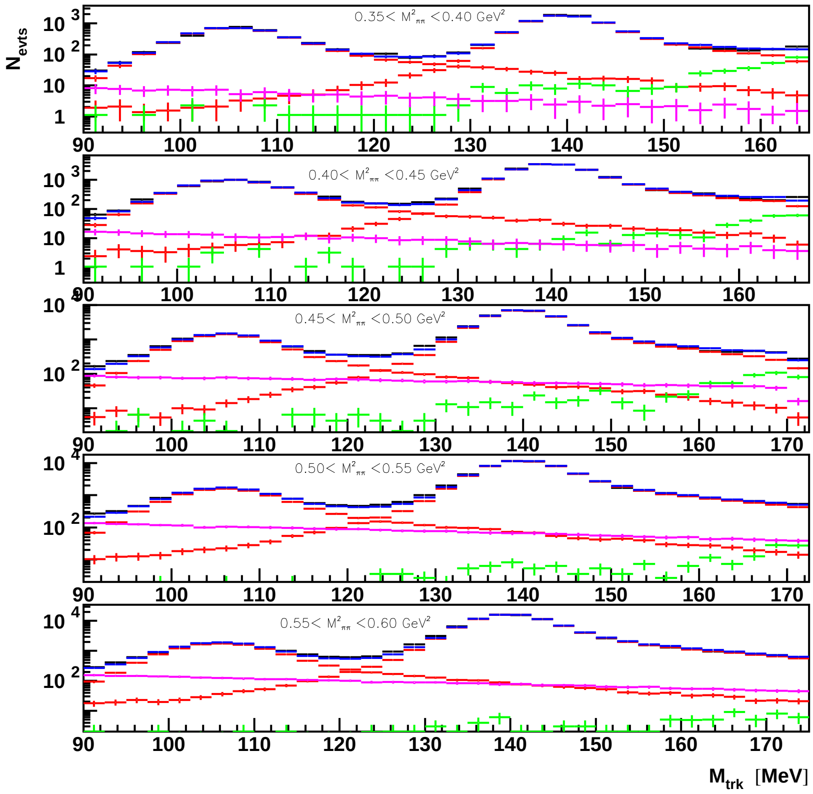

Figure 15: Trackmass shapes in different slices of $M^2_{\pi\pi}$ from 0.35 to 0.60 GeV^2 after step B of the fitting procedure described in Sec. 4.2.1. The black histogram represents the data sample, with the `or`-configuration of the $\pi - e$ PID. The red histos represent the $\pi^+\pi^-\gamma$ and $\mu^+\mu^-\gamma$ Monte Carlo samples, the green histogram the $\pi^+\pi^-\pi^0$ one and the pink histogram the $e^+e^-\gamma$ events, as obtained from step A. The blue histogram indicates the sum of all Monte Carlo sources and of the $e^+e^-\gamma$ channel.

in Fig. 19, where a π^- and a γ have triggered the event unbiasing the π^+, whose efficiency is measured.
The single particle efficiency, $\varepsilon_{\mathrm{trg}}(\theta_{\pi^+,\pi^-,\gamma}, p_{\pi^+,\pi^-,\gamma})$, is evaluated in 8 slices between 50° and 130° of polar angle and in 10 bins between 200 and 500 MeV for the pion momentum and in 10 bins between 50 and 500 MeV for the photon energy. The single particle efficiency can be seen in Fig. 20 for the positive pion, in Fig. 21 for the negative pion and in Fig. 22 for the photon. The trigger efficiency is very close to 100% for the photon, while for $\pi^\pm$ it is well above 97% in $|90° - \theta_{\pi^\pm}| < 30°$. At lower polar angles, $30° < |90° - \theta_{\pi^\pm}| < 40°$, the bending of the low momentum tracks in the magnetic field, causes a drop in the efficiency, as can be seen in Fig. 20 and Fig. 21. This drop is due to the less efficient performance of the barrel-endcaps intersections, where the bent tracks enter the calorimeter.

The trigger efficiency as a function of $M^2_{\pi\pi}$ is obtained applying the same mapping method used for the likelihood efficiency. The passage

$$\varepsilon_{\mathrm{trg}}(\theta_{\pi^+,\pi^-,\gamma}, p_{\pi^+,\pi^-,\gamma}) \to \varepsilon_{\mathrm{trg}}(M^2_{\pi\pi}),$$

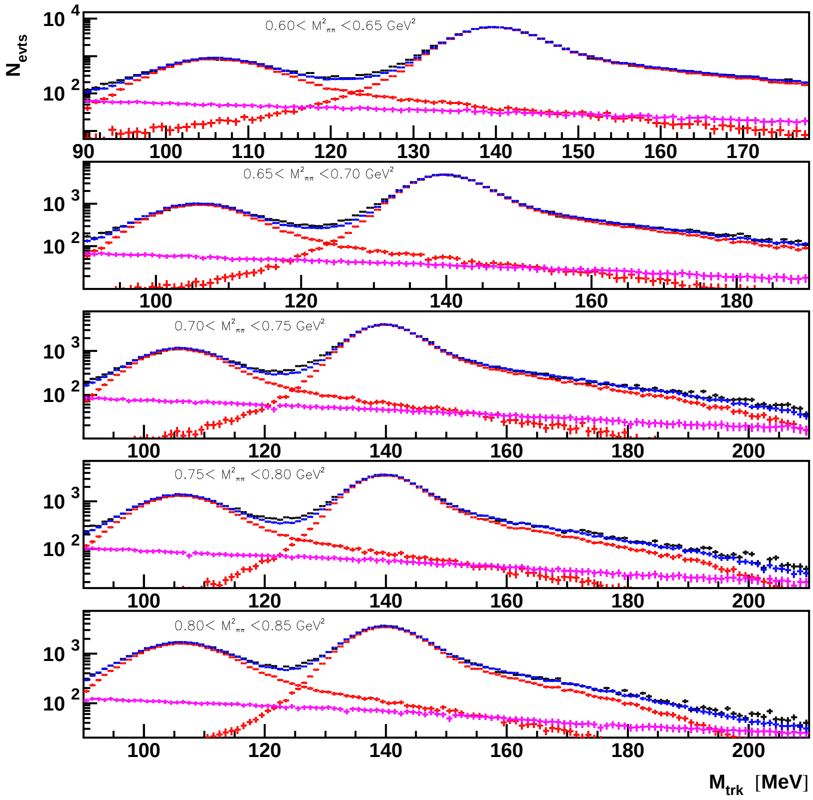

Figure 16: Trackmass shapes in different slices of $M^2_{\pi\pi}$ from 0.60 to 0.85 GeV^2 after step B of the fitting procedure described in Sec. 4.2.1. The black histogram represents the data sample, with the `or`-configuration of the $\pi - e$ PID. The red histos represent the $\pi^+\pi^-\gamma$ and $\mu^+\mu^-\gamma$ Monte Carlo samples and the pink histogram the $e^+e^-\gamma$ events, as obtained from step A. The blue histogram indicates the sum of all Monte Carlo sources and of the $e^+e^-\gamma$ channel.

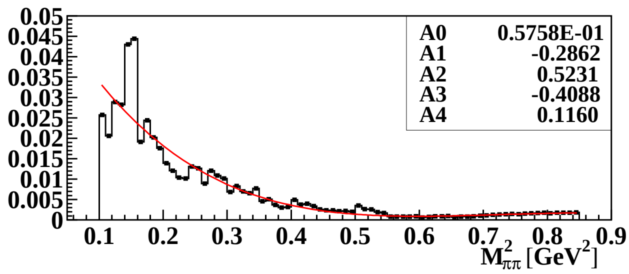

Figure 17: Systematic uncertainty of the cross section measurement due to the background estimation. The red line represents a parameterization with a fourth order polynomial.

is performed taking the kinematic from Monte Carlo $\pi^+\pi^-\gamma$ events using

$$\varepsilon_{\rm trg}(M^2_{\pi\pi}) = \frac{1}{N}\sum_{k=1}^{n} \nu_k \; \varepsilon_k, \qquad (12)$$

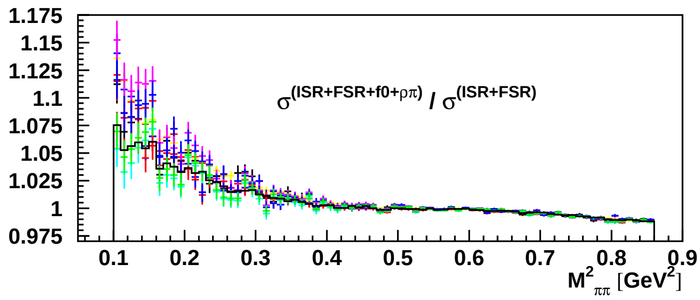

(a)

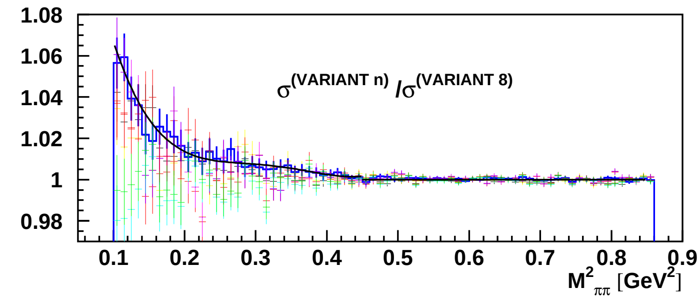

(b)

Figure 18: (a) Fractional contribution of the processes $e^+e^- \to \phi \to f_0\gamma \to \pi^+\pi^-\gamma$ and $e^+e^- \to \phi \to \varrho^\pm\pi^\mp \to (\pi^\pm\gamma)\pi^\mp$ (estimated from MC simulation) to the signal. 10 different variants of the parameter sets have been used. The solid line histogram shows the variant with a set of parameters which gave the best fit result in [21] (variant 8). (b) Comparison between all the variants and the one with the best fit result. The solid histogram shows the effect of the variant with the largest deviation (variant 4 in [21]). Below 0.45 GeV^2, the solid histogram has been fitted with a fourth order polynomial.

which is the analogous of Eq. 14. The parameter ε_k is given by

$$\begin{aligned}\varepsilon_k = 1 &- P_0^{\pi^+}(\theta,p)P_0^{\pi^-}(\theta,p)P_0^{\gamma}(\theta,p)\\ &-P_1^{\pi^+}(\theta,p)P_0^{\pi^-}(\theta,p)P_0^{\gamma}(\theta,p)\\ &-P_0^{\pi^+}(\theta,p)P_1^{\pi^-}(\theta,p)P_0^{\gamma}(\theta,p)\\ &-P_0^{\pi^+}(\theta,p)P_0^{\pi^-}(\theta,p)P_1^{\gamma}(\theta,p)\end{aligned} \tag{13}$$

where $P^j_{0(1)}(\theta,p)$ is the probability for the particle j (i.e. π^+, π^- or γ), at polar angle θ and momentum p, to fire 0 (1 and only 1) trigger sectors, evaluated with the single particle method described above. Inserting $\varepsilon_k^{\rm data}$, see Eq. 13, in Eq. 12 one gets $\varepsilon_{\rm trg}^{\rm data}(s_\pi)$. The trigger efficiency as a function of $M^2_{\pi\pi}$ is shown in Fig. 23. The efficiency is very close to 100%. The inefficiency is essentially due to the tracks, as explained before, since the photon is always firing at least one trigger sector. The $\pi^+\pi^-\gamma$ spectrum is corrected bin-by-bin for the result shown in Fig. 28.
A comparison between trigger efficiency evaluated from data, $\varepsilon_{\rm trg}^{\rm data}(\theta_{\pi^+,\pi^-,\gamma}, p_{\pi^+,\pi^-,\gamma})$, and from $\pi^+\pi^-\gamma$ Monte Carlo sample, $\varepsilon_{\rm trg}^{\rm MC}(\theta_{\pi^+,\pi^-,\gamma}, p_{\pi^+,\pi^-,\gamma})$, has been performed.

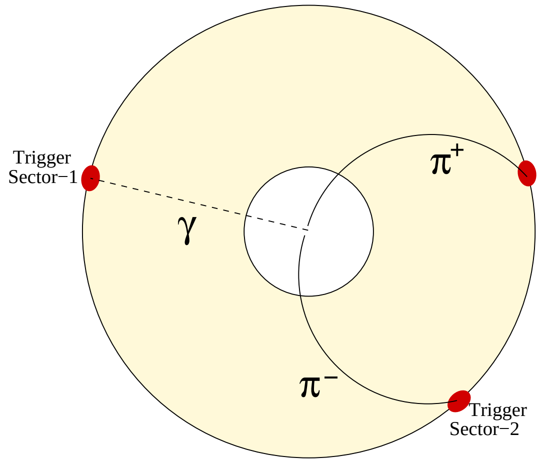

Figure 19: Schematic representation of the single particle trigger efficiency. In this example a π^- and a γ are triggering the event providing an unbiased sample for π^+, whose probability of firing trigger sectors is measured.

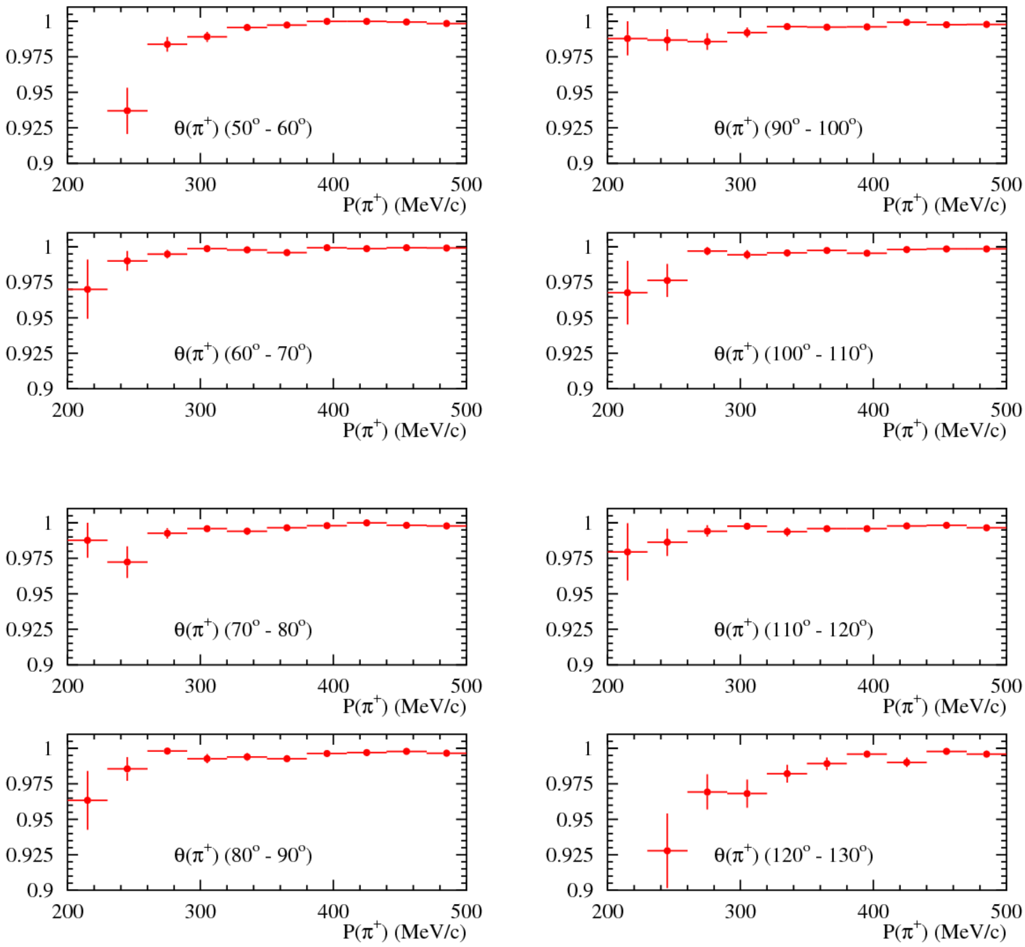

Figure 20: Efficiency of firing at least one trigger sector for unbiased π^+ sample as a function of momentum in slices of polar angle.

The ratio $\varepsilon_{\text{trg}}^{\text{data}}(M_{\pi\pi}^2)/\varepsilon_{\text{trg}}^{\text{MC}}(M_{\pi\pi}^2)$, evaluated after the mapping described by Eq. 12 and Eq. 13, is ca. 1×10^{-4} over the whole energy range.

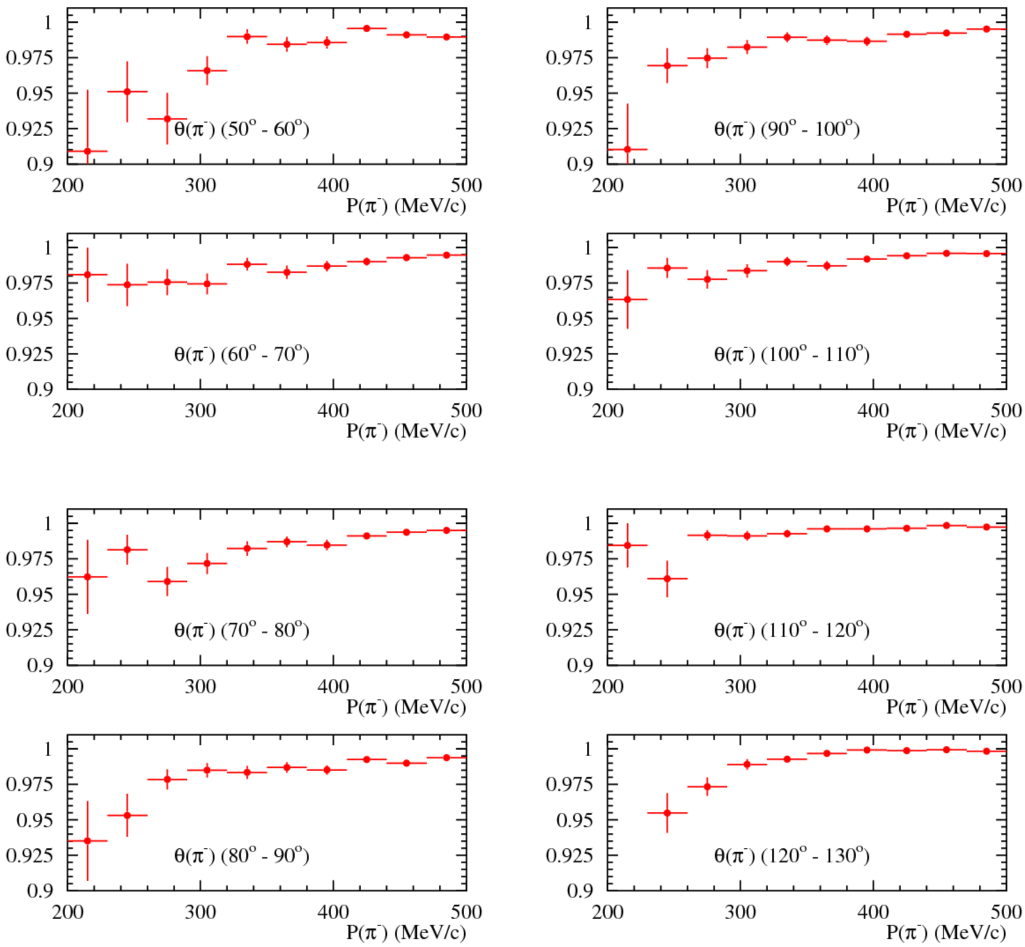

Figure 21: Efficiency of firing at least one trigger sector for unbiased π^- sample as a function of momentum in slices of polar angle.

4.4.1 Systematic error on the trigger efficiency

The evaluation of the systematic uncertainty is performed by comparing the single particle method, described above and indicated as “mapping”, with the “direct” efficiency evaluation, using in both cases the $\pi^+\pi^-\gamma$ Monte Carlo sample. The direct method consists in looking at how many Monte Carlo events, for a certain bin of $M^2_{\pi\pi}$, have fired at least two trigger sectors. The systematics is evaluated performing the ratio between $\varepsilon_{\rm trg}^{\pi\pi\gamma\ {\rm dir}}(M^2_{\pi\pi})$ and $\varepsilon_{\rm trg}^{\pi\pi\gamma\ {\rm map}}(M^2_{\pi\pi})$, where $\varepsilon_{\rm trg}^{\pi\pi\gamma\ {\rm map}}(M^2_{\pi\pi})$ is given by Eq. 12 and Eq. 13. In the upper plot of Fig. 24 the comparison between the two methods is shown. The ratio is fitted by a third order polynomial function (red line in the lower plot of Fig. 24), in order to parameterize the dependence on $M^2_{\pi\pi}$ of the systematic uncertainty.

The systematic uncertainty, shown in Fig. 25, is then given by the deviation of the polynomial function from 1.

4.5 π/e likelihood and TCA efficiency

In the analysis, each track is extrapolated to the calorimeter and at least one cluster is searched within a sphere of radius $|\vec{r}_{\rm ext} - \vec{r}_{\rm clu}| < 90$ cm, where $\vec{r}_{\rm ext}$ represents the

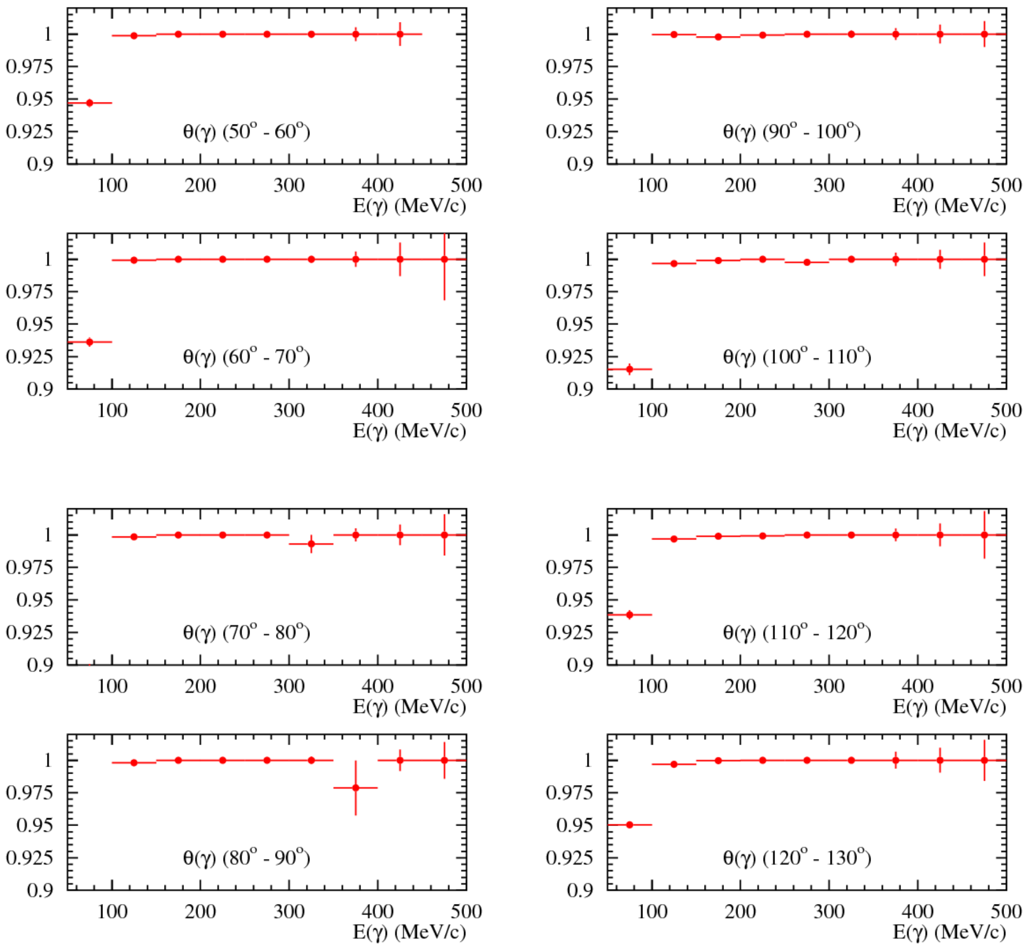

Figure 22: Efficiency of firing at least one trigger sector for unbiased γ sample as a function of momentum in slices of polar angle.

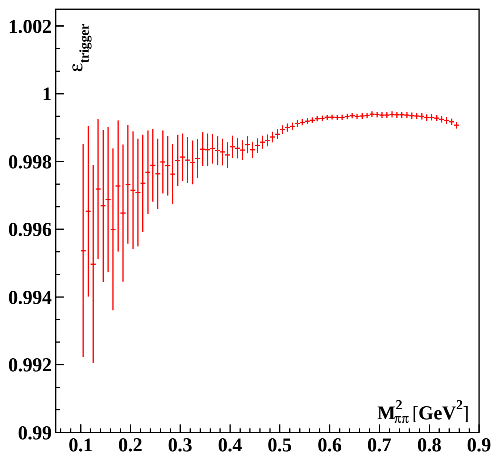

Figure 23: Trigger efficiency as a function of the $\pi^+\pi^-$-systems' invariant mass.

coordinates of the extrapolated impact point of the track in the calorimeter and $\vec{r}_{\rm clu}$ is the position of the cluster centroid. If there is more than one cluster inside this

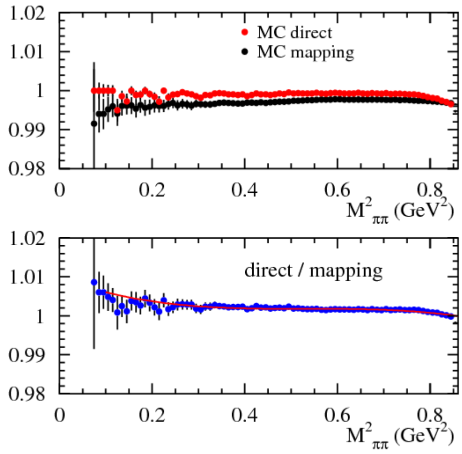

Figure 24: The upper plot shows the comparison between the trigger efficiency evaluated with the single particle method, black circles, and the direct method, red circles. In the lower plot the ratio between the two, together with a fit function, is shown.

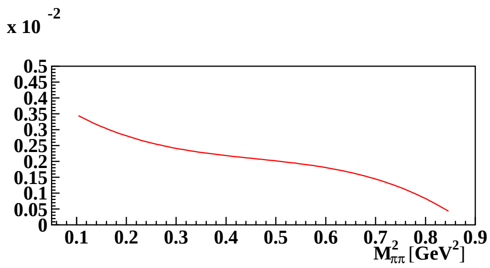

Figure 25: Systematic uncertainty on trigger efficiency, given by the deviation from 1 of the function used to fit the ratio $\varepsilon_{\rm trg}^{\pi\pi\gamma\ \rm dir}(M^2_{\pi\pi})$ over $\varepsilon_{\rm trg}^{\pi\pi\gamma\ \rm map}(M^2_{\pi\pi})$, shown in Fig. 24.

sphere, the most energetic one is associated to the track.

In the case that both tracks impinge on the same spot in the calorimeter (which happens at values of $M^2_{\pi\pi}$ close to 0.2 GeV^2), the resulting cluster will have the combined energy deposit of both charged particles, and bias the likelihood estimator. Therefore, events are excluded for which the centroid of the clusters associated to the two tracks have a distance which is smaller than 90 cm. The resulting inefficiency is contained in the global Monte Carlo efficiency (sec. 4.7).
To select the event, at least one track has to be recognized as a pion, as written in Sec. 3.2, which means that at least one track must have an associated cluster with $\log \mathcal{L}_\pi/\mathcal{L}_e > 0$.
The single $\pi^\pm$ efficiency, is defined as the probability to find an associated cluster in the calorimeter with $\log \mathcal{L}_\pi/\mathcal{L}_e > 0$, conditioned to the presence of another track recognized to be a $\pi^\mp$. The efficiency is evaluated from a data control sample with the following requirements:

- two tracks of opposite sign satisfying the same conditions on point-of-closest-approach (PCA) and first drift chamber hit as applied in the analysis;

- $50^\circ < \theta_\pm < 130^\circ$;
- $|M_{\rm trk} - m_\pi| < 2.5$ MeV, to obtain a clean sample of $\pi^+\pi^-\gamma$;
- cut in Ω-angle as in Eq. 3.

The single pion efficiency, $\varepsilon_{\rm like}(\theta_{\pi^\pm}, p_{\pi^\pm})$, is evaluated in 8 slices of polar angle between 50° and 130° and in 30 bins of momentum modulus $p_{\pi^\pm}$ between 200 and 500 MeV, for positive and negative track. The efficiencies as a function of polar angle and momentum can be seen in Fig. 26 and in Fig. 27 for positive and negative tracks, respectively.

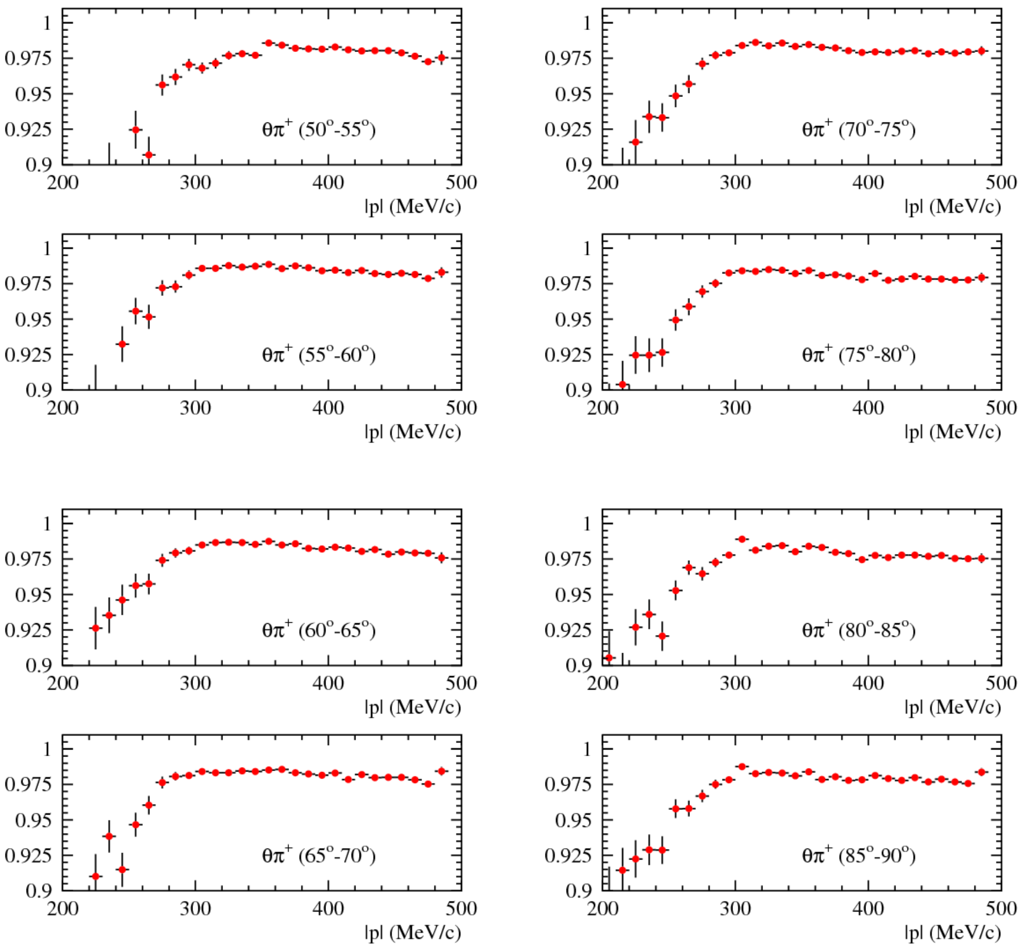

Figure 26: PID likelihood single particle efficiency for π^+ as a function of polar angle and momentum.

The likelihood efficiency as a function of $M^2_{\pi\pi}$ is obtained by *mapping* these single pion efficiencies with the kinematics generated from simulation. This allows to extract the likelihood efficiency as a function of $M^2_{\pi\pi}$ using the measured values of $\varepsilon_{\rm like}(\theta_{\pi^\pm}, p_{\pi^\pm})$, i.e

$$\varepsilon_{\rm like}(\theta_{\pi^\pm}, p_{\pi^\pm}) \longrightarrow \varepsilon_{\rm like}(M^2_{\pi\pi}).$$

The same cuts applied in the analysis are used in the Monte Carlo $\pi^+\pi^-\gamma$ events to extract $\varepsilon_{\rm like}(M^2_{\pi\pi})$. For a given bin in $M^2_{\pi\pi}$ (width $= 0.01$ GeV^2), the likelihood efficiency is an average over the n different phase space configurations $(\theta_{\pi^+}, p_{\pi^+}, \theta_{\pi^-}, p_{\pi^-})$

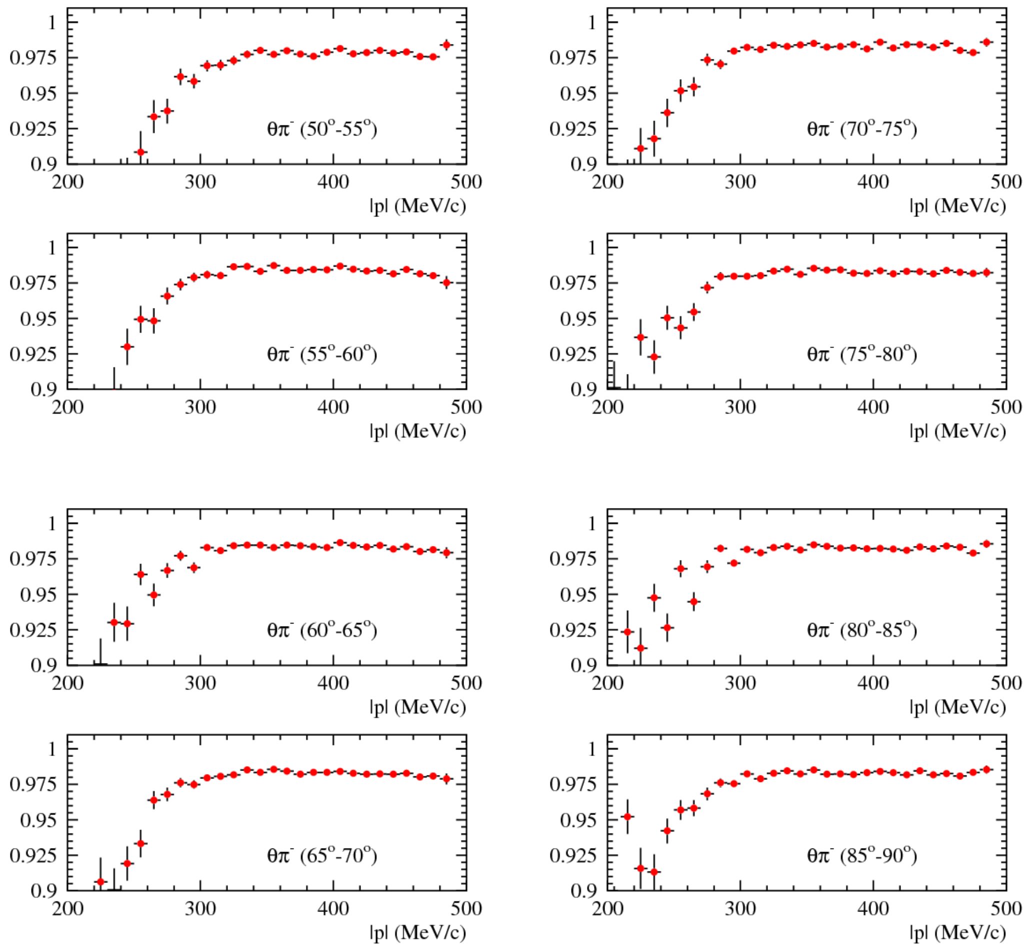

Figure 27: PID likelihood single particle efficiency for π^- as a function of polar angle and momentum.

contributing to that bin:

$$\varepsilon_{\text{like}}(M_{\pi\pi}^2) = \frac{1}{N}\sum_{k=1}^{n} \nu_k\ \varepsilon_k, \tag{14}$$

where N is the number of Monte Carlo events used to compute the frequency ν_k of a certain k configuration. In the analysis the `or`-configuration of the $\pi - e$ PID likelihood is used, thus the efficiency parameter, ε_k, to be put in the expression of the mapping, is:

$$\varepsilon_k = 1 - \left[1 - \varepsilon_{\text{like}}^{\text{data}}(\theta_{\pi^+}, p_{\pi^+})\right]\left[1 - \varepsilon_{\text{like}}^{\text{data}}(\theta_{\pi^-}, p_{\pi^-})\right]. \tag{15}$$

Inserting Eq. 15 in Eq. 14 one gets $\varepsilon_{\text{like}}^{\text{data}}(M_{\pi\pi}^2)$.
In Fig. 28 the efficiency of the `or`-configuration of the $\pi - e$ likelihood as a function of $M_{\pi\pi}^2$ is shown. The result is close to 100%, which means that the probability of misidentifying both of the tracks is very small. The drop for low values of $M_{\pi\pi}^2$ is mainly due to track to cluster association, which is more inefficient for low momentum tracks.

A test of the likelihood efficiency evaluation has been done using a Monte Carlo based procedure, i.e. obtaining the single pion efficiency values, $\varepsilon_{\text{like}}(\theta_{\pi^\pm}, p_{\pi^\pm})$, from

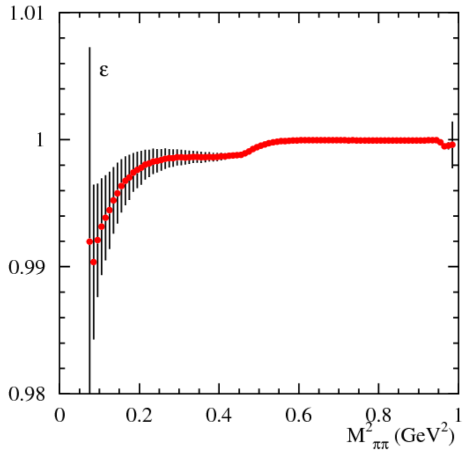

Figure 28: PID likelihood efficiency as a function of the $\pi^+\pi^-$-system invariant mass.

$\pi^+\pi^-\gamma$ Monte Carlo and then extracting the $\varepsilon_{\rm like}(M^2_{\pi\pi})$ according to Eq. 14. The result of this "fully Monte Carlo based" procedure is in very good agreement with the one from data, as it can be seen in Fig. 29. Monte Carlo is also used to estimate the systematic uncertainty, as explained below.

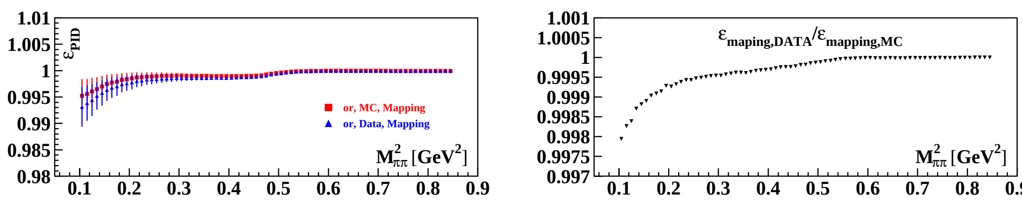

(a) (b)

Figure 29: (a) PID likelihood efficiency as a function of the $\pi^+\pi^-$-system invariant mass evaluated from data, red circles, and from $\pi^+\pi^-\gamma$ Monte Carlo, black circles. (b) The ratio of the two efficiencies.

A further check has been performed using $\pi^+\pi^-\gamma$ Monte Carlo. The single pion ("mapping") method has been compared with the "direct" method. The latter consists in looking directly at the $\pi - e$ PID efficiency for a certain value of $M^2_{\pi\pi}$. Then $\varepsilon_{\rm like}^{\pi\pi\gamma\ \rm map}(M^2_{\pi\pi})$ and $\varepsilon_{\rm like}^{\pi\pi\gamma\ \rm dir}(M^2_{\pi\pi})$ are compared for each bin of $M^2_{\pi\pi}$. In Fig. 30 the ratio between the two methods is shown, proving a very good agreement. The difference between the two methods contributes to the systematic uncertainty assigned to the PID efficiency (see next section).
The values of $\varepsilon_{\rm like}^{\rm data}(M^2_{\pi\pi})$ shown in Fig. 28 are used as bin-by-bin correction to the spectrum.

4.5.1 Systematic error on the $\pi - e$ PID efficiency

An uncertainty arises from the difference between the mapping method and the direct method, since the mapping method can not take into account correlation effects

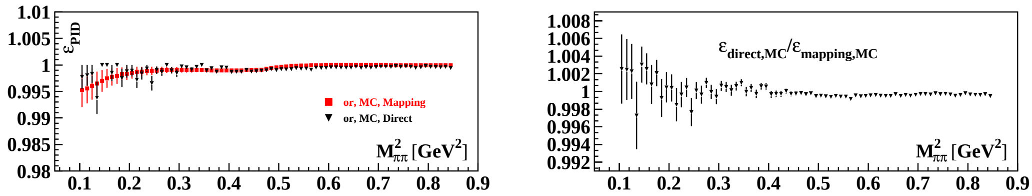

(a) (b)

Figure 30: (a) PID likelihood efficiencies evaluated by means of the single pion efficiency (mapping) and the direct method using $\pi^+\pi^-\gamma$ Monte Carlo sample.(b) Ratio of the two efficiencies.

between the two tracks. The direct method instead allows to account for the correlation effects between the tracks, but it can not be obtained from data. A comparison between the two methods (mapping and direct) using a $\pi^+\pi^-\gamma$ MC sample provides a check of the mapping method and allows to estimate the systematic effect coming from two-track correlations. To reduce the statistical fluctuations, a larger binning of 0.05 GeV^2 has been chosen below 0.4 GeV^2 for the efficiency evaluated with the direct method. Fig. 31 shows the two efficiencies as well as their absolute difference, which is taken as a a contribution to the systematic uncertainty. It is very small, reaching a value larger than 0.1% only below 0.15 GeV^2. The main cut applied to se-

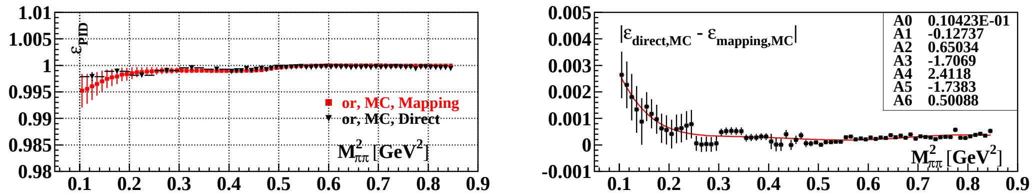

(a) (b)

Figure 31: (a) PID likelihood efficiencies evaluated by means of the single pion efficiency (mapping) and the direct method using $\pi^+\pi^-\gamma$ Monte Carlo sample.(b) Absolute difference between the two efficiencies. The red line represents a smooth parameterization of the difference.

lect the $\pi^+\pi^-\gamma$ sample in the $\pi - e$ PID efficiency evaluation is the cut on trackmass: $|M_{\rm trk} - m_\pi| < \Delta_{M_{\rm trk}}$ which, in the standard configuration, is $\Delta_{M_{\rm trk}} = 2.5$ MeV. An effect on the systematic uncertainty is thus estimated changing $\Delta_{M_{\rm trk}}$ according to the resolution in $M_{\rm trk}$(see Fig. 38(a)). The window has been opened up to 7.5 MeV, which correspond to about 1σ. The ratio

$$(\varepsilon_{\rm like}|\Delta'_{M_{\rm trk}})/(\varepsilon_{\rm like}|\Delta_{M_{\rm trk}})$$

is then evaluated, where $\Delta_{M_{\rm trk}}$ corresponds to the standard value $\Delta_{M_{\rm trk}} = 2.5$ MeV and $\Delta'_{M_{\rm trk}}$ corresponds to the modified window. The resulting contribution to the uncertainty was found to be always smaller than 0.1%, and is therfore negligible.

The `or`-configuration of the PID provides an high efficiency always above 99% and also guarantees a very small systematic uncertainty, smaller than 0.1% in the whole energy range. The only source of inefficiency comes from the association between the found cluster in the EMC and the track.

4.6 Unfolding for detector resolution

The correction for the detector resolution (often also called *unfolding*) in $M^2_{\pi\pi}$ takes place right after the correction for those efficiencies which are directly evaluated from data control samples and before correcting for the effective global efficiency (see Fig. 5). As this implies the passage from *reconstructed events*, which take into account the effects of the detector, to the *generated* (*true*) events,

$$(M^2_{\pi\pi})^{\rm rec} \to (M^2_{\pi\pi})^{\rm true},$$

subsequent corrections have to be performed in $(M^2_{\pi\pi})^{\rm true}$.
The number of events in a bin i of $(M^2_{\pi\pi})^{\rm true}$ can be related to the spectrum of observed events in bins j of $(M^2_{\pi\pi})^{\rm rec}$ via

$$N_i^{\rm true} = \sum_{j=1} P(N_i^{\rm true}|N_j^{\rm rec}) \cdot N_j^{\rm rec}, \tag{16}$$

where the sum runs over all bins of the reconstructed quantity $(M^2_{\pi\pi})^{\rm rec}$. The problem then consists in finding the quantity $P(N_i^{\rm true}|N_j^{\rm rec})$, which describes the bin-to-bin migration of events due to the reconstruction (and thus the detector resolution). This quantity determines the contribution of an observed event in bin j of $(M^2_{\pi\pi})^{\rm rec}$ to the bin i in $(M^2_{\pi\pi})^{\rm true}$.
Two methods have been used to evaluate $P(N_i^{\rm true}|N_j^{\rm rec})$:

1. Evaluating $P(N_i^{true}|N_j^{rec})$ directly from a sample of $\pi^+\pi^-\gamma$ Monte Carlo events, using the normalization condition

   $$\sum_{i=1}^{n_{\rm true}} P(N_i^{\rm true}|N_j^{\rm rec}) = 1.$$

   This method assumes that each observed event must come from one or more bins of the true values of $M^2_{\pi\pi}$. Then the correction reduces to a *matrix multiplication* of $P(N_i^{\rm true}|N_j^{\rm rec})$ with the vector of the observed spectrum in bins of $(M^2_{\pi\pi})^{\rm rec}$. However, a bias can be introduced due to the parameterization of $|F_\pi(s)|^2$ used in the Monte Carlo generation.

2. Evaluating $P(N_i^{\rm true}|N_j^{\rm rec})$ using Bayes' theorem [25]. This approach reduces the bias due to the parameterization for $|F_\pi(s)|^2$ used by defining $P(N_i^{\rm true}|N_j^{\rm rec})$ as

   $$P(N_i^{\rm true}|N_j^{\rm rec}) = \frac{P(N_j^{\rm rec}|N_i^{\rm true}) \cdot P_0(N_i^{\rm true})}{\sum_{l=1}^{n_{\rm true}} P(N_j^{\rm rec}|N_l^{\rm true}) \cdot P_0(N_l^{\rm true})},$$

   where the *initial probability* $P_0(N_l^{\rm true})$ is changed in an iterative procedure to become more and more consistent with the distribution of $N_i^{\rm true}$. Both $P_0(N_l^{\rm true})$ and the *response matrix* $P(N_j^{\rm rec}|N_i^{\rm true})$ are obtained from a Monte Carlo production of $\pi^+\pi^-\gamma$ events.[7]

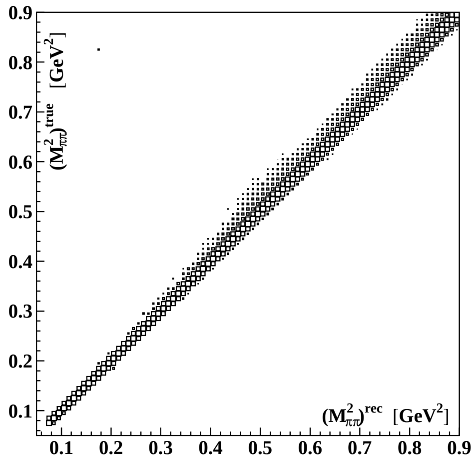

Figure 32: The probability matrix $P(N_i^{\rm true}|N_j^{\rm rec})$ (*smearing matrix*) which represents the correlation between generated (true) and reconstructed values for $M^2_{\pi\pi}$. The axis of the entries is in logarithmic scale.

In Fig. 32, the probability matrix $P(N_i^{\rm true}|N_j^{\rm rec})$ from Monte Carlo is shown. The high precision of the KLOE drift chamber results in an almost diagonal matrix.

Both methods give rather similar results. A smoothing of the spectrum to be unfolded is applied to avoid fluctuations caused by statistical limitations. The smoothing is performed only in the regions below 0.5 GeV^2 and between 0.7 and 0.95 GeV^2, and not in the region of the ρ-ω interference. The Bayesian method is applied in the analysis, while the matrix multiplication method is used to evaluate the systematic error.

Fig. 33 shows the outcome of the Bayes method, compared to the original input spectrum. The Bayesian approach with its iterative procedure, is less prone to introduce a bias from the $|F_\pi|^2$ parameterization. It has also been verified that the outcome of the procedure does not depend on the χ^2-like cutoff value used to terminate the iteration loop.

4.6.1 Systematic error on the unfolding procedure

As an estimate of the systematic uncertainty due to the unfolding effect the absolute value of the difference between the two methods is taken. This gives a significant contribution only near the ρ-ω interference region, where the small width of the ω meson introduces strong variations in the shape of $|F_\pi|^2$. In Fig. 34(b) the ratios between the unfolded over the input spectra are shown. The blue circles referr to the Bayesian approach, while the red ones correspond to the matrix approach. It can be seen that the deviation between the two methods affects only the region within $[0.6 - 0.62]$ GeV^2. The two points affected are the only ones which give a $> 2\sigma$ deviation from 1. The absolute difference between these two values and 1 is taken as the systematic uncertainty due to the unfolding procedure. The values are reported in Tab. 2. Please note that the unfolding has a negligible effect on the integral on $a_\mu^{\pi\pi}$, as it simply moves events between adjacent bins. Therefore, the

[7] The code used in the procedure can be found on the authors' webpage [26]

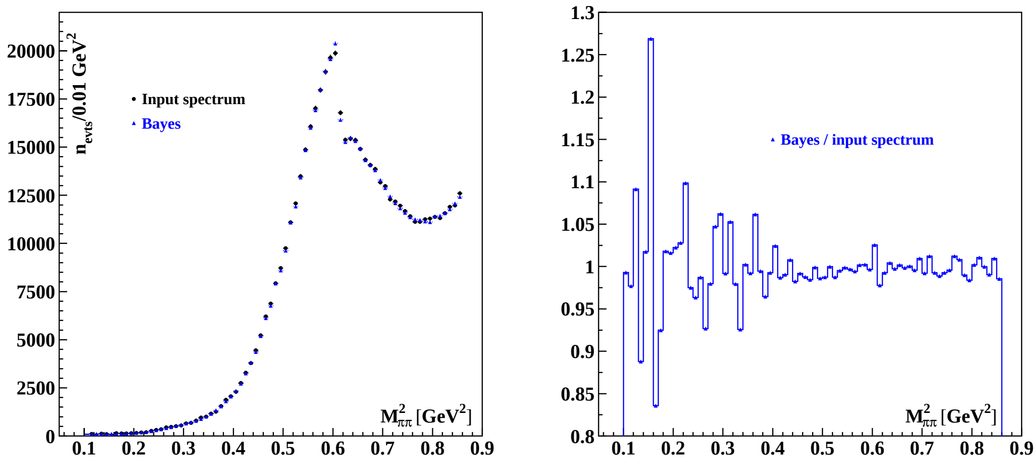

(a) (b)

Figure 33: Left: input spectrum (blue) in bins of $(M^2_{\pi\pi})^{\text{rec}}$ and unfolded spectrum for Bayesian method (black) in bins of $(M^2_{\pi\pi})^{\text{true}}$. Right: relative difference between the unfolded spectrum (true) and the input one (rec).

uncertainty given in Table 2 should not be taken into account when evaluating the integral on $a_\mu^{\pi\pi}$ from $\sigma_{\pi\pi}$.

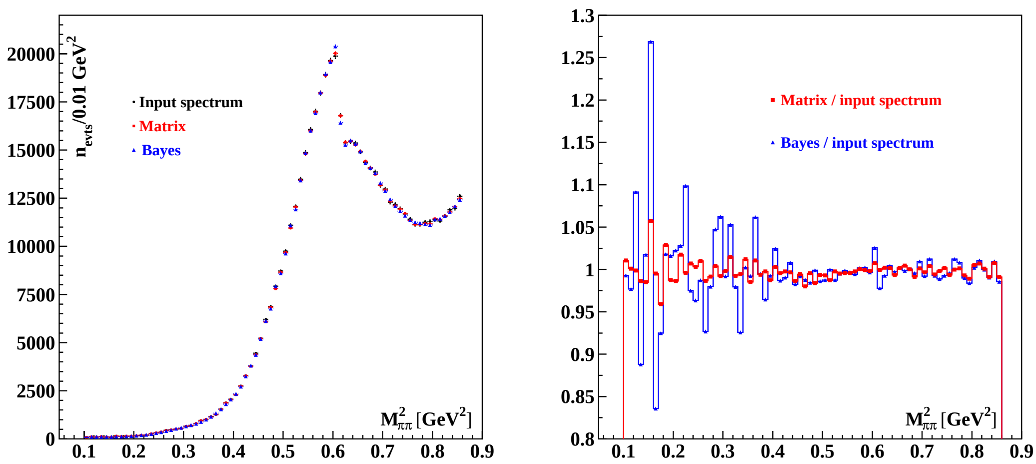

(a) (b)

Figure 34: In (a), the superimposition of the $M^2_{\pi\pi}$ input spectrum, black circles, and those one unfolded by the Bayesian and by the matrix approaches (blue squares and red triangles respectively), is shown. In (b) the ratio between the unfolded spectra over the input ones is drawn.

$M^2_{\pi\pi}$ (GeV^2)	0.605	0.615
$\delta_{unf}(\%)$	1.8	2.2

Table 2: Systematic error in % on $d\sigma(e^+e^- \to \pi^+\pi^-\gamma)/dM^2_{\pi\pi}$, $\sigma(e^+e^- \to \pi^+\pi^-)$ and $|F_\pi|^2$ due to the correction for detector resolution in 0.01 GeV^2 intervals. The indicated values for $M^2_{\pi\pi}$ represent the center of the bin. Outside this interval the effect is negligible.

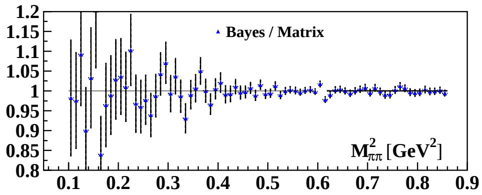

Figure 35: Ratio of Bayes-unfolded spectrum over matrix-unfolded spectrum. Omitting the 2 points between 0.6 and 0.62 GeV^2, a linear fit gives a result which is compatible with "1.000" (black lines).

4.7 The global efficiency

The *global efficiency* stands for the ratio

$$\varepsilon_{\text{glob}} = \frac{(dN_{\pi^+\pi^-\gamma}\,|\,\text{all analysis cuts})/(d(M^2_{\pi\pi})^{\text{true}})}{(dN_{\pi^+\pi^-\gamma}\,|\,\text{full inclusive})/(d(M^2_{\pi\pi})^{\text{true}})}. \tag{17}$$

Due to the fact that the unfolding for detector resolution effects has been already applied the $\pi^+\pi^-$-system invariant mass at Monte Carlo generated level, $(M^2_{\pi\pi})^{\text{true}}$, is considered. By means of the full set of analysis cuts, we take into account:

- corrections for the geometrical acceptance:

$$50^\circ < \theta_\pi < 130^\circ\ ;\ 45^\circ < \theta_{\text{Miss}} < 135^\circ\ ;\ 50^\circ < \theta_\gamma < 130^\circ\ ;\ E_\gamma > 20\ \text{MeV};$$

- signal loss due to selection cuts:

$$120\ \text{MeV} < M_{\text{trk}} < M_{\text{trk}}(M^2_{\pi\pi})\ \text{as in Eq. 2;}\ \Omega < \Omega(M^2_{\pi\pi})\ \text{as in Eq. 4;}$$

- signal loss due to data quality requests on momentum:

$$|p_T| > 160\ \text{MeV or}\ |p_z| > 90\ \text{MeV}\ ;\ |\vec{p}| > 200\ \text{MeV};$$

- corrections for tracking efficiency according to the request of

$$\rho_{\text{PCA}} = \sqrt{x^2_{\text{PCA}} + y^2_{\text{PCA}}} < 8\ \text{cm}\ ;\ |z_{\text{PCA}}| < 12\ \text{cm};\ \rho_{\text{FH}} < 50\text{cm};$$

- signal loss due to the cut on the distance between the clusters associated with the two charged tracks:

$$d_{\text{clu}} = \sqrt{(\vec{x}_{\text{clu}+} - \vec{x}_{\text{clu}-})^2} < 90\text{cm}.$$

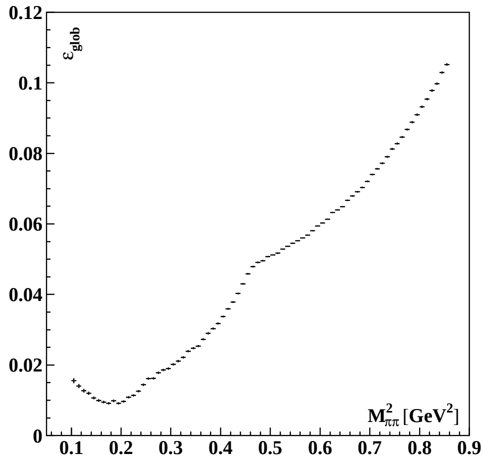

Figure 36: Effective global efficiency according to the ratio of Eq. 17 and the cuts described in the text.

The $\pi^+\pi^-\gamma$ spectrum obtained after all selection cuts (Sec. 3.2), after the background subtraction (Sec. 4.2.1) and the unfolding procedure (Sec. 4.6) is then corrected by the global effective efficiency. The value of $\varepsilon_{\mathrm{glob}}$ is shown in Fig. 36(a). The slope is mainly due to the large angle geometrical acceptance cuts.

The global efficiency for the differential cross section is defined in a similar way, with the exception that it is conditioned on the presence of at least one photon with $(50^\circ < \theta_\gamma < 130^\circ)$ and $E_\gamma > 20$ MeV in the event:

$$\varepsilon_{\mathrm{glob,cond}} = \frac{(dN_{\pi^+\pi^-\gamma}\,|\,\text{all analysis cuts})/(d(M^2_{\pi\pi})^{\mathrm{true}})}{(dN_{\pi^+\pi^-\gamma}\,|\,\text{a }\gamma\text{ with }(50^\circ < \theta_\gamma < 130^\circ\ ;\ \mathrm{E}_\gamma > 20\ \mathrm{MeV};))/(d(M^2_{\pi\pi})^{\mathrm{true}})}. \tag{18}$$

Fig. 37 shows this efficiency. It is by definition larger than the one in Fig. 36.

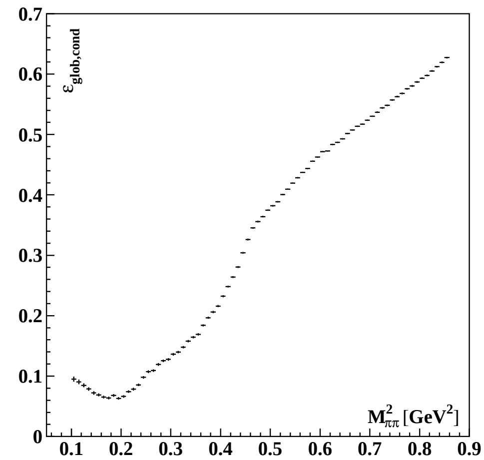

Figure 37: Global efficiency conditioned on the request that of at least one photon with $(50^\circ < \theta_\gamma < 130^\circ$ and $E_\gamma > 20$ MeV is present in the event, see Eq. 18.

4.7.1 Systematics on trackmass cut

The systematic uncertainties due to trackmass enter in two points of the analysis, namely: (*i*) in the background estimation procedure (described in Sec. 4.2.1) and (*ii*) in the signal selection cut.

To evaluate the systematic uncertainty of the trackmass cut a data-Monte Carlo *double ratio* check is applied.[8] It consists of

- shifting each single cut (*shifted cut*) with respect to the value used in the analysis (*standard cut*), leaving unchanged all the others. The shift is about 1σ of the resolution of the variable in which the cut is applied;
- running the full selection procedure on data, and the Monte Carlo $\pi^+\pi^-\gamma$, $\mu^+\mu^-\gamma$, $e^+e^-\gamma$ and $\pi^+\pi^-\pi^0$ samples;
- subtracting the residual background events from the data sample, according to the background subtraction procedure, explained in Sec. 4.2.1, and build the ratio between data and $\pi^+\pi^-\gamma$ Monte Carlo in the shifted cut over the standard cut conditions;
- performing the double ratio of the spectra, data over $\pi^+\pi^-\gamma$ Monte Carlo

$$R_{\rm cut}(M^2_{\pi\pi}) = \frac{(dN^{\rm data}/dN^{\rm MC})|_{\text{shifted cut}}}{(dN^{\rm data}/dN^{\rm MC})|_{\text{standard cut}}}(M^2_{\pi\pi}), \tag{19}$$

  where $dN^{\rm data,MC}$ is the number of events binned in $M^2_{\pi\pi}$ and $dN^{\rm data}$ is the background subtracted event yield.

By means of this double ratio it is possible to check both the changing of the spectrum caused by modifying a specific selection cut and, at the same time, the data-Monte Carlo agreement in that cut.

In Fig. 38(a) the resolution of the trackmass variable is shown, obtained from the difference between the generated and the reconstructed value using Monte Carlo $\pi^+\pi^-\gamma$ sample. In the reconstructed quantities the smearing and the shifting of momenta, described in [8], have been applied. The distribution is fitted with two Gaussian functions, shown in red. The first Gaussian fit has a standard deviation $\sigma \simeq 3$ MeV, which is taken as the resolution of the trackmass variable, since the other Gaussian function is needed only for a small fraction of events.

First a shift of ± 3.5 MeV is applied to the upper trackmass cut, while the lower is left unchanged. After that the lower cut is shifted while the upper cut is untouched.In Fig. 38(b) the standard cuts, described by the black curves, and the shifted ones, in red, are shown on the data distribution of $M_{\rm trk}$ vs. $M^2_{\pi\pi}$.

The results of the double ratios are shown in Fig. 39(a) and in Fig. 39(b), for the upper cuts and to the lower cut shifted, respectively. The discrepancies from 1 are very small, suggesting a small systematic uncertainty, especially in the region between 0.4 and 0.8 GeV^2. To take into account the not constant behaviour of the double ratio in $M^2_{\pi\pi}$, a fit with a third order polynomial functions is performed for each ratio, represented by the red lines.

[8]This approach will be used also to estimate the systematic errors of other selection cuts.

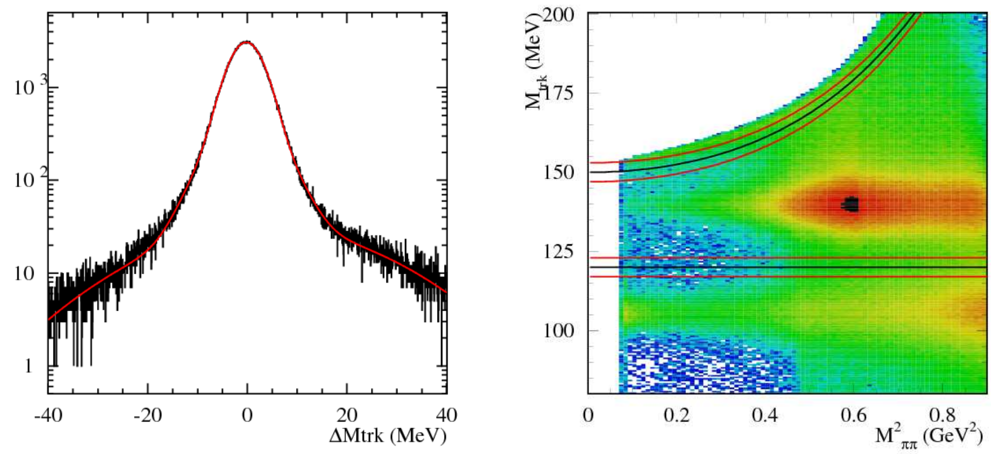

(a) (b)

Figure 38: In (a), the resolution of trackmass variable, estimated as the difference between the reconstructed and the "true" values of the $\pi^+\pi^-\gamma$ Monte Carlo sample, is shown. The reconstructed quantities take into account the tuning and the smearing procedure described in [8]. In (b), the $M_{\rm trk}$ vs. $M^2_{\pi\pi}$ distribution from data is shown. The black lines describe the standard analysis cuts, while the red ones the shifted cuts applied to estimate the systematic error.

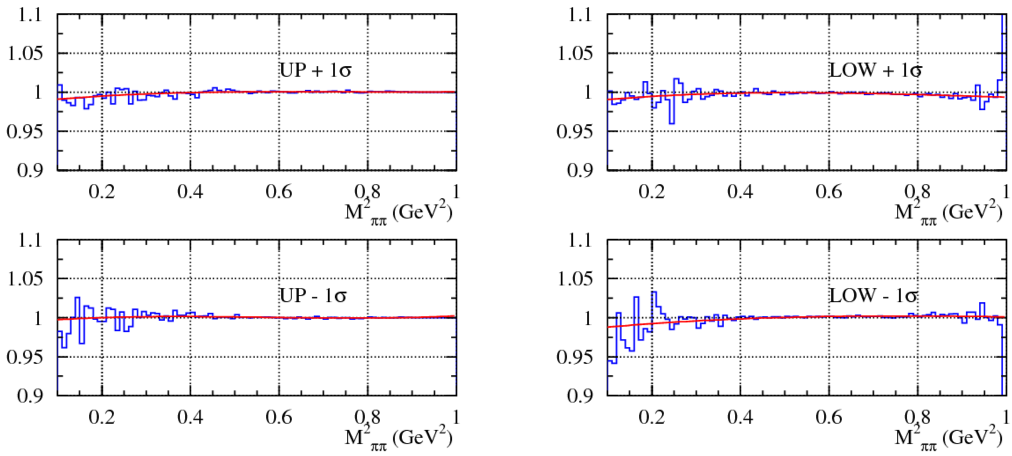

(a) (b)

Figure 39: Double ratio results for shifting the upper, (a), and the lower trackmass cut, (b). The red curves represents the third power functions used to fit the double ratios.

As systematic error associated to the trackmass cut the maximum deviation from 1 of the four fitting functions, which are used to fit the double ratios, is taken, see Fig. 40. The error reaches up to ca. 1% close to the $2m_\pi$-threshold and decreases down to 0.1% on the ρ-peak.

The uncertainty is very small thanks to: (i) the good data-Monte Carlo agreement, obtained after the fine calibration and tuning of track parameters, described in [8];

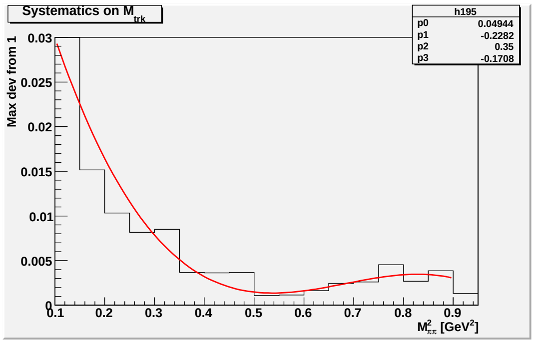

Figure 40: Maximum deviation from 1 among the four fitting functions shown in Fig. 39(a) and Fig. 39(b).

and (*ii*) the relatively loose cuts applied in the analysis. Cutting far away from steep slopes in the variable shapes, where the variation of the spectrum is smooth over the variable interval, allows to get a small systematic uncertainty.

4.7.2 Ω-angle

For ISR events with one photon, which represent the dominant part of the ISR spectrum, the emitted photon and the missing momentum of the track have the same direction. Exploiting this information, together with the photon detection, it is possible to reject background from $\pi^+\pi^-\pi^0$ events, for which the direction of the photons produced by the π^0 decay is uniformly distributed.
The Ω-*angle* is defined as the angle between the track missing momentum and the momenta of the detected photon. In the case of more than one photon present in the event, all the combinatorial combinations are built and the smallest value of the Ω-angle is chosen:

$$\Omega = \min(\Omega_i)$$
$$\Omega_i = \mathrm{acos}\left(\frac{\vec{p}_{\mathrm{miss}} \cdot \vec{p}_{\gamma,i}}{|\vec{p}_{\mathrm{miss}}||\vec{p}_{\gamma,i}|}\right), \tag{20}$$

where $\vec{p}_{\mathrm{miss}}$ stands for the track missing momentum and $\vec{p}_{\gamma,i}$ is the momentum of the i^{th} photon. The Ω-angle distribution peaks at zero for signal events while it is off-zero for events with higher photon multiplicity, as can be seen in Fig. 41 for $\pi^+\pi^-\gamma$ and $\pi^+\pi^-\pi^0$ Monte Carlo samples. The plot shows events normalized to the same integrated luminosity after the Large Angle acceptance cuts and the `ppgtag` pre-filter.
The spread of the $\pi^+\pi^-\gamma$ peak is not only due to resolution, but mainly due to the NLO events. Since at high values of $M^2_{\pi\pi}$, the amount of NLO-ISR processes is comparable to the amount of LO events, a $M^2_{\pi\pi}$-dependent cut is applied (see Fig. 42(a))

$$\Omega < (2. + e^{4.M^2_{\pi\pi}/GeV^2})^\circ, \tag{21}$$

to preserve signal events at large values of $M^2_{\pi\pi}$. A further cut on $\Omega < 90^\circ$ is imposed.
The inefficiency of the cut imposed on signal events is on the level of 2% below 0.3 GeV^2 and reaching up to 6% above, as can be seen in Fig. 43(a). In Fig. 43(b) the percentage of $\pi^+\pi^-\pi^0$ events which survive the Ω-angle cut (after passing the `ppgtag` pre-filter and trackmass cuts) is shown. The rejection power on $\pi^+\pi^-\pi^0$ is

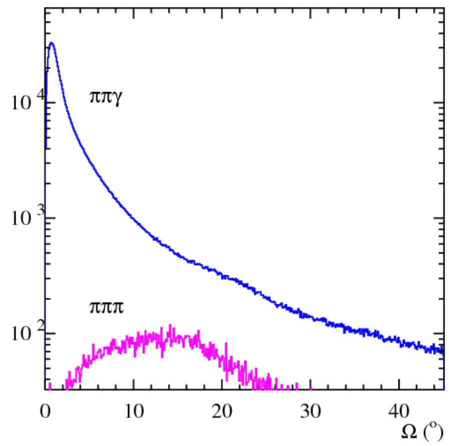

Figure 41: Distributions of the Ω-angle for $\pi^+\pi^-\gamma$ (blue histogram), and $\pi^+\pi^-\pi^0$ (pink histogram), from Monte Carlo samples. The events shown have passed the `ppgtag` pre-filter and Large Angle acceptance cuts. They are inclusive in $M^2_{\pi\pi}$ and normalized to the same integrated luminosity. The signal is peaked at small values of Ω-angle, while background events from $\pi^+\pi^-\pi^0$ are situated at higher value.

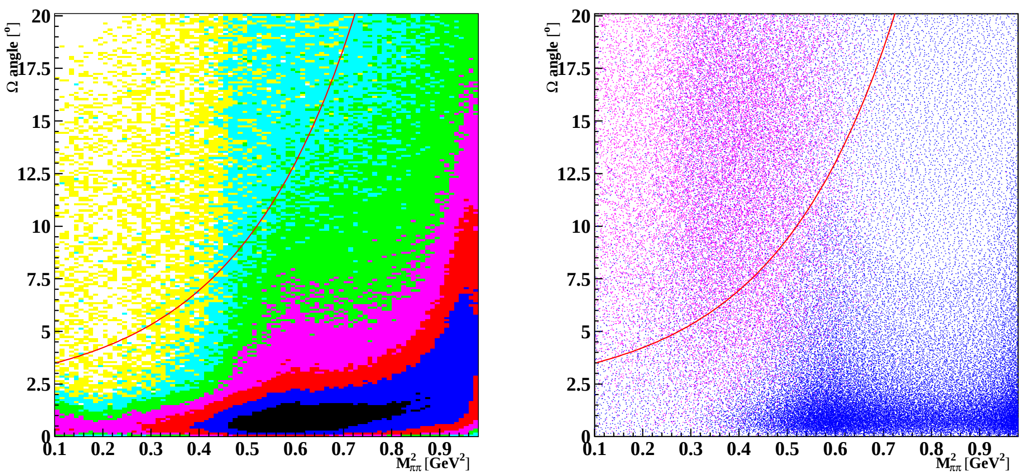

(a) (b)

Figure 42: Ω-angle distribution for the data sample, in (a), and for $\pi^+\pi^-\gamma$ (blue dots) and $\pi^+\pi^-\pi^0$ (pink dots) Monte Carlo samples, in (b), after Large Angle acceptance cut and the `ppgtag` pre-filter. The events are normalized to the integrated luminosity of the data sample. The spreading for the signal events at high values of $M^2_{\pi\pi}$ due to NLO-ISR processes is visible. The red line represents the cut applied, see Eq. 4.

around 80 - 90% up to 0.7 GeV^2. Above 0.7 GeV^2 the $\pi^+\pi^-\pi^0$ contamination is negligible.

The Ω-angle can not distinguish among different kind of ISR processes, thus it does not help in further rejecting $\mu^+\mu^-\gamma$ or $e^+e^-\gamma$ events.

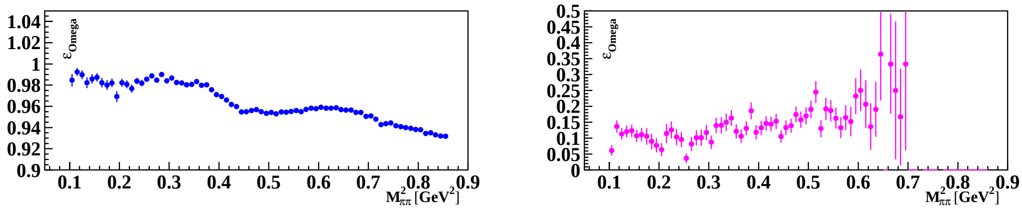

(a) (b)

Figure 43: (a) Efficiency of Ω-angle for $\pi^+\pi^-\gamma$ events; (b), percentage of residual $\pi^+\pi^-\pi^0$ events surviving the cut. The ratios have been evaluated using 1×10^7 Monte Carlo events.

4.7.3 Systematics on Ω-angle cut

The same "double ratio approach" used for M_{trk}, see Sec. 4.7.1 and Eq. 19, is applied to evaluate the systematic uncertainty on the Ω-angle cut.

To take into account the broadening of the Ω-angle distribution with the increasing of the energy, see Fig. 42, the root mean square as a function of $M^2_{\pi\pi}$ has been evaluated, $rms(M^2_{\pi\pi})$. Thus, to obtain $(dN^{\mathrm{data}}/dN^{\mathrm{MC}})|_{\mathrm{shifted\ cut}}$, the standard cut in Ω-angle is shifted by $\pm rms(M^2_{\pi\pi})$. In Fig. 44 the blue circles represent the values of the rms evaluated in slices of $M^2_{\pi\pi}$. The red line shows a linear fit.

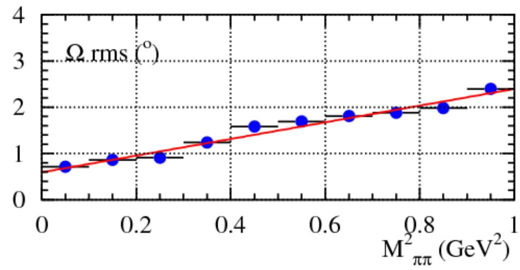

Figure 44: The values of the Ω-angle rms evaluated in slices of $M^2_{\pi\pi}$ are shown, together with the linear fit, in red.

Fig. 45 shows the Ω-angle vs. s_π distribution for data. Superimposed to the spectrum, in black, the standard cut applied in the analysis, see Eq. 4, and, in red, the cut shifted by $+rms(M^2_{\pi\pi})$ and $-rms(M^2_{\pi\pi})$ are drawn.

The double ratio results are shown in Fig. 46: in the upper plot the shifting of the standard Ω-angle cut by $+rms(M^2_{\pi\pi})$ and the lower plot by $-rms(M^2_{\pi\pi})$. The shifts affect the spectrum only below 0.4 GeV^2, while at higher energy the deviation from 1 is negligible. The low statistics, denoted by the scattering of the histograms, also plays a role at the low energy values, however a small trend in the ratios is visible. To consider that, a third power polynomial function fit is applied, indicated by the red lines, from the threshold up to 0.4 GeV^2, while above that energy a linear fit is used. The maximum deviation from 1 between the two fitting functions is taken as the systematic error, see Fig. 47. The systematic uncertainty is negligible above 0.4 GeV^2 and it reaches ca. 2% at the $2m_\pi$-threshold. Thanks to the good data-Monte Carlo agreement and to the little $\pi^+\pi^-\pi^0$ contamination in the off-peak data, it is possible to keep small the uncertainty due to the Ω-angle cut. The almost $\pi^+\pi^-\pi^0$

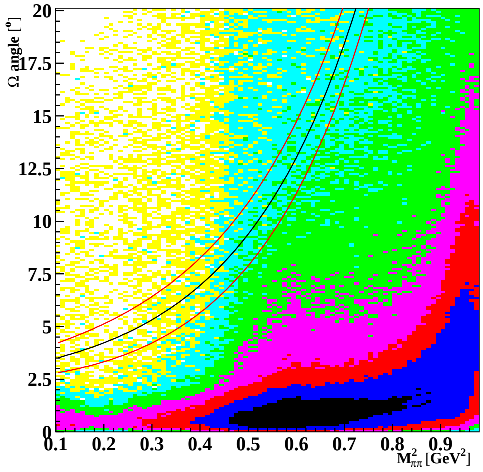

Figure 45: The Ω-angle vs. $M^2_{\pi\pi}$ distribution for data sample is shown. The black line represents the standard cut applied in the analysis, see Eq. 4, and the red ones the standard cut shifted by $\pm rms(M^2_{\pi\pi})$.

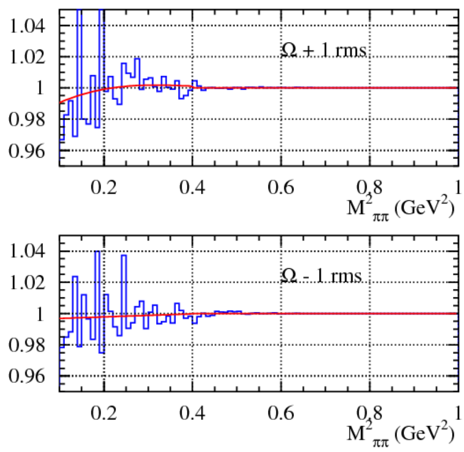

Figure 46: Double ratio results shifting the Ω-angle cut by adding, in the upper plot, or subtracting, in the lower one, 1 $rms(M^2_{\pi\pi})$.

free data sample permits to apply a much looser cut in the Ω-angle with respect to the one applied for 2002 on-peak data. This avoids a considerable signal lost (which is an issue at the $\pi^+\pi^-$-threshold) and allows to apply the cut only in a region where the tails of the signal distributions are smooth.

4.7.4 Tracking efficiency

The tracking efficiency takes into account not only the pure efficiency of the reconstruction algorithm, but also the effects due to the pion decay and nuclear interactions.[9]

[9]If only the tracking reconstruction algorithm efficiency was considered, the tracking efficiency would be actually 100%, since given some hits in the DC the pattern recognition procedure is

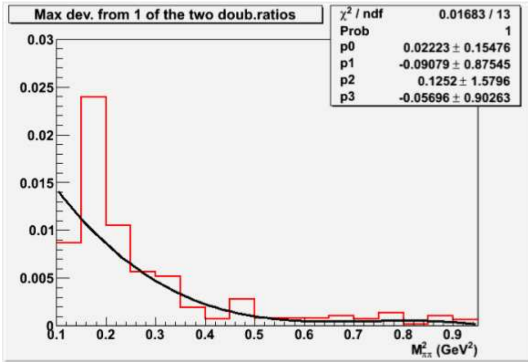

Figure 47: Systematic uncertainty taken as the maximum deviation from 1 for the double ratios of the Ω systematic uncertainty.

The efficiency of reconstructing the pion track is measured per single charge, both with Monte Carlo and data samples, conditioned to the presence of a tagging track of opposite sign. The efficiency to find the pion track of a given sign is parameterized as a function of momentum and polar angle slices of the expected track.
A sample of ca. 50 pb^{-1} of data and of effective 300 pb^{-1} of Monte Carlo is analyzed.[10] The efficiency is evaluated directly from signal events selected from these samples.
The selected events consist in

- at least one *tagging track*, satisfying the following requests:
  - * the polar angle $50° < \theta_{\text{tag}} < 130°$;
  - * the radial position of the first hit in the drift chamber $\rho_{\text{FH}} = \sqrt{x^2_{\text{FH}} + y^2_{\text{FH}}} <$ 30 cm and of the last hit $\rho_{\text{LH}} = \sqrt{x^2_{\text{LH}} + y^2_{\text{LH}}} > 180$ cm;
  - * the extrapolated point of closest approach to the interaction point with $\rho_{\text{PCA}} = \sqrt{x^2_{\text{PCA}} + y^2_{\text{PCA}}} < 8$ cm and with $|z_{\text{PCA}}| < 7$ cm;
  - * an associated cluster (after extrapolating the track to the calorimeter and looking for a cluster within a sphere of radius = 90 cm) recognized as a pion by the $\pi - e$ PID function, i.e. $\log \mathcal{L}_\pi/\mathcal{L}_e > 0.3$;
- 1 and only 1 photon with
  - * the polar angle $50° < \theta_\gamma < 130°$;
  - * the energy $E_\gamma > 50$ MeV;
- cut on M_{miss}
  - * the missing mass, M_{miss}, evaluated using the 4-momentum conservation on momenta of the photon and the tagging track (having imposed the mass of the pion to the tagging track), must satisfy $|M_{\text{miss}} - m_\pi| <$ 20 MeV.

almost always able to find a track.

[10]The Monte Carlo signal sample has been produced with a scale factor of 6 in cross section with respect to data, giving in this way $L_{\pi\pi\gamma} = 6 \times L_{\text{data}}$.

An event is defined efficient, if a fitted track with opposite charge with respect to the tagging one is found. The *expected track* to be considered an "efficient" track has to satisfy the following conditions:

* the radial position of the first hit: $\rho_{\mathrm{FH}} < 50$ cm;
* the position of the point of closest approach: $\rho_{\mathrm{PCA}} < 8$ cm and $|z_{\mathrm{PCA}}| < 12$ cm.

These conditions correspond to the same requests applied in the analysis.
The single track efficiency is evaluated for 6 bins from 200 MeV to 500 MeV in the expected track momentum and in 4 slice in polar angle within $|90° - \theta_{\mathrm{exp}}| < 40°$, both for data, $\varepsilon^{\mathrm{data}}_{\mathrm{trk}}(\theta_{\pi^\pm}, p_{\pi^\pm})$, and for Monte Carlo, $\varepsilon^{\mathrm{MC}}_{\mathrm{trk}}(\theta_{\pi^\pm}, p_{\pi^\pm})$. The results are shown in Fig. 48 and in Fig. 49 for positive and negative track, respectively. Data are represented by red and Monte Carlo by black circles.

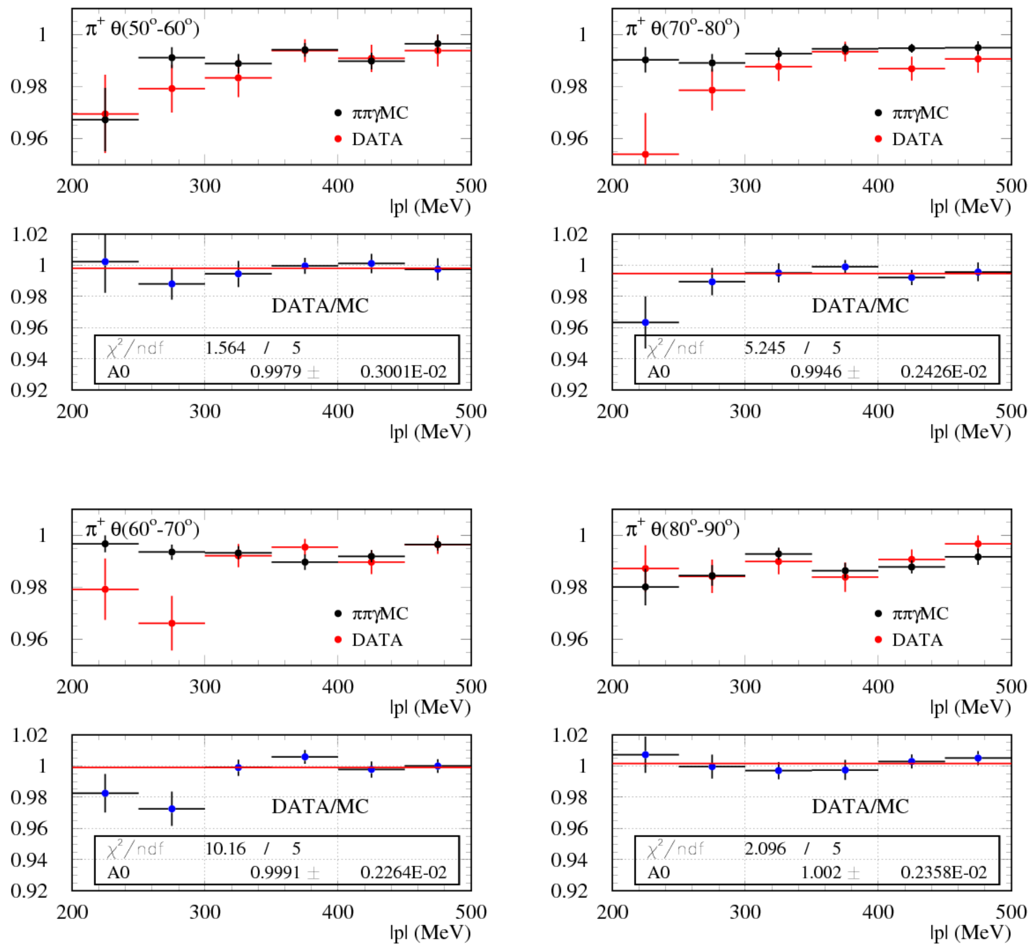

Figure 48: Single track efficiency for π^+ sample as a function of momentum in slices of polar angle. Data are represented in red points and Monte Carlo in black points. Ratios between the efficiencies from data and from simulation are also shown, for each slice in polar angle. The red straight line is the linear fit performed to obtain the correction factors $\zeta(\theta_{\pi^+})$ used to evaluate the data efficiency as a function of s_π, $\varepsilon^{\mathrm{data}}_{\mathrm{trk}}(s_\pi)$.

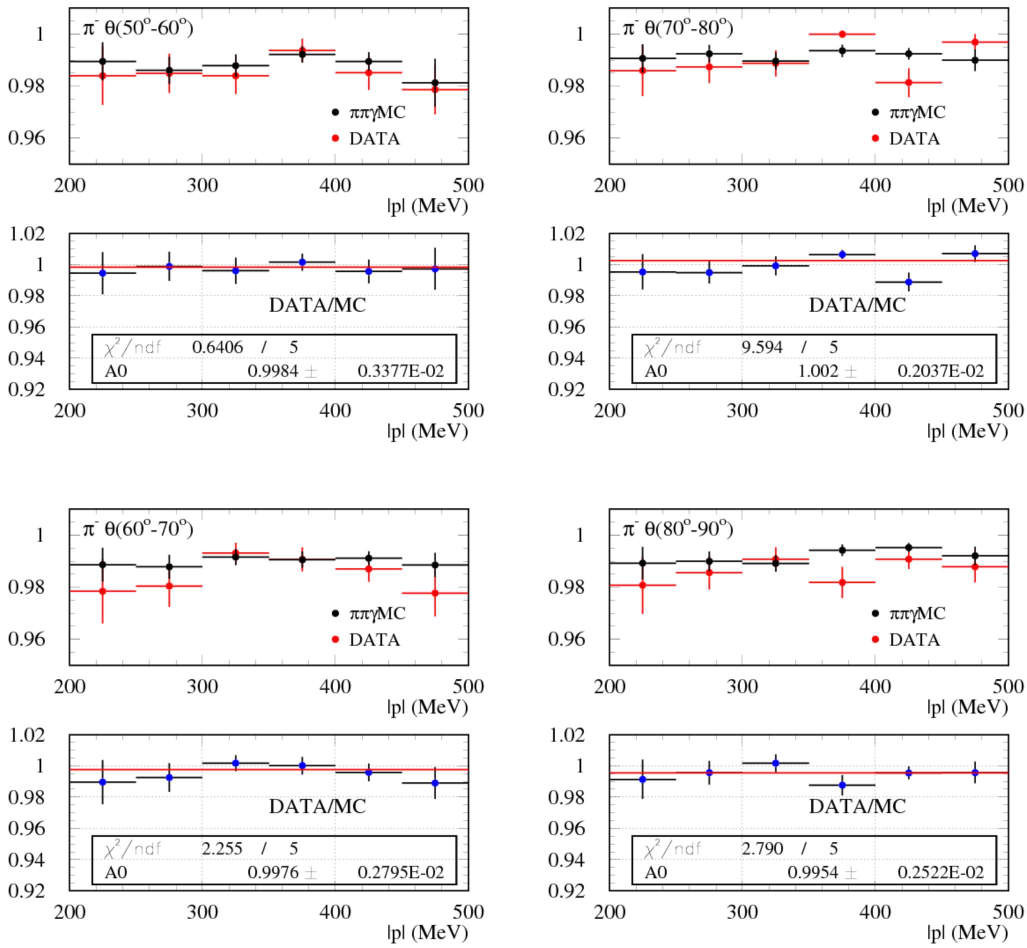

Figure 49: Single track efficiency for π^- sample as a function of momentum in slices of polar angle. Data are represented in red points and Monte Carlo in black points. Ratios between the efficiencies from data and from simulation are also shown, for each slice in polar angle. The red straight line is the linear fit performed to obtain the correction factors $\zeta(\theta_{\pi^-})$ used to evaluate the data efficiency as a function of s_π, $\varepsilon_{\rm trk}^{\rm data}(s_\pi)$.

For each slice of $\theta_{\pi^\pm}$ the ratio of the tracking efficiencies from data and Monte Carlo as a function of $p_{\pi^\pm}$ is computed:

$$c(\theta_{\pi^\pm}, p_{\pi^\pm}) = \frac{\varepsilon_{\rm trk}^{\rm data}(\theta_{\pi^\pm}, p_{\pi^\pm})}{\varepsilon_{\rm trk}^{\rm MC}(\theta_{\pi^\pm}, p_{\pi^\pm})}, \tag{22}$$

represented by the blue circles in the lower plots of Fig. 48 and Fig. 49 for the positive and negative track, respectively. The ratios result to be almost flat for the considered momentum range and in each slice of polar angle a linear fit is performed, whose parameter, $\zeta(\theta_{\pi^\pm})$, is used to obtain $\varepsilon_{\rm trk}(M^2_{\pi\pi})$. In Fig. 48 and Fig. 49 the linear fit is reported by the red line and the fit results are also indicated.

The tracking efficiency as a function of $M^2_{\pi\pi}$ is obtained by mapping these single pion efficiencies with generated kinematics from Monte Carlo. For a given bin in $M^2_{\pi\pi}$ (width $= 0.01$ GeV^2), the tracking efficiency is an average over the n different configurations of $(\theta_{\pi^+}, p_{\pi^+}, \theta_{\pi^-}, p_{\pi^-})$ contributing to that bin:

$$\varepsilon_{\rm trk}(M^2_{\pi\pi}) = \frac{1}{N}\sum_{k=1}^{n} \nu_k \ \varepsilon_k, \tag{23}$$

where N is the number of Monte Carlo events used to compute the frequency ν_k of the occurrence of a certain k configuration.

To evaluate the efficiency per event for the Monte Carlo sample, i.e. to perform the passage

$$\varepsilon^{\rm MC}_{\rm tk}(\theta_{\pi^\pm}, p_{\pi^\pm}) \rightarrow \varepsilon^{\rm MC}_{\rm trk}(M^2_{\pi\pi}),$$

the input, ε_k, to Eq. 23 is

$$\varepsilon_k = \varepsilon^{\rm MC}_{\rm trk}(\theta_{\pi^+}, p_{\pi^+})\varepsilon^{\rm MC}_{\rm trk}(\theta_{\pi^-}, p_{\pi^-}). \tag{24}$$

To get the efficiency for data as a function of $M^2_{\pi\pi}$

$$\varepsilon^{\rm data}_{\rm trk}(\theta_{\pi^\pm}, p_{\pi^\pm}) \rightarrow \varepsilon^{\rm data}_{\rm trk}(M^2_{\pi\pi})$$

the correction factors, $\zeta(\theta_{\pi^\pm})$, are used, which have been obtained by fitting the data-Monte Carlo ratio (see Fig. 48 and Fig. 49). The parameter ε_k is given by:

$$\varepsilon_k = \zeta(\theta_{\pi^+})\varepsilon^{\rm MC}_{\rm trk}(\theta_{\pi^+}, p_{\pi^+}) \cdot \zeta(\theta_{\pi^-})\varepsilon^{\rm MC}_{\rm trk}(\theta_{\pi^-}, p_{\pi^-}). \tag{25}$$

The choice of using in both the two evaluations $\varepsilon^{\rm MC}_{\rm trk}(\theta_{\pi^\pm}, p_{\pi^\pm})$ from Monte Carlo – properly corrected by $\zeta(\theta_{\pi^\pm})$ in the case of data – is motivated by the bigger statistics of the simulation with respect to the data one. In Fig. 50(a) the results for $\varepsilon^{\rm data}_{\rm trk}$ is shown. In Fig. 50(b) a data (red points) and Monte Carlo (black points) comparison (upper plot) and the ratio of the two (lower plot) are presented. A good agreement between experimental sample and simulation is found, giving a correction on $\Delta\varepsilon$ due to tracking of ca. 0.3%.

Since in the effective global efficiency approach the tracking reconstruction is included in $\varepsilon_{\rm glob}$, the spectrum is bin-by-bin corrected by the data–Monte Carlo difference for the tracking efficiency. The data-Monte Carlo discrepancy is mainly due to a not perfect simulation of split and spiralizing tracks in the simulation. An example of this kind of events is shown in Fig. 51 where a front and a side view of the KLOE detector display are shown. To reduce the presence of these events, which happen essentially only for low momentum tracks, a cut $|\vec{p}_{trk}| > 200$ MeV is applied. This cut introduces an inefficiency for signal events of ca. 15%.

Several test have been performed to verify the result on the tracking efficiency. Possible influences from the trigger efficiency and from the presence of residual $\mu^+\mu^-\gamma$ and $\pi^+\pi^-\pi^0$ events have been checked.

In addition to the conditions described above, the tagging track has been required also to trigger the event. This is fulfilled by ca. 30% of the events. The "self triggering" requirement causes a negligible change of ca. 0.1% on $\varepsilon_{\rm trk}(M^2_{\pi\pi})$, coherently on data and Monte Carlo, leaving unchanged the agreement between the two.

Defining α as the angle between the missing momentum – with respect to the tagging track and the detected photon – and the found expected track momentum (see Fig. 52), one can cut on that variable to reject possible residual $\pi^+\pi^-\pi^0$ events. The 3π sample is already strongly reduced by the cut on missing mass ($|M_{\rm miss} - m_\pi| <$

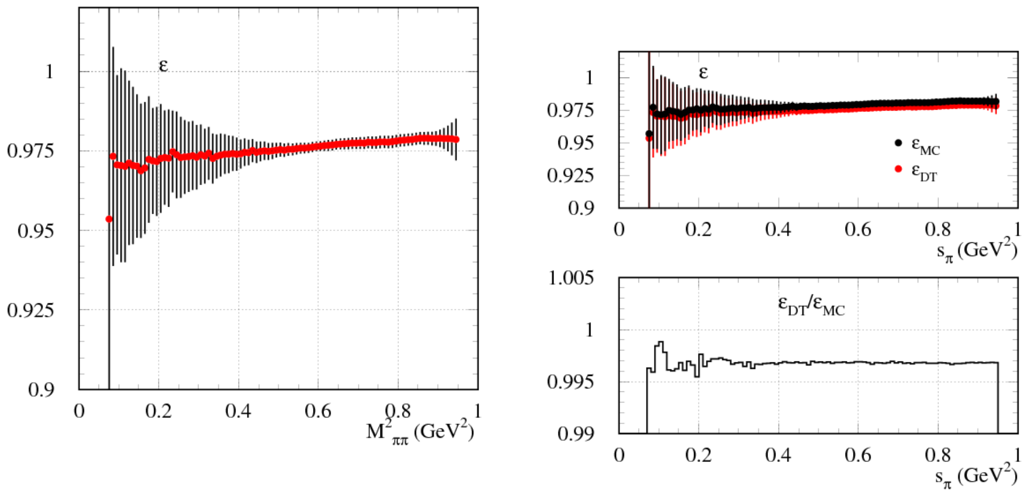

(a) (b)

Figure 50: In (a) the tracking efficiency for data, evaluated according to Eq. 25 is shown. The comparison between data and Monte Carlo is visible in (b, upper) and the data–Monte Carlo ratio is drawn in (b, lower). The spectrum is bin-by-bin corrected for this ratio.

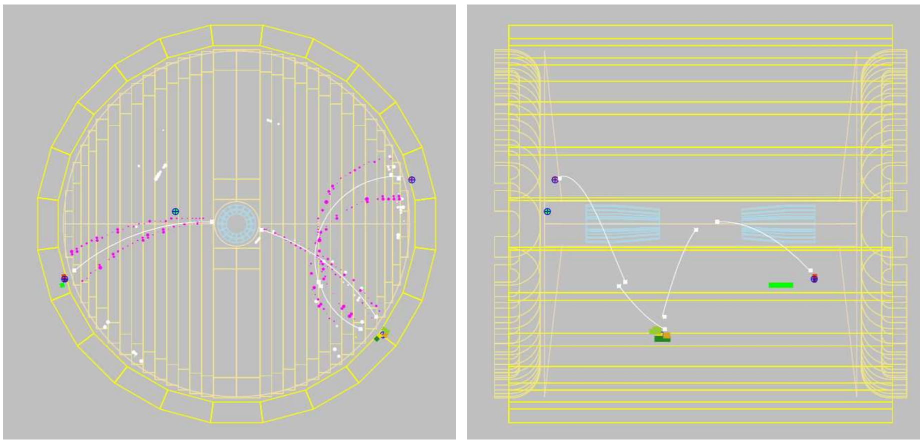

(a) (b)

Figure 51: A front (a) and side (b) view of the KLOE detector of a typical data event where a split track is present. These events are not reproduced in a perfect way by the detector simulation.

20 MeV), resulting in about 10^{-3} less events than for the signal. Even if a priori there is no reason to expect a different tracking efficiency between the $\pi^+\pi^-\gamma$ and the $\pi^+\pi^-\pi^0$ samples (since the tracks are generated by the same kind of charged particle), cuts on α, from 5° to 20°, have been applied to test this hypothesis. Only negligible differences in the absolute efficiency are found, leaving unchanged the data-Monte Carlo ratios.

4.7.5 Systematic error on the tracking efficiency

The main cause of inefficiency consists in the fact that the candidate track does not satisfy one of the following conditions

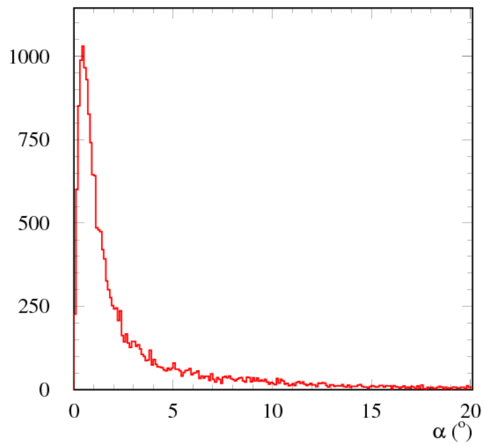

Figure 52: Angle between the missing momentum, from the tagging track and the photon, and the candidate track found for data sample.

* $\rho_{\mathrm{FH}} < 50$ cm;
* $\rho_{\mathrm{PCA}} < 8$ cm;
* $|z_{\mathrm{PCA}}| < 12$ cm.

To evaluate the systematic uncertainty of the tracking efficiency each of the conditions listed above has been moved, keeping the others unchanged. The systematic uncertainty is then obtained from the ratio

$$(\varepsilon^{\mathrm{data}}_{\mathrm{trk}}|cut'_{(\rho_{\mathrm{FH}},\rho_{\mathrm{PCA}},|z_{\mathrm{PCA}}|)})/(\varepsilon^{\mathrm{data}}_{\mathrm{trk}}|cut_{(\rho_{\mathrm{FH}},\rho_{\mathrm{PCA}},|z_{\mathrm{PCA}}|)}), \tag{26}$$

where the efficiency values $\varepsilon_{\mathrm{trk}}$ are obtained directly from the data sample, and *cut* indicates the conditions on first hit and point of closest approach applied to evaluate the efficiency, while *cut′* stays for the shifted requests, either on the point of closest approach or on the first hit. Each ratio is fitted with a third order polynomial function.
The radial position of the first hit inside the drift chamber is moved from a minimal value of 45 cm to a maximum of 60 cm. The values of the ratios

$$(\varepsilon^{\mathrm{data}}_{\mathrm{trk}}|_{\rho_{\mathrm{FH}}<45})/(\varepsilon^{\mathrm{data}}_{\mathrm{trk}}|_{\rho_{\mathrm{FH}}<50}) \text{ and } (\varepsilon^{\mathrm{data}}_{\mathrm{trk}}|_{\rho_{\mathrm{FH}}<60})/(\varepsilon^{\mathrm{data}}_{\mathrm{trk}}|_{\rho_{\mathrm{FH}}<50}),$$

are shown in the upper and lower plot of Fig. 53.
The conditions on the point of closest approach have been moved from 6 cm to 10 cm, for ρ_{PCA}, and from 10 cm to 14 cm, for $|z_{\mathrm{PCA}}|$. In Fig. 54 and Fig. 55 the ratios

$$(\varepsilon^{\mathrm{data}}_{\mathrm{trk}}|_{\rho_{\mathrm{PCA}}<6})/(\varepsilon^{\mathrm{data}}_{\mathrm{trk}}|_{\rho_{\mathrm{PCA}}<8}) \text{ and } (\varepsilon^{\mathrm{data}}_{\mathrm{trk}}|_{\rho_{\mathrm{PCA}}<10})/(\varepsilon^{\mathrm{data}}_{\mathrm{trk}}|_{\rho_{\mathrm{PCA}}<8})$$

and

$$(\varepsilon^{\mathrm{data}}_{\mathrm{trk}}|_{|z_{\mathrm{PCA}}|<10})/(\varepsilon^{\mathrm{data}}_{\mathrm{trk}}|_{|z_{\mathrm{PCA}}|<12}) \text{ and } (\varepsilon^{\mathrm{data}}_{\mathrm{trk}}|_{|z_{\mathrm{PCA}}|<14})/(\varepsilon^{\mathrm{data}}_{\mathrm{trk}}|_{|z_{\mathrm{PCA}}|<12})$$

are reported.
The systematic error is evaluated as the maximum deviation from 1 between each of the two rations on ρ_{FH}, ρ_{PCA} and $|z_{\mathrm{PCA}}|$. The total uncertainty for the tracking efficiency, shown in Fig. 56, is obtained by adding in quadrature the three maximum deviations. The systematic error is about 0.3% in the whole $M^2_{\pi\pi}$ range.

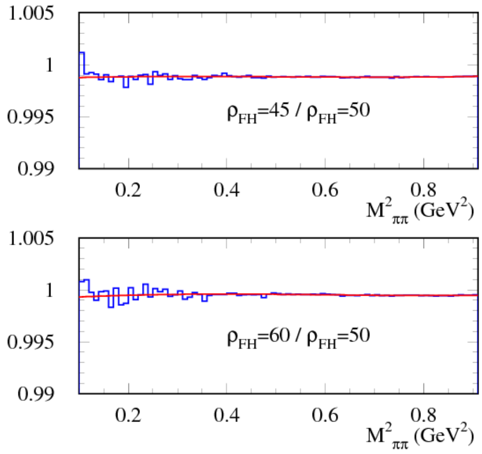

Figure 53: Ratio between the tracking efficiency varying the radial position of the first hit. The red lines represent the polynomial functions used to fit the ratio.

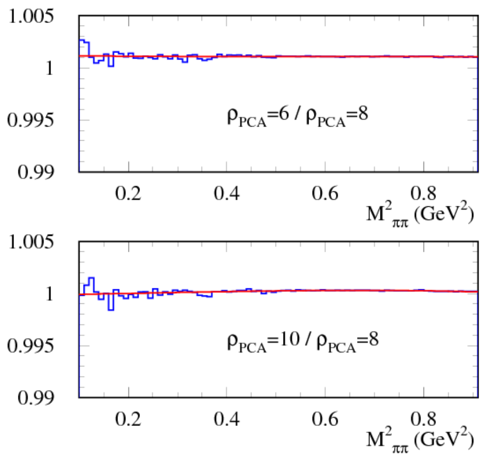

Figure 54: Ratio between the tracking efficiency varying the radial position of the extrapolated point of closest approach of the track to the interaction point. The red lines represent the polynomial functions used to fit the ratio.

4.7.6 Photon efficiency

The calorimeter photon efficiency has been measured using a sample of $\pi^+\pi^-\pi^0$ events, selected from data requiring two opposite charged tracks from the IP, and requiring the missing mass around the mass of π^0. One of the two photons from the neutral pion decay is detected, as a *tagging photon*, and the event is defined efficient if another neutral cluster is found within a cone around the expected direction. The efficiency is evaluated in bins of polar angle of the expected energy. Using the mapping procedure, the result as a function of the pion invariant mass, $\varepsilon_\gamma(M^2_{\pi\pi})$, is obtained. For a detailed explanation of the procedure see [27].
The calorimeter efficiency for photon detection is already included in the effective global efficiency, therefore the relevant quantity is the data-Monte Carlo ratio. The ratio as a function of $M^2_{\pi\pi}$ is shown in Fig. 57. Data and Monte Carlo samples are in

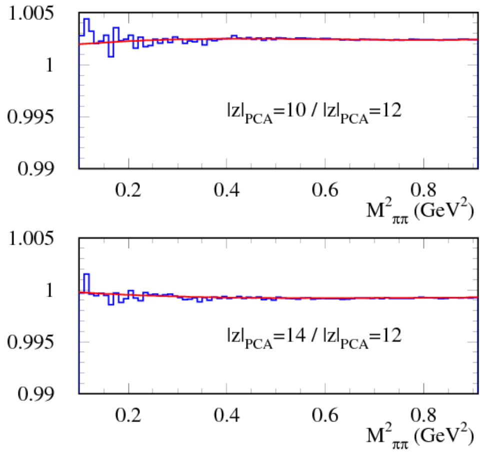

Figure 55: Ratio between the tracking efficiency varying the longitudinal position of the point of closest approach. The red lines represent the polynomial functions used to fit the ratio.

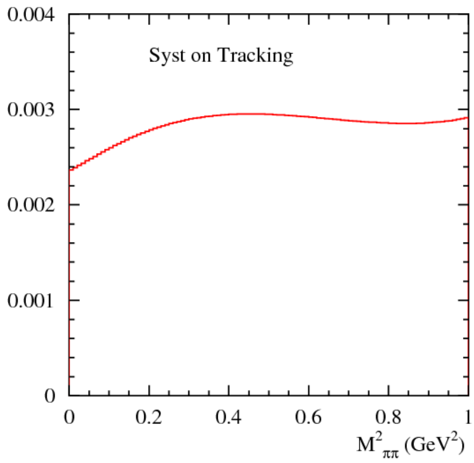

Figure 56: To evaluate the total systematic uncertainty, the three maximum deviation from 1 of the ratios for ρ_{FH}, ρ_{PCA} and $|z_{\mathrm{PCA}}|$ are added in quadrature.

excellent agreement in the energy range considered in the analysis described in this work, indicated by the red line, set at $M^2_{\pi\pi} = 0.85$ GeV^2. Nevertheless, the $\pi^+\pi^-\gamma$ spectrum gets corrcted by $\varepsilon_\gamma^{\mathrm{data}}/\varepsilon_\gamma^{\mathrm{MC}}$ in each bin.

Due to the very high efficiency and the extremely good data-Monte Carlo agreement, we consider the systematic uncertainty on the photon detection efficiency as negligible.

4.7.7 Systematic error on the acceptance efficiency

The geometrical acceptance is taken from Monte Carlo and included in the effective global efficiency approach.

The evaluation of the systematic error introduced by the acceptance cuts is per-

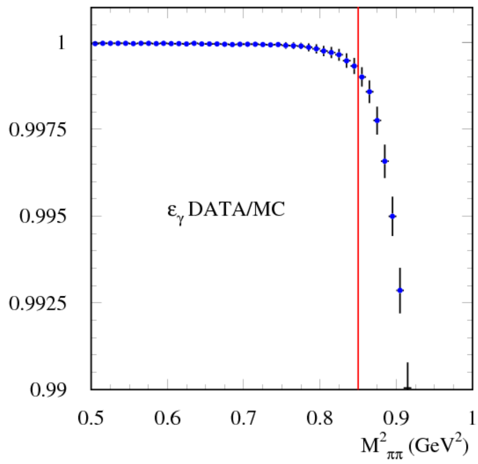

Figure 57: Photon efficiency as a function of $M^2_{\pi\pi}$.

formed again by means of the double ratio approach, see Sec. 4.7.1 and Eq. 19. The double ratio has been performed moving separately the cuts on the pion polar angle and on the photon polar angle.
Varying the pion polar angle one can perform the double ratio

$$R_{\theta_\pi}(M^2_{\pi\pi}) = \frac{(dN^{\rm data}_{\theta_\pi}/dN^{\rm MC}_{\theta_\pi})|_{\theta_\pi \pm 2^\circ}}{(dN^{\rm data}_{\theta_\pi}/dN^{\rm MC}_{\theta_\pi})|_{\theta_\pi}}(M^2_{\pi\pi}), \tag{27}$$

where $\theta_\pi \pm 2^\circ$ stands for the standard cut on θ_π moved by 2°. Concerning the photon polar angle one has

$$R_{\theta_\gamma}(M^2_{\pi\pi}) = \frac{(dN^{\rm data}_{\theta_\gamma}/dN^{\rm MC}_{\theta_\gamma})|_{\theta_\gamma \pm 5^\circ}}{(dN^{\rm data}_{\theta_\gamma}/dN^{\rm MC}_{\theta_\gamma})|_{\theta_\gamma}}(M^2_{\pi\pi}), \tag{28}$$

where again $\theta_\gamma \pm 5^\circ$ is referred to the standard cut on θ_γ moved by 5°.
The quantity of the shifts – i.e. $\pm 2^\circ$ for pions and $\pm 5^\circ$ for photons – have been chosen according to the resolutions on θ_π and θ_γ. These are obtained from the difference between the generated value and the reconstructed one using Monte Carlo $\pi^+\pi^-\gamma$ sample, as shown in Fig. 58.
The resolution on θ_π, shown in Fig. 58(a), has been fitted by three Gaussian distributions, to describe also the tails. The third Gaussian function is required by less than 1% of the events, thus only the first two are taken into account, obtaining a σ of ca. 0.1° and 0.3° respectively, giving a global resolution of ca. 0.5°. The shift applied on θ_π then corresponds to 4σ.
The same evaluation has been performed for θ_γ, see Fig. 58(b), giving an estimated σ of about 1.5°. Thus, shifting the photon polar angle of 5° corresponds to ca. 3 times of the resolution.
Like the systematic uncertainty evaluation for $M_{\rm trk}$ and Ω-angle cuts, the spectra $dN^{\rm data}$ and $dN^{\pi\pi\gamma}$ in bin of 0.01 GeV^2 is $M^2_{\pi\pi}$ are extracted after having applied all the analysis cuts and after having subtracted the background events from $dN^{\rm data}$. Each of the four double ratios – two for $\theta_\pi \pm 2^\circ$ and two for $\theta_\gamma \pm 5^\circ$ – is fitted by a third order polynomial function, to reproduce the behaviour in $M^2_{\pi\pi}$. The maximum

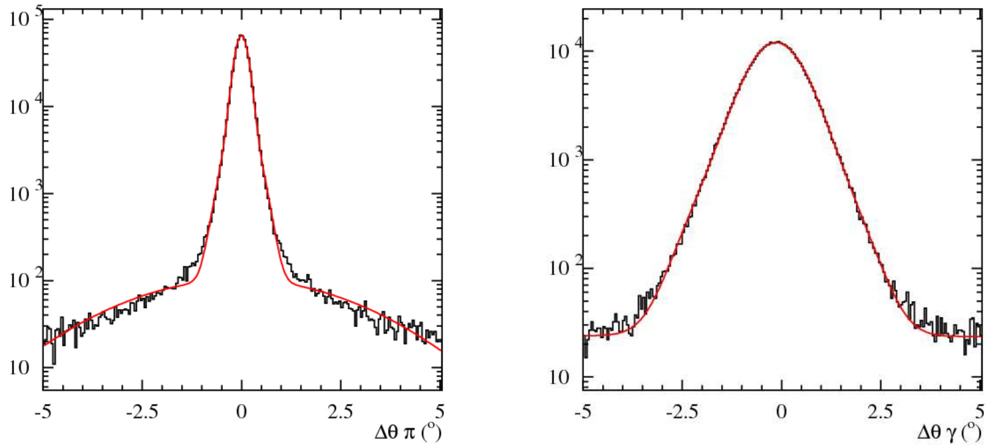

(a) (b)

Figure 58: Resolutions on θ_π, in (a), and θ_γ, in (b).

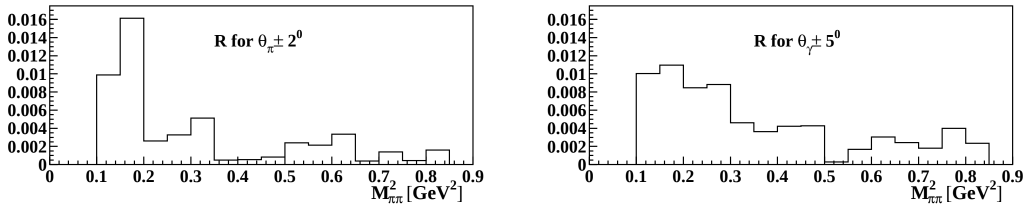

(a) (b)

Figure 59: Maximum deviation from 1 of the two double ratios for the pion polar angle, $R|_{\theta_\pi \pm 2^\circ}$, in (a), and of the two double ratios for the photon polar angle, $R|_{\theta_\gamma \pm 5^\circ}$, in (b).

deviation from 1 for each θ_π and θ_γ cut is taken, see Fig. 59(a) for the pion and Fig. 59(b) for the photon polar angle cuts, respectively.

The systematic error on the acceptance cut is given by squared sum of the the maximum deviations from 1 for $R(M^2_{\pi\pi})|_{\theta_\pi \pm 2^\circ}$ and $R(M^2_{\pi\pi})|_{\theta_\gamma \pm 5^\circ}$, as it is shown in Fig. 60.

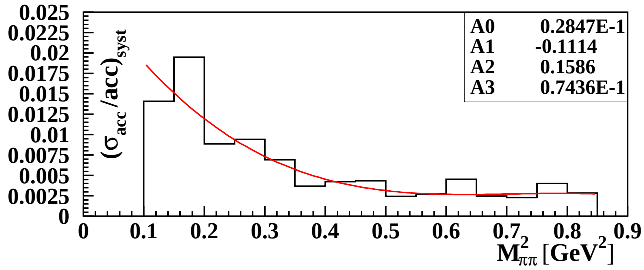

Figure 60: Systematic uncertainty due to the acceptance cut as a function of $M^2_{\pi\pi}$.

4.8 Unshifting Correction for final state radiation events

The transition from $M^2_{\pi\pi}$ to $(M^0_{\pi\pi})^2$ is performed using a special version of the PHOKHARA Monte Carlo generator [28]. This version of the generator allows to distinguish between photons radiated in the initial state from photons emitted in the final state. The presence of final state radiation shifts the observed value of $M^2_{\pi\pi}$ (evaluated from the momenta of the two charged pion tracks in the events) away from the value of the invariant mass squared of the virtual photon produced in the collision. The shift occurs only in one direction, $(M^0_{\pi\pi})^2 \geq M^2_{\pi\pi}$, as can be seen in the spectra reported in Fig. 62. To find out to which bin of $(M^0_{\pi\pi})^2$ an event

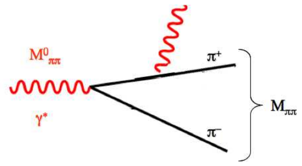

Figure 61: Graphical description of the shifting in the $\pi^+\pi^-$-system invariant mass, from $M^0_{\pi\pi}$ to $M_{\pi\pi}$, due to the photon emission by a pion in the final state.

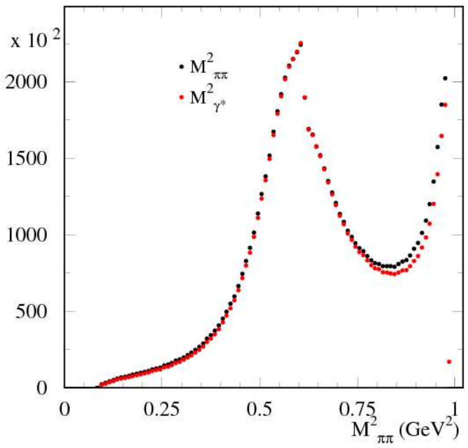

Figure 62: The spectra of $M^2_{\gamma*} \equiv (M^0_{\pi\pi})^2$, in red points, and of $M^2_{\pi\pi}$, in black points.

with a measured value of $M^2_{\pi\pi}$ belongs, a population matrix and a probability matrix, shown in Fig. 63(a) and Fig. 63(b) respectively, have been constructed. The method, based on a matrix multiplication is similar to that one used to evaluate the systematic error of the unfolding procedure (see Sec. 4.6). In this way one can *un-shift* the spectrum performing the passage

$$M^2_{\pi\pi} \rightarrow (M^0_{\pi\pi})^2.$$

In order to be as much as possible inclusive in NLO-FSR events, the energy range considered is broader than that one chosen for the result: the un-shifting is performed in the range $[0. - 1.02]$ GeV^2 instead of $[0.1 - 0.85]$ GeV^2 considered in the measurement.

The spectrum is unshifted after having corrected by acceptance effects (included in the effective global efficiency). Thus the $M^2_{\pi\pi} \rightarrow (M^0_{\pi\pi})^2$ procedure is fully inclusive

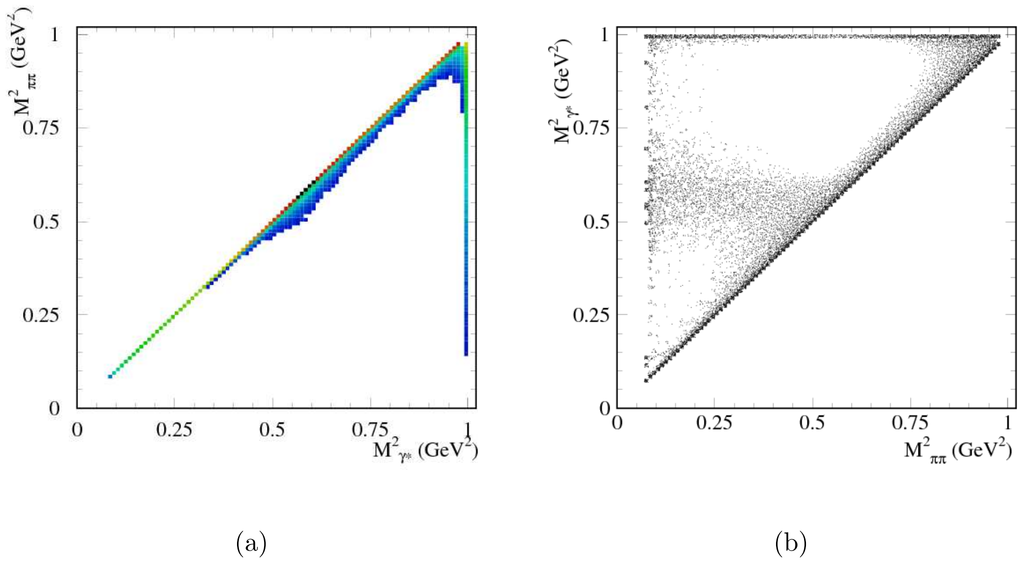

Figure 63: In (a) the population matrix used in the unshifting procedure is shown. In (b) the probability matrix used to unshift the $M^2_{\pi\pi}$ spectrum.

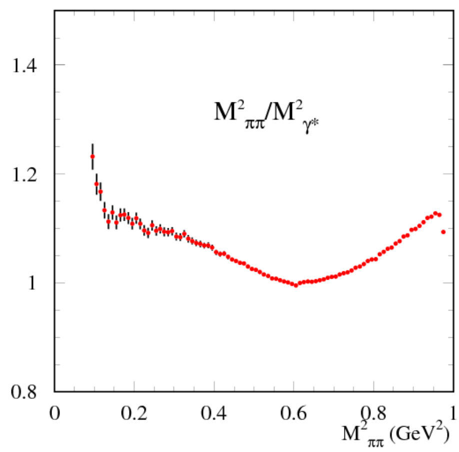

Figure 64: Unshifting correction due to final state radiation on the spectrum (obtained from Monte Carlo).

for the polar angle. The presence of FSR events is of the order of few percent, as can be seen in Fig. 64, where the un-shifting correction is reported by the ratio between $M^2_{\pi\pi}$ and $(M^0_{\pi\pi})^2$. At low values of the pion system invariant mass, the relative increase of final state radiation effects due to events with the emission of two photons, one photon from ISR and the other one from FSR (NLO-FSR), is larger than 15%.

4.9 Luminosity

The absolute normalization of the data sample is obtained [29] from very large angle ($55^\circ < \theta < 125^\circ$) Bhabha, VLAB, events. The integrated luminosity, $\mathcal{L}$, is provided

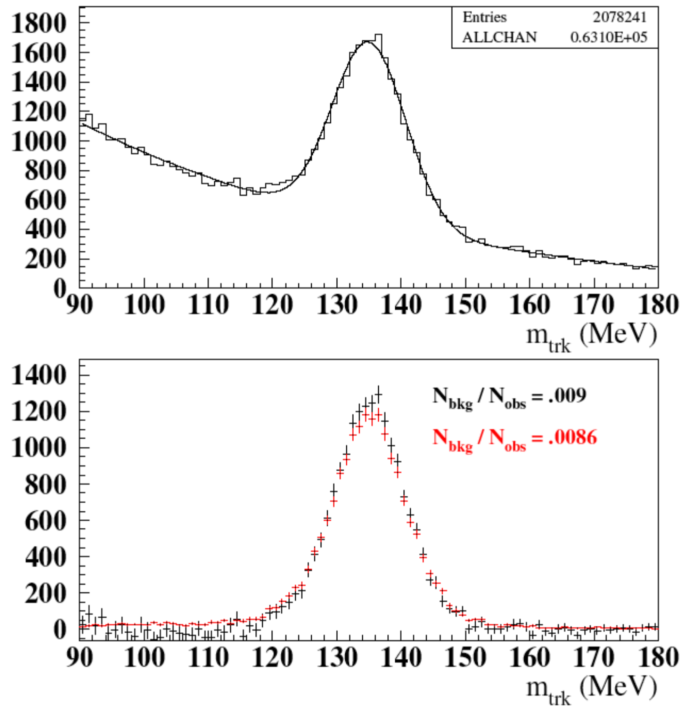

Figure 65: Top: zoom of $M_{\rm trk}$ spectrum from VLAB data fitted with the sum of an exponential plus a Gaussian functions. Down: the same spectrum, after subtracting the exponential, compared with a distribution of events with both tracks identified as pions, from the same data sample.

by:

$$\mathcal{L} = \frac{N_{\rm obs} - N_{\rm bkg}}{\sigma_{\rm eff}} \ , \tag{29}$$

where $N_{\rm obs}$ is the number of candidate large angle Bhabha events, $N_{\rm bkg}$ is the number of background events and $\sigma_{\rm eff}$ is the effective cross section for the KLOE VLAB selection cuts. This cross section is evaluated by the Monte Carlo generator `Babayaga` [30] – including QED radiative corrections with the parton shower algorithm – interfaced with the KLOE detector simulation `GEANFI` [31]. The method for the luminosity determination, the event-selection criteria, and the systematics are all discussed in [29], and we consider here only the updates for the 2006 data analysis.

An updated version of the generator, `Babayaga@NLO` [32], has been released, in which the new predicted cross section decreases by 0.7% ($\sigma_{Bhabha} = 456.2\ nb$) [11] and the theoretical uncertainty improves from 0.5% to 0.1% with respect to the older version.

From the experimental point of view, the hardware veto of cosmic rays, has been removed during 2002 data taking. This implies that this inefficiency is not present in this analysis of VLAB events, and, furthermore, the background process $e^+e^- \to \pi^+\pi^-$ is slightly increased with respect to the analysis of 2001 data, because the veto inefficiency was remarkable for this class of events.

Fig. 65, top, shows the tail of the $M_{\rm trk}$ spectrum of VLAB events in which the signal and background distributions are respectively parameterized with an expo-

[11] For a comparison of the Bhabha cross section with the other generators see [29].

nential and a Gaussian function. Fig. 65, bottom, shows the comparison of the same spectrum after subtracting the exponential with the distribution of events with both tracks fulfilling the pion identification – $\log \mathcal{L}_\pi/\mathcal{L}_e > 0$ – out of the same sample.

Table 3 lists the differences in the contributions to the corrections and systematic errors used for the luminosity measurement, between the analyses of the three data sets.

	2001	2002	2006
relative theoretical error on $\sigma_{\rm eff}$	0.5%	0.1%	0.1%
background correction	−0.6%	−0.7%	−0.9%
cosmic ray veto efficiency	+0.4%	–	–
relative error on $\mathcal{L}$: $\delta_{th} \oplus \delta_{exp}$	0.6%	0.3%	0.3%

Table 3: Differences between 2001, 2002 and 2006 corrections and systematic errors on the luminosity measurement.

More in detail, the background correction is the fraction of events identified as $e^+e^- \to \pi^+\pi^-$ to be subtracted from data and cosmic ray veto efficiency is the fraction of events to be added to the event counts, because of this inefficiency. The relative systematic error on the luminosity measurement is 0.3%.

By chance, the 0.7% change in the sum of the corrections for background and cosmic ray veto efficiency from −0.2% in 2002 to −0.9% in 2006 cancels the 0.7% effect from the updated version of the BABAYAGA generator. Upscaling the effective VLAB cross section of 428.8 nb from the 2002 data analysis [29] by the change of cross section going from $\sqrt{s} = 1.0195$ MeV to $\sqrt{s} = 1000$ MeV (obtained using the new BABAYAGA generator), the new effective VLAB cross section becomes

$$\sigma^{eff}_{VLAB} = 428.8nb \cdot \frac{1.007}{1.007} \cdot \frac{485.1nb}{468.0nb} = 444.5nb \tag{30}$$

With 103379038 selected VLAB candidate events in the 2006 data sample used, one obtains an integrated luminosity of 232.6 pb^{-1}.

4.10 Radiative corrections

As shown in Eq. 41 to obtain the cross section $\sigma(e^+e^- \to \pi^+\pi^-)$, the radiator function, $H(M^2_{\pi\pi}, s)$, has to be taken into account and radiative correction, $\delta_{\rm rad}$, are required.

4.11 The radiator function

The radiative differential cross section $d\sigma(e^+e^- \to \pi^+\pi^- + \gamma_{\rm ISR}(\gamma_{\rm ISR}))(M^2_{\pi\pi}, \theta_\gamma)/ds_{\gamma^*}$ and the total cross section for the process $e^+e^- \to \pi^+\pi^-$, in the absence of photons from final state radiation, are related by a theoretical radiator function, $H(s_{\gamma^*}, s, \theta_\gamma)$, via the equation [7, 34]

$$\frac{d\sigma(e^+e^- \to \pi^+\pi^- + \gamma_{\rm ISR}(\gamma_{\rm ISR}))(M^2_{\pi\pi}, \theta_\gamma)}{dM^2_{\pi\pi}} \cdot s = H(M^2_{\pi\pi}, s, \theta_\gamma) \times \sigma(e^+e^- \to \pi^+\pi^-)(M^2_{\pi\pi}). \tag{31}$$

$M^2_{\pi\pi}$ is the squared invariant mass of the two-pion system, identical to the square of the virtual photon invariant mass in the absence of FSR, s is the squared Center-of-Mass energy of the DAΦNE collider, and θ_γ is the polar angle of the photon.

The dimensionless quantity H describes the emission of soft, virtual and hard photons in the initial state.

Using $\sigma_{\pi\pi}(M^2_{\pi\pi}) = \frac{\pi\alpha^2}{3M^2_{\pi\pi}}\beta^3_\pi|F_\pi(M^2_{\pi\pi})|^2$, it is possible to rewrite Eq. 31 as[12]

$$\frac{d\sigma_{\pi\pi\gamma(\gamma)}(M^2_{\pi\pi},\theta_\gamma)}{dM^2_{\pi\pi}} = \frac{H(M^2_{\pi\pi},s,\theta_\gamma)}{s} \times \frac{\pi\alpha^2}{3M^2_{\pi\pi}}\beta^3_\pi|F_\pi(M^2_{\pi\pi})|^2. \qquad (32)$$

Exploiting Eq. 32 and the `PHOKHARA` Monte Carlo generator, which contains ISR processes up to the next-to-leading order [34], one can obtain the H-function. Setting $|F_\pi(M^2_{\pi\pi})|^2 = 1$ in the generator (and switching off the vacuum polarization of the intermediate photon in the generator), $H(s_{M^2_{\pi\pi}}, s, \theta_\gamma)$ becomes

$$H(M^2_{\pi\pi},s,\theta_\gamma) = s \cdot \frac{3M^2_{\pi\pi}}{\pi\alpha^2\beta^3_\pi} \cdot \frac{d\sigma_{\pi\pi\gamma(\gamma)}(M^2_{\pi\pi},\theta_\gamma)}{dM^2_{\pi\pi}}\Big|^{\mathrm{MC}}_{|F_\pi(M^2_{\pi\pi})|^2=1}. \qquad (33)$$

As can be seen from Eq. 33, the quantity $H(M^2_{\pi\pi},s,\theta_\gamma) \cdot \frac{\pi\alpha^2\beta^3_\pi}{3M^2_{\pi\pi}s}$ takes the dimensions of a differential cross section (nb/GeV^2). Therefore, dividing for this quantity allows to pass from differential to absolute cross sections.

In the analysis H is evaluated for $0° < \theta_\gamma < 180°$, since the spectrum has been already corrected by acceptance cuts. The differential radiator function cross section is shown in Fig. 66.

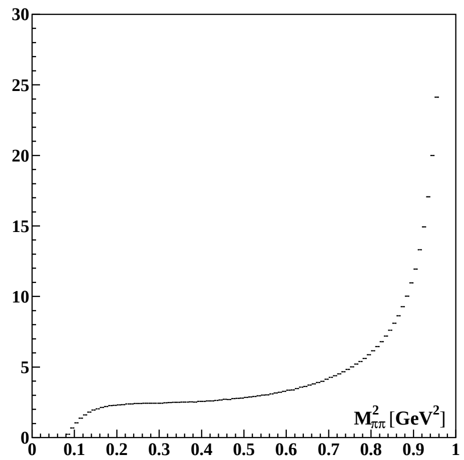

Figure 66: The differential radiator function cross section $H(M^2_{\pi\pi}, s)\cdot\frac{\pi\alpha^2\beta^3_\pi}{3M^2_{\pi\pi}s}$, inclusive in θ_γ, in bins of 0.01 GeV^2 in $M^2_{\pi\pi}$. The value used for s in the Monte Carlo production is $s = 999.85$ (GeV)^2, corresponding to the mean value of DAΦNE energy for data collected in 2006.

[12] $\beta_\pi = \sqrt{1 - \frac{4m^2_\pi}{M^2_{\pi\pi}}}$.

4.11.1 Systematic error of the radiator function

The error quoted by the authors of PHOKHARA on the ISR part of the generator is 0.5%, mainly due to missing diagrams like non-factorizable two-photon exchange contributions.

Possible experimental systematic uncertainty to the radiator function, due to the spread of $\sqrt{s}$ during the 2006 running period of DAΦNE, results to be less than 3×10^{-4} and is flat in the whole energy range. Thus this source of error is considered negligible and only the quoted theoretical 0.5% is taken into account.

4.12 Final state radiation

In this section, the uncertainty on the spectrum from Bremsstrahlung final state radiation is discussed. Other contributions, like final state radiation from ϕ-decays, are discussed in Sec. 4.3.

The presence of events with Bremsstrahlung final state radiation in the data sample affects the analysis

- in the M_{trk} distributions. The missing FSR-NLO terms and the model dependence might affect the data-Monte Carlo agreement in the M_{trk} cut (see Sec. 3.2) and the background fitting procedure (see Sec. 4.2.1). However, thanks to the fine tuning of track parameters, described in [8], the Monte Carlo trackmass distributions reproduce very well the data ones. The systematic uncertainty relative to this cut has already been taken into account;
- in the correction for the angular acceptance cuts for photon detection ($50° < \theta_\gamma < 130°$) and the data quality requests on the momentum of the pion tracks. This correction is included in the *global efficiency* (see eq. 17);
- in the unshifting procedure. The correction due to the passage from $M^2_{\pi\pi}$ to $(M^0_{\pi\pi})^2$ is of the order of several percent, see Fig. 64.

Fig. 67 (a) shows the part of the *global efficiency* which is affected by the presence of final state radiation. It contains the following cuts:

1) $50° < \theta_\gamma < 130°$; $E_\gamma > 20$ MeV
2) $|p_T| > 160$ MeV or $|p_z| > 90$ MeV
   $|\vec{p}| > 200$ MeV
   $0.15 < |p_+| + |p_-| < 1.02$ GeV

Fig. 67 (a) is obtained by creating the ratio

$$\frac{(d\sigma_{\pi^+\pi^-\gamma}\,|\,\mathrm{cuts})/(d(M^2_{\pi\pi})^{\mathrm{ISR+FSR}})}{(d\sigma_{\pi^+\pi^-\gamma}\,|\,\mathrm{full\ inclusive})/(d(M^2_{\pi\pi})^{\mathrm{ISR+FSR}})}. \tag{34}$$

In Fig. 67 (b), the unshifting procedure is approximated using the ratio

$$\frac{(d\sigma_{\pi^+\pi^-\gamma}\,|\,\mathrm{full\ inclusive})/(d(M^2_{\pi\pi})^{\mathrm{ISR+FSR}})}{(d\sigma_{\pi^+\pi^-\gamma}\,|\,\mathrm{full\ inclusive})/(d(M^2_{\pi\pi})^{\mathrm{ISR}})}. \tag{35}$$

The reason for this approximation respect to the more involved method explained in Sec. 4.8 is that not all MC codes allow to compute the cross sections as function of

$(M^0_{\pi\pi})^2$, which is needed in the procedure used in the analysis. Fig. 67 (b) shows that the approximation comes close to the correct procedure, the difference comes from the different treatment of events with NLO-FSR.[13] Fig. 67 (c) shows the combination of both effects. It is obtained from the product of Eq. 34 and Eq. 35:

$$\frac{(d\sigma_{\pi^+\pi^-\gamma}\,|\,\mathrm{cuts})/(d(M^2_{\pi\pi})^{\mathrm{ISR+FSR}})}{(d\sigma_{\pi^+\pi^-\gamma}\,|\,\mathrm{full\ inclusive})/(d(M^2_{\pi\pi})^{\mathrm{ISR+FSR}})} \times \frac{(d\sigma_{\pi^+\pi^-\gamma}\,|\,\mathrm{full\ inclusive})/(d(M^2_{\pi\pi})^{\mathrm{ISR+FSR}})}{(d\sigma_{\pi^+\pi^-\gamma}\,|\,\mathrm{full\ inclusive})/(d(M^2_{\pi\pi})^{\mathrm{ISR}})}$$
$$= \frac{(d\sigma_{\pi^+\pi^-\gamma}\,|\,\mathrm{cuts})/(d(M^2_{\pi\pi})^{\mathrm{ISR+FSR}})}{(d\sigma_{\pi^+\pi^-\gamma}\,|\,\mathrm{full\ inclusive})/(d(M^2_{\pi\pi})^{\mathrm{ISR}})} \qquad (36)$$

It is therefore sufficient to estimate the effect that corrections to FSR have on the ratio given in Eq. 36 and Fig. 67 (c) to obtain an uncertainty related to the FSR treatment, provided that all other parameters in the MC code are identical in nominator and denominator of Eq. 36.

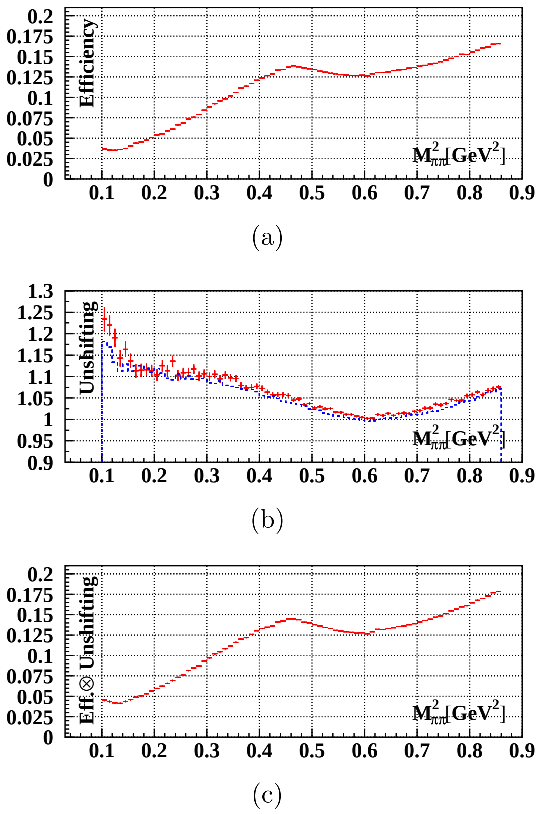

Figure 67: (a) Part of the *global efficiency* affected by FSR. (b) Approximate unshifting (red data points) and unshifting correction used in the analysis (blue histogram), see text. (c) Combination of efficiency and unshifting, see Eq. 36.

4.12.1 Effect from uncertainty on pion form factor at $\sqrt{s} = 1$ GeV

The amount of leading-order Bremsstrahlung final state radiation is proportional to the value of $|F_\pi|^2(s = 1\mathrm{GeV}^2)$, see Ref. [7]. The Monte Carlo samples used to perform the analysis were produced with a parameterization à la Kühn-Santamaria [56], with parameters from an unpublished fit of KLOE data taken in 2001. Using this

[13] The difference in the two methods is that in the procedure used in the analysis, events from NLO-FSR are retained in the spectrum, and moved to a different bin. In the approximation, those events are completely removed.

parameterization, one gets a value of $|F_\pi|^2(s = 1\text{GeV}^2) = 3.30$. We compare this with the parameters based on a fit of data using a Gounaris-Sakurai-approach [57] in [55], which gives a $\sim 5\%$ lower value of $|F_\pi|^2(s = 1\text{GeV}^2) = 3.15$. Table 4 shows the parameters used in the two parameterizations, and Fig. 68 shows both curves as function of $M^2_{\pi\pi}$.[14] The effect these two parameterizations have on the ratio in Eq. 36 is shown in Fig. 69 (a). The difference between the two curves is entirely due to the unshifting (Eq. 35), as is visible in Fig. 69 (b). This can be expected, because the unshifting procedure has a large effect on the leading-order contribution of FSR, which, as discussed above, depends critically on the value of the pion form factor at $\sqrt{s} = 1$ GeV in the present case. An unpublished study with KLOE data indicates a value of $|F_\pi|^2(s = 1\text{GeV}^2) = 3.2 \pm 0.1$, which is compatible with both parameterizations. While the two parameterizations in Table 4 differ by 0.15 in value of $|F_\pi|^2(s = 1\text{GeV}^2)$, the difference between the value used in the KLOE MC and the preliminarily measured value differ by a value of 0.1 (which is also the present uncertainty of the measurement). We therefore take the fractional difference between the two parameterizations in Table 4, shown with red data points in Fig. 69 (c), and scale it with a factor $\frac{2}{3}$ to account for the fact that the parameterization used in the Monte Carlo differs by only 0.1 from the preliminary measured value (blue data points in Fig. 69 (c)). Below 0.35 GeV^2, a straight line fit gives a value of 1.3%, whereas above a polynomial function is fitted to approximate the data points as a function of $x = M^2_{\pi\pi}$:

$$\Delta\sigma_{\pi\pi}(x) = |-0.46831 + 4.4100x - 15.170x^2 + 24.329x^3 - 18.389x^4 + 5.2909x^5|$$

We take the absolute value of this polynomial curve to obtain an uncertainty which is always positive - since the two parameterizations discussed differ not only in the value for $|F_\pi|^2(s = 1\text{GeV}^2)$, but also slightly in their shape, the difference between the two curves shown in Fig. 69 (c) takes on slightly negative values at the peak around the ρ-meson mass.

In Fig. 74 and Table 6, the parameterization for the uncertainty on the measurement from the uncertainty on the FSR treatment coming from the influence of the missing knowledge of the pion form factor value at $\sqrt{s} = 1$ GeV is given. The effect on the $\Delta a_\mu^{\pi\pi}$ evaluation between 0.1 and 0.85 GeV^2 is 0.5%.

4.12.2 An estimate of the model-dependence of FSR using SU(3) χPT

Apart from the dependence of the FSR corrections from the value of the pion form factor at $\sqrt{s} = 1$ GeV^2, a possible deviation of final state radiation from the point-like pion model needs to be taken into account. The model of point-like pions is actually used in the Monte-Carlo generator PHOKHARA and is commonly used by most experiments. Given the fact that FSR corrections are large in the analysis presented here, possible effects beyond the point-like pion model need to be studied. It is important to understand that one part of such beyond-point-like-pion effects has already been taken into account, namely the so-called additional background, stemming from the $f_0(980)\gamma$ or $\rho\gamma$ intermediate states (see Chapter 4.3). In this chapter we describe effects, which might go beyond effects of these kind. We use Chiral Perturbation Theory (χPT) to estimate the size of additional effects. We also

[14] More information on the Kühn-Santamaria and Gounaris-Sakurai approaches can be found in the appendix of this document.

	KS (KLOE MC)	GS ([55])
m_ρ [MeV]	772.6	773.95
Γ_ρ [MeV]	143.7	144.9
m_ω [MeV]	782.78	783.0
Γ_ω [MeV]	8.68	8.4
c_0	1.17275	1.171
c_1	-0.17275	-0.1194
c_ω	0.00148	0.00184
$m_{\rho'}$ [MeV]	1460	1356.71
$\Gamma_{\rho'}$ [MeV]	310	436.85
$m_{\rho''}$ [MeV]	1700	1700
$\Gamma_{\rho''}$ [MeV]	240	240
$m_{\rho'''}$ [MeV]	$775.5 * \sqrt{7.0}$	$775.5 * \sqrt{7.0}$
$\Gamma_{\rho'''}$ [MeV]	$0.2 \cdot m_{\rho'''}$	$0.2 \cdot m_{\rho'''}$
c_2	0.0	0.011519
c_3	0.0	-0.0437612
c_n	0.0	-0.0193578

Table 4: Parameters for the pion form factor parameterizations used to estimate the effect on the uncertainty from FSR.

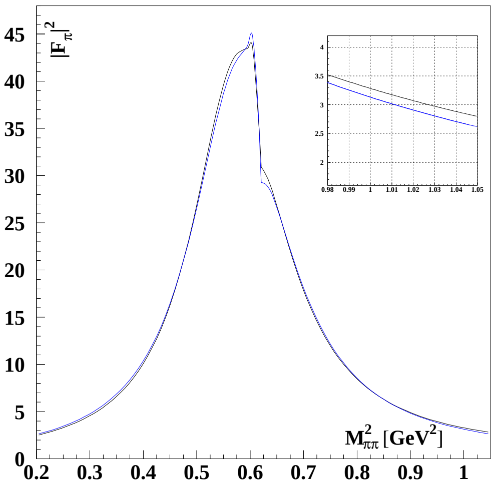

Figure 68: Two parameterizations of the pion form factor to estimate the effect on the FSR uncertainty. Blue curve: Gounaris-Sakurai-parameterization from [55]. Black curve: Kühn-Santamaria parameterization from KLOE data (2001), unpublished.

investigated the possibility to use the Resonance Chiral Theory (RχT) [40]; this would however require the knowledge of the relevant coupling parameters, which is not existing.
Fig. 70 shows the fractional difference between two PHOKHARA Monte-Carlo productions in which in the one case the point-like pion model ("General Born", GB) and in the second case the χPT calculation is used. For the χPT computation the

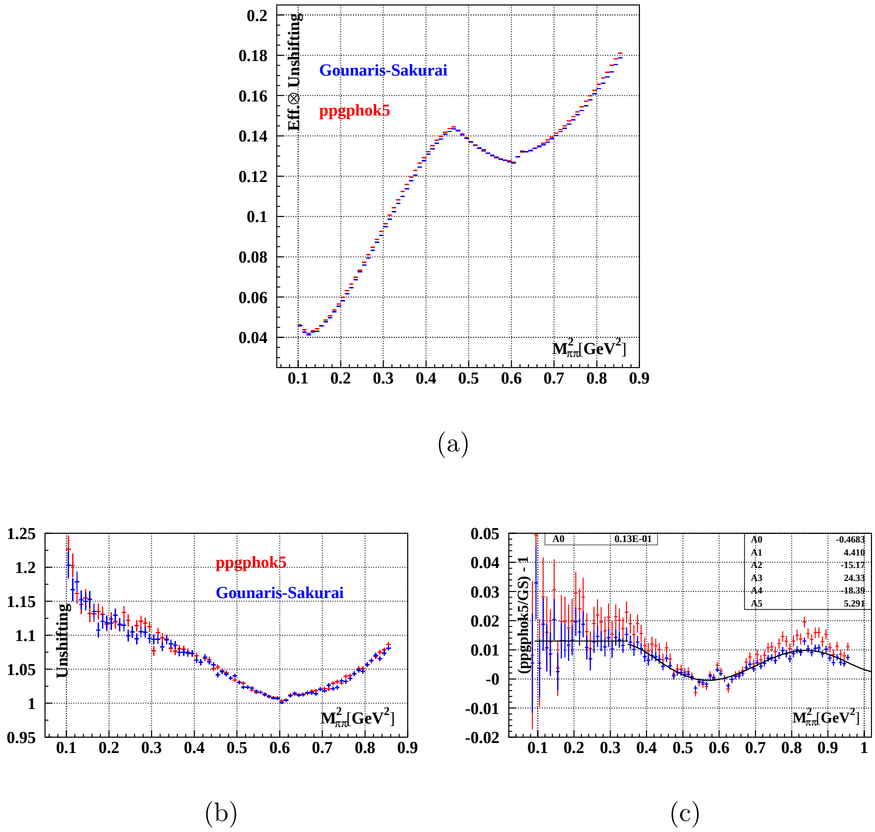

Figure 69: (a) Effect of two parameterizations for the pion form factor on the ratio of Eq. 36. Red data points: "ppgphok5" parameterization used in KLOE MC productions based on fit to KLOE 2001 data, blue data points: GS parameterization from [55]. (b) Effect of the two parameterizations on the unshifting (Eq. 35). (c) Red data points: Fractional difference between the two curves shown in (a), blue data points show the result from the red points scaled by a factor $\frac{2}{3}$, see text.

work published in [42, 43] is used. A similar comparison as the one presented here is described in detail in Ref. [41]. We observe deviations of up to 7% at threshold, while in the intermediate and the high mass region no sizeable deviation from the point-like pion model can be seen. As an estimate we take the full difference as the model uncertainty for the point-like pion model used in our analysis. We want to stress that the low-energy constants used in the χPT calculations might include up to some extent the resonant substructures of Chapter 4.3 and therefore our uncertainty estimate has to be considered as a very conservative approach, which leads to an uncertainty on the $\Delta a_\mu^{\pi\pi}$ evaluation between 0.1 and 0.85 GeV^2 of 0.6%.

4.13 Vacuum polarisation

In order to obtain the *bare* cross section, needed to evaluate $a_\mu^{\pi\pi}$ vacuum polarization effects must be subtracted. This is done by correcting the cross section for the running of $\alpha_{\rm em}$ as follows:

$$\sigma^{bare} = \sigma^{dressed}\left(\frac{\alpha_{\rm em}(0)}{\alpha_{\rm em}(s=M^2_{\pi\pi})}\right)^2 \equiv \sigma^{dressed}/\delta(s=M^2_{\pi\pi}). \tag{37}$$

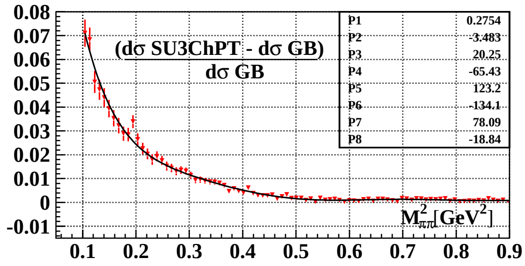

Figure 70: Fractional difference between Monte-Carlo productions in which the model of point-like pions is used as a model for FSR, compared to a χPT calculation. The full difference is used for the model dependence of the point-like pion model.

where the running of $\alpha_{\rm em}$ can be written as [35]:

$$\alpha_{\rm em}(s) = \frac{\alpha_{\rm em}(0)}{1 - \Delta\alpha_{\rm em}^{lep}(s) - \Delta\alpha_{\rm em}^{\rm had}(s)} \tag{38}$$

The leptonic contribution can be calculated analytically, while the hadronic contribution comes from a dispersion integral, which includes the hadronic cross section itself in the integrand:[15]

$$\Delta\alpha_{\rm em}^{\rm had}(s) = -\frac{\alpha_{\rm em}(0)s}{3\pi} Re \int_{4m_\pi^2}^{\infty} ds' \frac{R(s')}{s'(s'-s-i\epsilon)}. \tag{39}$$

Therefore, the correct procedure has to be iterative and it should include the same data that must be corrected. However, since the correction is at the few percent level, the $\Delta\alpha_{\rm had}(s)$ is evaluated using $\sigma_{\rm had}(s)$ values previously measured [36].

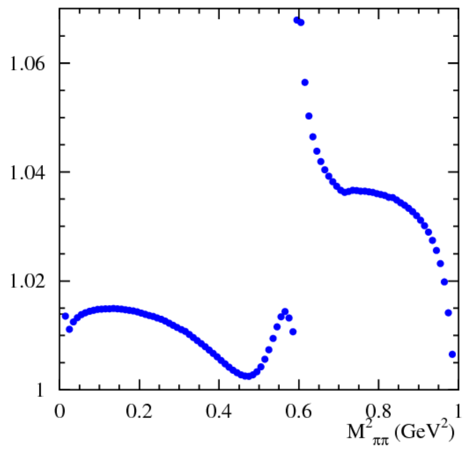

Figure 71: Correction factor $\delta_{\rm VP}(s)$: $\sigma^{bare}(s) = \sigma^{dressed}(s)/\delta_{\rm VP}(s)$, obtained from [36].

Fig. 71 shows the correction $\delta_{\rm VP}(s)$ applied to the $\pi^+\pi^-$ cross section. This correction avoids double-counting of higher order terms in the dispersion integral for $a_\mu^{\pi\pi}$, and it is not applied to the pion form factor $|F_\pi(s)|^2$.

[15] $R(s) \equiv \sigma_{bare}^{had}(s)/\frac{4\pi\alpha(0)^2}{3s}$

5 Results

5.1 Results of the KLOE10 analysis

The differential $\pi^+\pi^-\gamma$ cross section is obtained from the formula:

$$\frac{d\sigma_{\pi\pi\gamma}}{dM^2_{\pi\pi}} = \frac{\Delta N_{\rm obs} - \Delta N_{\rm bkg}}{\Delta M^2_{\pi\pi}} \frac{1}{\varepsilon_{\rm dat} \cdot \varepsilon_{\rm glob,cond} \cdot c_\varepsilon \int \mathcal{L}\, dt} \tag{40}$$

The cross section can be extracted from radiative events by means of the relation

$$\frac{\sigma_{\pi\pi}}{s} = \frac{\Delta N_{\rm obs} - \Delta N_{\rm bkg}}{\Delta (M^0_{\pi\pi})^2} \cdot \frac{1}{\varepsilon_{\rm dat} \cdot \varepsilon_{\rm glob} \cdot c_\varepsilon} \cdot \frac{1}{\int \mathcal{L}\, dt} \cdot \frac{1}{H(M^2_{\pi\pi}, s)}. \tag{41}$$

In Eq. 40 and 41, $\Delta N_{\rm obs} - \Delta N_{\rm bkg}$ represents the observed spectrum after the residual background subtraction, binned in the hadronic system invariant mass, $\Delta M^2_{\pi\pi}$, equal to 0.01 GeV^2; $\varepsilon_{\rm dat}$ represents the correction for the efficiencies evaluated directly from data control samples; $\varepsilon_{\rm glob,cond}$ and $\varepsilon_{\rm glob}$ indicate the effective global efficiency taken from Monte Carlo (in the case of the differential cross section, this efficiency is conditioned to the presence of at least one photon with $50° < \theta_\gamma < 130°$ and $E_\gamma > 20$ MeV); the c_ε are corrections for data-Monte Carlo differences in the individual efficiencies; $\int \mathcal{L}\, dt$ is the integrated luminosity of the 2006 data sample, corresponding to 232.6 pb^{-1} and $H(M^2_{\pi\pi}, s)$ is the radiator function.

To obtain the bare cross section, $\sigma^{\rm bare}_{\pi\pi}$, we need to correct the cross section for effects from vacuum polarisation in the virtual photon produced in the e^+e^- annihilation, and correct the cross section via

$$\sigma^{\rm bare}_{\pi\pi}((M^0_{\pi\pi})^2) = \sigma_{\pi\pi}((M^0_{\pi\pi})^2) \times \left(\frac{\alpha}{\alpha((M^0_{\pi\pi})^2)}\right)^2 \tag{42}$$

α is the fine structrue constant in the limit $q = 0$ ($\alpha = e^2/4\pi$), and $\alpha((M^0_{\pi\pi})^2)$ represents its effective value at the specific value of $(M^0_{\pi\pi})^2$. We use the parameterization for $\alpha/\alpha((M^0_{\pi\pi})^2)$ provided in [36].

The squared modulus of the pion form factor $|F_\pi|^2$ can then be derived using the relation

$$|F_\pi(s')|^2(1 + \eta_{\rm FSR}(s')) = \frac{3}{\pi}\frac{s'}{\alpha^2\beta^3_\pi}\sigma_{\pi\pi}(s') \tag{43}$$

where $s' = (M^0_{\pi\pi})^2$ is the squared momentum transferred by the virtual photon and $\beta_\pi = \sqrt{1 - \frac{4m^2_\pi}{s'}}$ is the pion velocity. The factor $(1 + \eta_{\rm FSR}(s'))$ describes the effect of FSR assuming pointlike pions (for the $\eta_{\rm FSR}(s')$ term, see [39, 44]). In this way, for the choice of radiative corrections applied to $\sigma^{\rm bare}_{\pi\pi}$ and $|F_\pi|^2$, we adopt the definition used also in [46, 47, 48], in which $\sigma^{\rm bare}_{\pi\pi}$ is inclusive with respect to final state radiation, and undressed from vacuum polarisation effects; while $|F_\pi|^2$ contains vacuum polarisation effects and final state radiation is removed.

Our results are summarized in Table 5 which gives

- the observed differential cross section $d\sigma(e^+e^- \to \pi^+\pi^-\gamma)/dM^2_{\pi\pi}$ as a function of the measured invariant mass of the dipion system, $M^2_{\pi\pi}$, with $0° < \theta_\pi < 180°$ and at least one photon in the angular region $50° < \theta_\gamma < 130°$ with $E_\gamma > 20$ MeV, with statistical and systematic error;

- the *bare* cross section $\sigma^{\rm bare}(e^+e^- \to \pi^+\pi^-)$, inclusive of FSR, but with vacuum polarization effects removed, as a function of $(M^0_{\pi\pi})^2$, with statistical error;

- the pion form factor, dressed with vacuum polarization, but with FSR effects excluded, as a function of $(M^0_{\pi\pi})^2$, with statistical error.

The statistical errors given in Table 5 are weakly correlated as a result of the resolution unfolding. The corresponding covariance matrices are given in [37]. The systematic errors are obtained combining all the individual contributions in each column in Table 7 in quadrature for each value of $M^2_{\pi\pi}$. Where the contributions are not constant in $M^2_{\pi\pi}$, polynomial parameterizations as a function of $M^2_{\pi\pi}$ are given in Table 6.

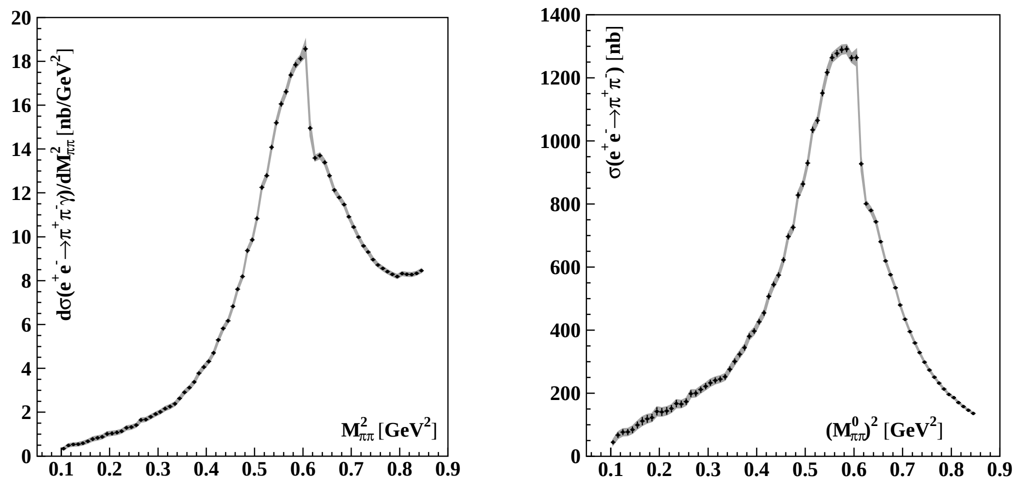

Figure 72: Left: differential cross section for the $e^+e^- \to \pi^+\pi^-\gamma(\gamma)$ process, inclusive in θ_π and with at least one photon having $E_\gamma > 20$ MeV and $50^o < \theta_\gamma < 130^o$. Right: *bare* cross section for $e^+e^- \to \pi^+\pi^-$. The data points have statistical error attached, the grey band gives the statistical and systematic uncertainty (added in quadrature).

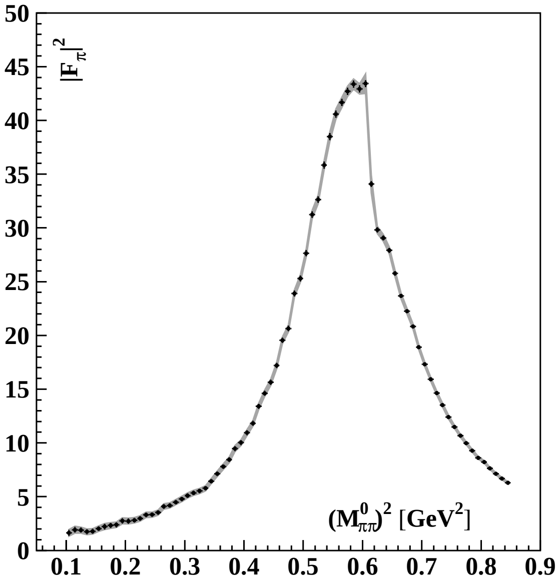

Figure 73: The pion form factor $|F_\pi|^2$. The error bars assigned to the points represent the statistical error, while the shaded band represents the combination of statistical and systematic uncertainty, added in quadrature, at each value of $(M^0_{\pi\pi})^2$, the invariant mass of the dipion system after the correction for the unshifting.

$M^2_{\pi\pi}$|$(M^0_{\pi\pi})^2$ GeV^2	$\sigma_{\pi\pi\gamma}$ nb/GeV^2	$\sigma^{bare}_{\pi\pi}$ nb	$\|F(\pi)\|^2$	$M^2_{\pi\pi}$|$(M^0_{\pi\pi})^2$ GeV^2	$\sigma_{\pi\pi\gamma}$ nb/GeV^2	$\sigma^{bare}_{\pi\pi}$ nb	$\|F(\pi)\|^2$	$M^2_{\pi\pi}$|$(M^0_{\pi\pi})^2$ GeV^2	$\sigma_{\pi\pi\gamma}$ nb/GeV^2	$\sigma^{bare}_{\pi\pi}$ nb	$\|F(\pi)\|^2$
0.105	0.34±0.06±0.03	44±7	1.63±0.27	0.355	2.91±0.09±0.03	301±9	7.13±0.22	0.605	18.57±0.12±0.35	1264±10	43.42±0.33
0.115	0.49±0.06±0.03	67±9	1.92±0.26	0.365	3.12±0.09±0.04	323±9	7.79±0.22	0.615	14.95±0.11±0.34	927±7	34.09±0.27
0.125	0.53±0.07±0.03	76±9	1.89±0.24	0.375	3.38±0.09±0.03	344±9	8.43±0.22	0.625	13.59±0.10±0.08	801±7	29.81±0.25
0.135	0.54±0.07±0.03	77±10	1.74±0.23	0.385	3.78±0.09±0.04	381±9	9.47±0.23	0.635	13.70±0.10±0.08	779±6	29.08±0.24
0.145	0.59±0.08±0.04	84±11	1.78±0.23	0.395	4.06±0.09±0.04	397±9	10.02±0.23	0.645	13.38±0.10±0.08	743±6	27.91±0.23
0.155	0.67±0.08±0.04	99±11	2.02±0.23	0.405	4.32±0.09±0.04	426±9	10.94±0.23	0.655	12.79±0.10±0.07	680±6	25.77±0.21
0.165	0.78±0.09±0.03	111±13	2.21±0.26	0.415	4.70±0.09±0.04	454±9	11.83±0.23	0.665	12.13±0.09±0.07	619±5	23.68±0.20
0.175	0.83±0.09±0.03	119±12	2.32±0.24	0.425	5.29±0.09±0.04	507±9	13.40±0.24	0.675	11.79±0.09±0.07	576±5	22.25±0.19
0.185	0.88±0.08±0.03	122±12	2.38±0.23	0.435	5.82±0.09±0.05	545±9	14.62±0.24	0.685	11.47±0.09±0.07	534±5	20.84±0.18
0.195	1.01±0.09±0.03	142±13	2.75±0.26	0.445	6.17±0.09±0.04	574±9	15.64±0.24	0.695	10.91±0.09±0.07	479±4	18.91±0.16
0.205	1.04±0.09±0.03	140±13	2.72±0.24	0.455	6.83±0.09±0.05	622±9	17.21±0.25	0.705	10.45±0.08±0.06	434±4	17.32±0.15
0.215	1.07±0.09±0.03	144±12	2.81±0.23	0.465	7.61±0.10±0.05	697±9	19.55±0.26	0.715	9.98±0.08±0.06	394.9±3.4	15.92±0.14
0.225	1.14±0.09±0.03	151±11	2.97±0.22	0.475	8.19±0.10±0.05	725±9	20.64±0.26	0.725	9.58±0.08±0.06	359.4±3.2	14.64±0.13
0.235	1.29±0.09±0.03	167±12	3.31±0.23	0.485	9.37±0.10±0.06	828±10	23.90±0.28	0.735	9.30±0.08±0.06	328.5±3.0	13.53±0.12
0.245	1.32±0.09±0.03	165±11	3.32±0.22	0.495	9.86±0.10±0.06	863±10	25.30±0.28	0.745	8.96±0.08±0.06	298.2±2.7	12.42±0.11
0.255	1.41±0.08±0.03	173±10	3.52±0.21	0.505	10.84±0.11±0.07	930±10	27.65±0.29	0.755	8.71±0.07±0.05	272.9±2.4	11.49±0.10
0.265	1.64±0.09±0.03	198±11	4.10±0.22	0.515	12.25±0.11±0.08	1035±10	31.24±0.31	0.765	8.55±0.07±0.05	250.6±2.2	10.67±0.09
0.275	1.67±0.08±0.03	199±10	4.18±0.21	0.525	12.79±0.11±0.08	1065±10	32.64±0.31	0.775	8.42±0.07±0.05	231.8±2.1	9.97±0.09
0.285	1.79±0.08±0.03	211±10	4.49±0.21	0.535	14.08±0.12±0.09	1151±10	35.84±0.33	0.785	8.29±0.07±0.05	213.2±1.9	9.27±0.08
0.295	1.92±0.08±0.03	222±10	4.78±0.21	0.545	15.20±0.12±0.09	1217±11	38.49±0.34	0.795	8.19±0.07±0.05	196.1±1.8	8.62±0.08
0.305	2.02±0.09±0.03	233±10	5.10±0.21	0.555	16.06±0.12±0.09	1264±11	40.59±0.34	0.805	8.32±0.07±0.05	185.2±1.6	8.23±0.07
0.315	2.17±0.09±0.03	241±9	5.36±0.21	0.565	16.62±0.12±0.10	1278±10	41.68±0.34	0.815	8.29±0.07±0.05	170.2±1.5	7.64±0.07
0.325	2.26±0.09±0.03	244±9	5.53±0.21	0.575	17.38±0.12±0.10	1289±10	42.71±0.34	0.825	8.28±0.07±0.05	157.4±1.4	7.13±0.06
0.335	2.38±0.09±0.03	252±9	5.79±0.21	0.585	17.85±0.12±0.10	1291±10	43.38±0.34	0.835	8.34±0.07±0.05	146.1±1.2	6.69±0.06
0.345	2.63±0.09±0.04	276±9	6.44±0.21	0.595	18.13±0.12±0.10	1263±10	42.94±0.33	0.845	8.45±0.07±0.05	135.9±1.1	6.28±0.05

Table 5: $\sigma_{\pi\pi\gamma}$, $\sigma^{bare}_{\pi\pi}$ cross sections and pion form factor $|F_\pi|^2$ for bins of 0.01 GeV^2, where the value given indicates the bin center. While the $\sigma_{\pi\pi\gamma}$ cross section is given as a function of $M^2_{\pi\pi}$, the $\sigma^{bare}_{\pi\pi}$ cross section and $|F^2_\pi|$ are given as function of $(M^0_{\pi\pi})^2$. The error attached to each value represents the statistical uncertainty. For $\sigma_{\pi\pi\gamma}$, the second error gives the systematic uncertainty obtained by adding all the contributions in the first column of Table 7 quadratically for each value of $M^2_{\pi\pi}$.

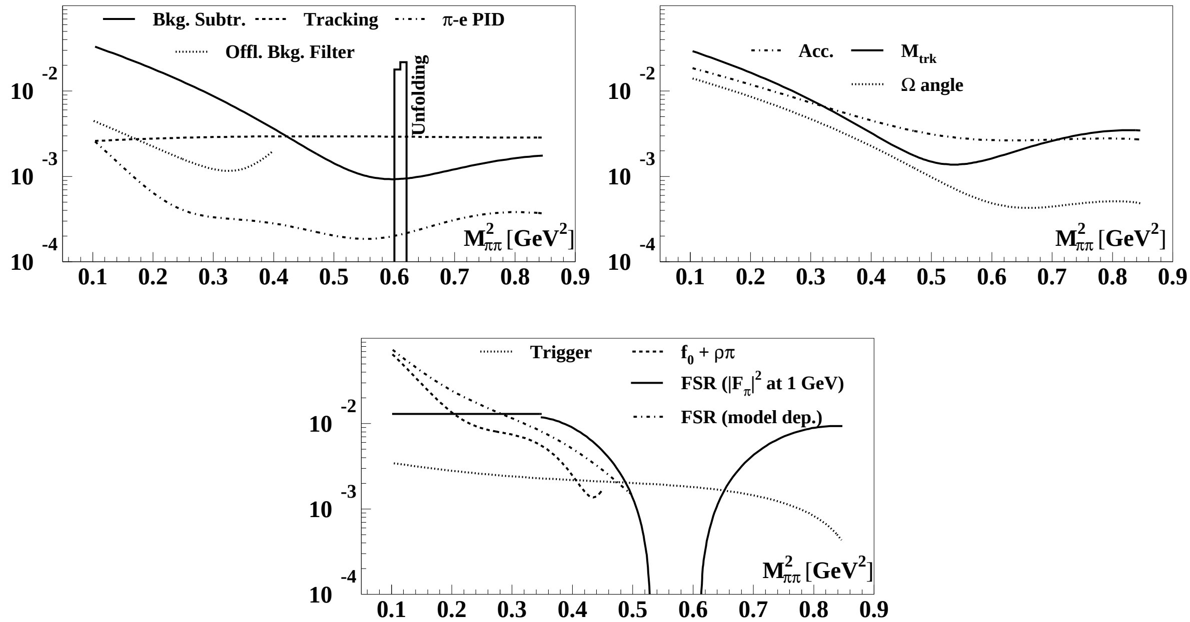

Figure 74: Parameterized fractional uncertainties as function of $M^2_{\pi\pi}$. The parameterizations are given in Table 6.

Our results are summarized in Table 5, which lists:

- the differential cross section $d\sigma(e^+e^- \to \pi^+\pi^-\gamma)/dM^2_{\pi\pi}$ as a function of the invariant mass of the di-pion system, $M^2_{\pi\pi}$, with $0° < \theta_\pi < 180°$ and at least one photon in the angular region $50° < \theta_\gamma < 130°$ with $E_\gamma > 20$ MeV;

- the *bare* cross section $\sigma(e^+e^- \to \pi^+\pi^-)$, inclusive of FSR, but with the vacuum polarization effects removed 4.13, as a function of $(M^0_{\pi\pi})^2$;

- the pion form factor dressed with vacuum polarization, but with FSR effects excluded, as a function of $(M^0_{\pi\pi})^2$ (equal to $M^2_{\pi\pi}$ in the absence of FSR).

Fig. 72, left, shows the observed differential cross section for $e^+e^- \to \pi^+\pi^-\gamma$, while Fig. 72, right, shows the cross section $\sigma^{\text{bare}}_{\pi\pi}$. The latter is the input for the dispersion integral for $\Delta a^{\pi\pi}_\mu$:

$$\Delta a^{\pi\pi}_\mu = \frac{1}{4\pi^3} \int_{s_{min}}^{s_{max}} \mathrm{d}s \, \sigma^{\text{bare}}_{\pi\pi}(s) \, K(s), \tag{44}$$

which gets computed as the sum of the values for $\sigma^{\text{bare}}_{\pi\pi}$ listed in Table 5 times the bin width of 0.01 GeV^2 used in the analysis times a kernel function $K(s)$ which behaves approximately like $1/s$ [49, 50], enhancing the contributions at low values of s. The lower and upper bounds of the integral are $s_{min} = 0.10$ GeV^2 and $s_{max} = 0.85$ GeV^2 in the analysis, and the statistical errors of the $\sigma^{\text{bare}}_{\pi\pi}$ values are summed in quadrature to obtain the statistical error of $\Delta a^{\pi\pi}_\mu$. For each individual contribution listed in Table 7, the systematic uncertainties on the $\sigma^{\text{bare}}_{\pi\pi}$ values are added linearly in the summation to obtain the contribution to the systematic error of $\Delta a^{\pi\pi}_\mu$. Then the individual contributions are added in quadrature to get the total experimental and theory systematics.

Reconstruction Filter	$0.00767 - 0.0269x - 0.1378x^2 + 1.215x^3 - 3.346x^4 + 3.423x^5$ for $x < 0.4$ GeV^2
Background subtr.	$0.0576 - 0.2862x + 0.5231x^2 - 0.4088x^3 + 0.1160x^4$
Trigger	$0.004511 - 0.01264x + 0.02405x^2 - 0.0175x^3$
π-e ID	$0.010423 - 0.12737x + 0.65034x^2 - 1.7069x^3$ $+2.4118x^4 - 1.7383x^5 + 0.50088x^6$
Unfolding	$0.60 < M^2_{\pi\pi} < 0.61$ GeV^2: 0.018 $0.61 < M^2_{\pi\pi} < 0.62$ GeV^2: 0.022
$f_0 + \rho\pi$ corr.	$0.2701 - 3.2686x + 15.263x^2 - 31.418x^3 + 23.769x^4$ for $x < 0.45$ GeV^2
Tracking eff.	$0.002336 + 0.002988x - 0.003995x^2 + 0.0003186x^3$ $+0.001276x^4$
Ω angle eff.	$0.0222 - 0.09079x + 0.1252x^2 - 0.0570x^3$
Trackmass eff.	$0.04944 - 0.2282x + 0.3500x^2 - 0.1708x^3$
Acceptance	$0.02847 - 0.1114x + 0.1586x^2 - 0.07436x^3$
FSR treatment (model dep.)	$0.27535 - 3.4831x + 20.254x^2 - 65.428x^3$ $+123.18x^4 - 134.05x^5 + 78.091x^6 - 18.844x^7$ for $x < 0.5$ GeV^2
FSR treatment ($\|F_\pi(1\text{GeV})\|^2$)	0.0130 for $x < 0.35$ GeV^2; $\|-0.46831 + 4.4100x - 15.170x^2 + 24.329x^3$ $-18.389x^4 + 5.2909x^5\|$ for $x > 0.35$ GeV^2

Table 6: Parameterizations of fractional systematic errors as a function of $0.1 < x \equiv M^2_{\pi\pi} < 0.85$ GeV^2.

	$\sigma_{\pi\pi\gamma}$	$\sigma_{\pi\pi}^{\text{bare}}$	$\lvert F_\pi\rvert^2$	$\Delta a_\mu^{\pi\pi}$
Reconstruction Filter				negligible
Background subtraction				0.5%
$f_0 + \rho\pi$ bkg.				0.4%
Ω cut				0.2%
Trackmass cut	see Tab. 6			0.5%
π-e ID	and Fig. 74			negligible
Tracking				0.3%
Trigger				0.2%
Acceptance				0.5%
Unfolding				negligible
Software Trigger (L3)	0.1%			
Luminosity	0.3%			
Experimental systematics				1.0%
FSR treatment ($\lvert F_\pi(1\text{GeV})\rvert^2$)	-	Tab. 6		0.5%
(model dep.)	-	and Fig. 74		0.6%
Radiator function H	-	0.5%		
Vacuum Polarization	-	see Ref. [36]	-	0.1%
Theory systematics				0.9%

Table 7: Systematic errors on $\sigma_{\pi\pi\gamma}$, $\sigma_{\pi\pi}^{\text{bare}}$, $|F_\pi|^2$ and $\Delta a_\mu^{\pi\pi}$.

As a result, we obtain a value of

$$\Delta a_\mu^{\pi\pi}(0.1 - 0.85\ \text{GeV}^2) = (478.5 \pm 2.0_{\text{stat}} \pm 5.0_{\text{exp}} \pm 4.5_{\text{theo}}) \cdot 10^{-10} \tag{45}$$

The combined fractional systematic error of our value for $\Delta a_\mu^{\pi\pi}$ is 1.4%.

6 Comparison with previous KLOE results

In the range of $0.35 < (M_{\pi\pi}^0)^2 < 0.85\ \text{GeV}^2$ we can compare our new results for the pion form factor with the result of the previous KLOE analysis [6]. The comparison is shown in Fig. 75. Despite the fact that the datasets have been collected at different running conditions of the DAΦNE collider, and using different selection cuts in acceptance, a remarkable agreement is found above 0.5 GeV^2, while below the new result is lower by few percent. This is reflected also in the evaluation of the dispersion integral for $\Delta a_\mu^{\pi\pi}$ in Eq. 44 between 0.35 and 0.85 GeV^2, where the new results gives a value of $\Delta a_\mu^{\pi\pi}$ which is lower by (0.8 ± 0.9)%:

KLOE Analysis	$\Delta a_\mu^{\pi\pi}(0.35 - 0.85\ \text{GeV}^2) \times 10^{-10}$
this work	$376.6 \pm 0.9_{\text{stat}} \pm 2.4_{\text{exp}} \pm 2.3_{\text{theo}}$
KLOE08 [6]	$379.6 \pm 0.4_{\text{stat}} \pm 2.4_{\text{exp}} \pm 2.2_{\text{theo}}$

The experimental systematic precision reached in the overlapping range of $(M_{\pi\pi}^0)^2$ is comparable in both measurements. The systematic effects are independent in the two cases except for the uncertainties related to the radiator function, the vacuum

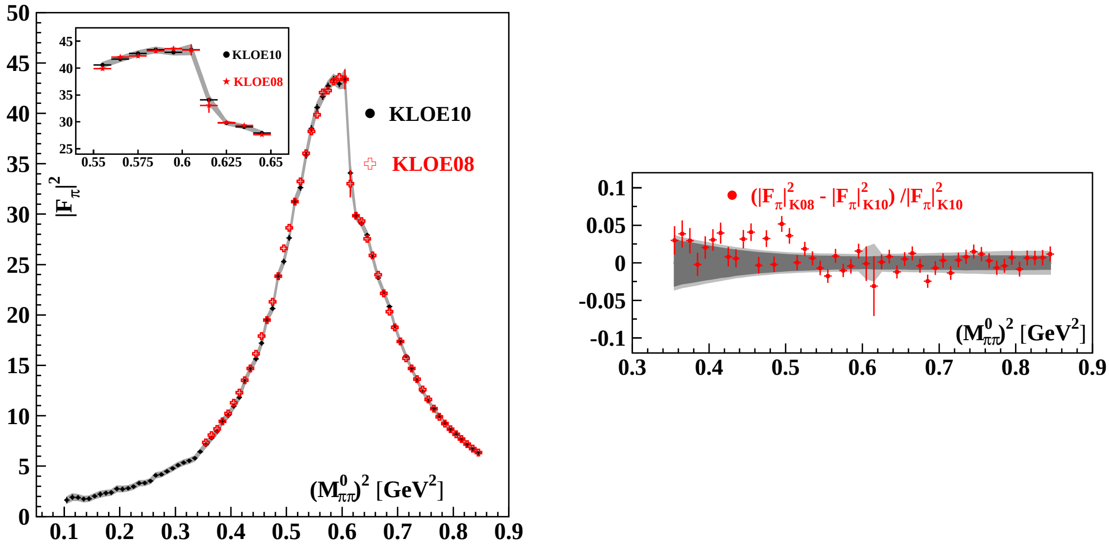

Figure 75: Left: Pion form factor $|F_\pi|^2$ obtained in the present (KLOE10, this work) and the previous (KLOE08, [6]) analyses. KLOE10 data points have statistical error attached, the grey band gives the combined statistical and systematic uncertainty (added in quadrature). Right: Fractional difference between $|F_\pi|^2$ from the KLOE08 and the KLOE10 analysis. The band in dark grey represents the statistical error of the KLOE10 result, the band in lighter grey gives the combined statistical and systematic uncertainty. In both figures, errors on KLOE08 points contain the combined statistical and systematic uncertainty.

polarization and the luminosity measurement, which are identical. The statistical uncertainty is larger in the present analysis due to the reduction of a factor 5 in statistics caused by the different cuts in acceptance.

Constructing the weighted average of the two measurements we evaluate the dispersion integral from 0.1 to 0.95 GeV^2, using the method of [45]. Separating out the uncertainties common to both measurements, we obtain

$$\Delta a_\mu^{\pi\pi}(0.1 - 0.95\ \text{GeV}^2) = (488.6 \pm 5.3_{\text{indep.}} \pm 2.9_{\text{common}}) \times 10^{-10}\ . \qquad (46)$$

The combined fractional total error of $\Delta a_\mu^{\pi\pi}$ in this range is 1.2%.

7 Comparison with results from the CMD-2, SND and BaBar experiments

The new KLOE result can be compared with the results from the energy scan experiments CMD-2 [46, 47] and SND [48] in Novosibirsk and the radiative return result obtained from the Babar experiment at SLAC [51]. In the comparisons, whenever there are several data points falling in one KLOE bin of $\Delta M^2_{\pi\pi} = 0.01$ GeV^2, their values are statistically averaged. Fig. 76, left, shows the comparison of $|F_\pi|^2$ obtained by the CMD-2 and SND collaborations with the new KLOE result. While on the ρ-peak and above, the new result is lower than the Novosibirsk results (confirming the discrepancy already present in the previous KLOE publication [6]), below the ρ-peak the three experiments show a good agreement within uncertainties. For

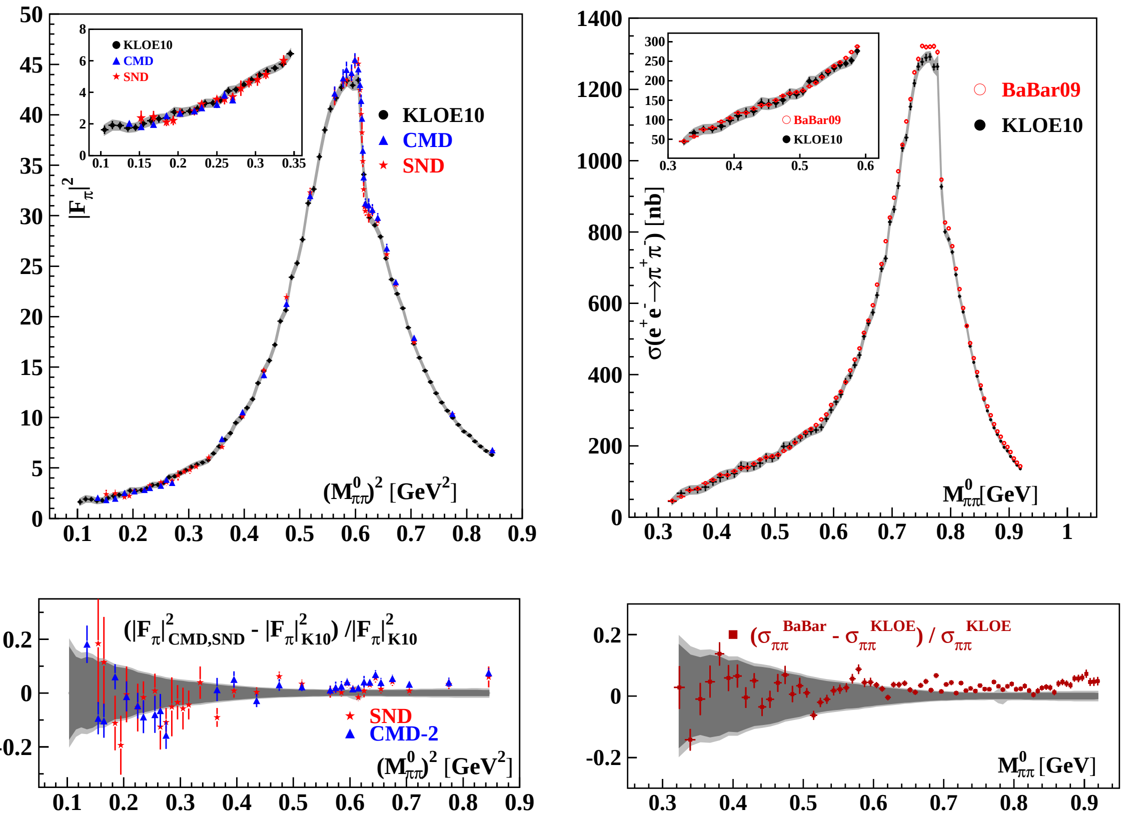

Figure 76: Upper left: $|F_\pi|^2$ from CMD-2 [46, 47], SND [48] and the new KLOE result. Lower left: Fractional difference between CMD-2 or SND and the new KLOE result. Upper right: $\sigma_{\pi\pi}^{\rm bare}$ from BaBar [51] and the new KLOE result. Lower right: Fractional difference between BaBar and the new KLOE result. CMD-2, SND and BaBar data points have the combined statistical and systematic uncertainty attached. The grey band in the upper plots contains combined statistical and systematic uncertainty of the new KLOE result. The dark (light) band in the lower plots shows statistical (combined statistical and systematic) error of the new KLOE result.

the comparison with the BaBar result, one needs to compare the bare cross sections $\sigma^{\mathrm{bare}}_{\pi\pi}$. This is shown in Fig. 76, right, as a function of $M^0_{\pi\pi}$ (KLOE bins of 0.01 GeV^2 have been converted transforming the upper and lower edges of the bin to values of $M^0_{\pi\pi}$). It can be seen that the new KLOE measurement lies systematically lower by 2-3 percent in the full range of $M^0_{\pi\pi}$. Below 0.6 GeV, the statistical uncertainties are large and and the two data sets agree within errors.

In the range between 0.630 and 0.958 GeV, the evaluation of the dispersion integral for the combined data set of the KLOE08 and KLOE10 can be compared with the results from the CMD-2 and SND experiments:

Experiment	$\Delta a^{\pi\pi}_\mu(0.630 - 0.958\ \mathrm{GeV}) \times 10^{-10}$
KLOE (comb.)	356.4 ± 2.7
KLOE08 [6]	356.7 ± 3.1
CMD-2, 2007 [46]	361.5 ± 3.4
SND, 2006 [48]	361.0 ± 5.1

As expected, the value using the combined KLOE data is very close to the one using the KLOE08 data, with a reduced total error. The 5 times larger statistics in the KLOE08 experiment pulls the value towards the KLOE08 result. All values are in agreement with each other.

8 Conclusions

We have measured the differential radiative cross section $\mathrm{d}\sigma(e^+e^- \to \pi^+\pi^-\gamma)/\mathrm{d}M^2_{\pi\pi}$ in the interval $0.1 < M^2_{\pi\pi} < 0.85$ GeV^2 using 230 pb^{-1} of data obtained while the DAΦNE e^+e^- collider was running at $W \simeq 1$ GeV, 20 MeV below the ϕ-meson peak. A systematic uncertainty of 1% has been reached above 0.4 GeV^2, rising up to 10% when approaching 0.1 GeV^2. This increase is mainly due to the uncertainty in the production mechanism of ϕ radiative decays and the uncertainty on the treatment of final state radiation.

From this measurement, we have extracted the squared modulus of the pion form factor in the time-like region, $|F_\pi|^2$, and the bare cross section for the process $e^+e^- \to \pi^+\pi^-$, $\sigma^{\mathrm{bare}}_{\pi\pi}$, in intervals of 0.01 GeV^2 of $(M^0_{\pi\pi})^2$, the squared mass of the virtual photon produced in the e^+e^--collision after the radiation of a hard photon in the initial state. Our new measurement is in good agreement with previous KLOE measurements, and reaches down to the dipion production threshold. A reasonable agreement has also been found with the results from the Novosibirsk experiments CMD-2 and SND, especially at low values of $(M^0_{\pi\pi})^2$. Comparing our result with the new result from the BaBar collaboration, we have found agreement within errors below 0.4 GeV^2, while above the BaBar result is higher by 2-3%.

Evaluating the dispersion integral for the dipion contribution to the muon magnetic moment anomaly, $\Delta a^{\pi\pi}_\mu$, in the range between 0.1 and 0.85 GeV^2 we have found

$$\Delta a^{\pi\pi}_\mu(0.1 - 0.85\ \mathrm{GeV}^2) = (478.5 \pm 2.0_{\mathrm{stat}} \pm 5.0_{\mathrm{exp}} \pm 4.5_{\mathrm{th}}) \times 10^{-10},$$

confirming the discrepancy between the SM evaluation for a_μ and the experimental value measured by the Muon g-2 collaboration at BNL.

Combining our result with the previous KLOE results, we have calculated $\Delta a_\mu^{\pi\pi}$ in the range $0.1 < M_{\pi\pi}^2 < 0.95$ GeV^2 obtaining

$$\Delta a_\mu^{\pi\pi}(0.1 - 0.95 \text{ GeV}^2) = (488.6 \pm 6.0) \times 10^{-10}.$$

The KLOE experiment covers $\sim 70\%$ of the leading order hadronic contribution to the muon anomaly with $\sim 1\%$ total error.

Note: $\sigma_{\pi\pi}^{\text{bare}}$ *has been evaluated using the parameterization for the* $\alpha(0)/\alpha(s')$ *given in [36]. A newer version of this parameterization (see [59]) gives values for* $\alpha(0)/\alpha(s')$ *which are higher by up to* 1.5% *in the region between* $0.6 - 0.95$ *GeV*^{2}*. This in turn leads to a reduction of our* $\sigma_{\pi\pi}^{\text{bare}}$*, and consequently our evaluations of* $\Delta a_\mu^{\pi\pi}$ *using KLOE data for* $\sigma_{\pi\pi}^{\text{bare}}$ *in the dispersion integral in Eq. 44 are reduced by* $0.7 - 0.8 \times 10^{-10}$*, depending on the energy range considered.*

Appendix: Fit of the pion form factor $|F_\pi|^2$

We perform a fit of the pion form factor in Table 5 using a model described in [55] in which the form factor is described as a sum of Breit-Wigner resonances:

$$F_\pi(s) = \sum_{n=0}^{\infty} c_n BW_n(s) \tag{47}$$

To account for the isospin-violating effect from the ω-meson, a $\rho - \omega$ mixing term is added to the ρ-contribution with $n = 0$:

$$F_\pi^{(\rho)}(s) = \frac{c_0 BW_0(s)}{1 + c_\omega}(1 + c_\omega BW_\omega) \tag{48}$$

For the $BW_n(s)$, two different parameterizations are used, one taken from [56]:

$$BW_\rho^{KS}(s) = \frac{m_\rho^2}{m_\rho^2 - s - i\sqrt{s}\Gamma_\rho(s)}\,,\; \Gamma_\rho(s) = m_\rho^2 \left(\frac{\sqrt{s - 4m_\pi^2}}{\sqrt{m_\rho^2 - 4m_\pi^2}}\right)^3 \frac{\Gamma_\rho}{s} \tag{49}$$

and one from [57]

$$BW_\rho^{GS}(s) = \frac{m_\rho^2(1 + d \cdot \Gamma_\rho/m_\rho)}{m_\rho^2 - s + f(s, m_\rho, \Gamma_\rho) - i m_\rho \Gamma_\rho(s)}\,,\; \Gamma_\rho(s) = \Gamma_\rho \left(\frac{\sqrt{s - 4m_\pi^2}}{\sqrt{m_\rho^2 - 4m_\pi^2}}\right)^3 \frac{m_\rho^2}{s} \tag{50}$$

with d and $f(s, m_\rho, \Gamma_\rho)$ described in [58].

We consider only terms up to $n = 3$ in the fit, and neglect the infinite tail of $n > 3$ states. We therefore do not constrain the absolute normalization of the c_i. The parameters fitted are M_ρ, Γ_ρ, M_ω, Γ_ω, c_0, c_1 and c_ω. All other parameters are fixed to the values found in [55].

We perform the fit using only the statistical error given in Table 5, and neglect the effects from the correlation of the error between bins parameterized in the covariance matrix in [37]. Figs. 77 and 78 show the result of the fit with the two different BW-parameterizations. We obtain the following parameters:

	KS	GS	PDG [12]
χ^2/d.o.f.	68.1/78	68.3/78	-
m_ρ [MeV]	775.0 ± 0.4	775.9 ± 0.4	775.49 ± 0.34
Γ_ρ [MeV]	148.4 ± 0.5	149.8 ± 0.5	149.1 ± 0.8
m_ω [MeV]	782.6 ± 0.3	782.6 ± 0.3	782.65 ± 0.08
Γ_ω [MeV]	10.1 ± 1.0	10.5 ± 1.0	8.49 ± 0.08
c_0	1.192 ± 0.002	1.097 ± 0.002	-
c_1	-0.133 ± 0.009	-0.096 ± 0.009	-
c_ω	0.00176 ± 0.00013	0.00180 ± 0.00013	-
$m_{\rho'}$ [MeV]	1357 (fixed)	1380 (fixed)	1465 ± 25
$\Gamma_{\rho'}$ [MeV]	437 (fixed)	340 (fixed)	400 ± 60
$m_{\rho''}$ [MeV]	1700 (fixed)	1700 (fixed)	1720 ± 20
$\Gamma_{\rho''}$ [MeV]	240 (fixed)	240 (fixed)	250 ± 50
$m_{\rho'''}$ [MeV]	2040 (fixed)	2040 (fixed)	-
$\Gamma_{\rho'''}$ [MeV]	400 (fixed)	400 (fixed)	-
c_2	0.00115 (fixed)	0.0216 (fixed)	-
c_3	-0.0438 (fixed)	-0.0309 (fixed)	-

Table 8: Parameters obtained in the fit of the pion form factor. Parameters marked as "fixed" were taken from [55] as input to the fitfunction.

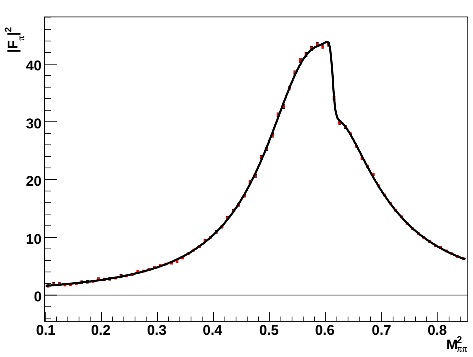

(a)

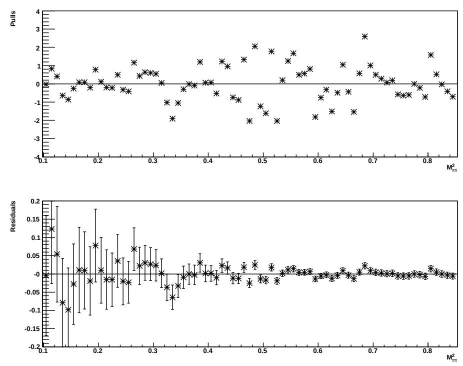

(b)

Figure 77: (a) Fit of the pion form factor with a KS-parameterization (b) Pulls and residuals for the fit of the pion form factor with a KS-parameterization.

Excellent agreement within the statistical error is found for both parameterizations, indicated by the χ^2-probability of about 80%. While the values for m_ρ, Γ_ρ and m_ω agree very well with the values of [12], the value for Γ_ω found in the fit is up to 2σ larger than the one in [12].

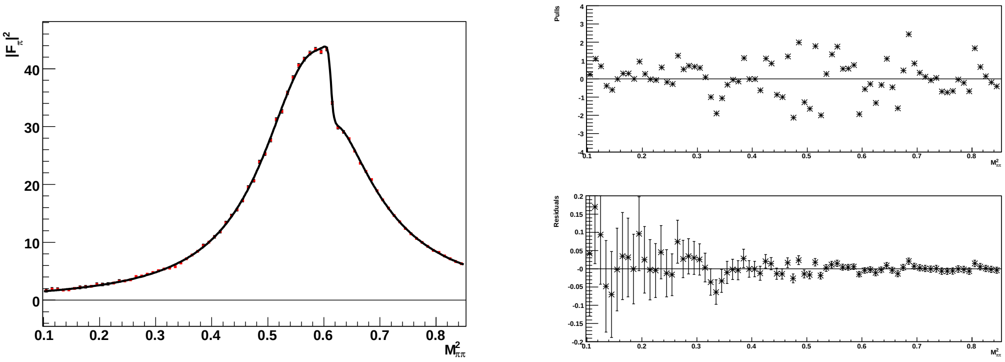

(a) (b)

Figure 78: (a) Fit of the pion form factor with a GS-parameterization (b) Pulls and residuals for the fit of the pion form factor with a GS-parameterization.

An important result of this simple fit is the perfect agreement of the mass of the ω meson with the PDG value, providing a valid cross check of the energy calibration of the KLOE detector.

Acknowledgements

We would like to thank our referees, Cesare Bini, Juliet Lee-Franzini and Graziano Venanzoni, for countless stimulating input and support.

References

[1] G. W. Bennett *et al.* [Muon G-2 Collaboration], Phys. Rev. D **73** (2006) 072003

[2] F. Jegerlehner and A. Nyffeler, Phys. Rept. **477** (2009) 1

[3] M. Davier, A. Hoecker, B. Malaescu, C.Z. Yuan and Z. Zhang, Eur. Phys. J. C **66** (2010) 1

[4] S. Actis *et al.*, Eur. Phys. J. C **66** (2010) 585

[5] F. Ambrosino et al. [KLOE collaboration], "Measurement of $\sigma(e^+e^- \to \pi^+\pi^-\gamma)$ and extraction of $\sigma(e^+e^- \to \pi^+\pi^-)$ below 1 GeV with the KLOE detector", Phys. Lett. B **606**, 12 (2005)

[6] F. Ambrosino et al. [KLOE collaboration], "Measurement of $\sigma(e^+e^- \to \pi^+\pi^-\gamma(\gamma))$ and the dipion contribution to the muon anomaly with the KLOE detector", Phys. Lett. B **670**, 285 (2009)

[7] S. Binner, J. H. Kühn and K. Melnikov, Phys. Lett. B **459** (1999) 279

[8] P. Beltrame, "Measurement of the Pion Form Factor via Radiative Return for data taken at $\sqrt{s} = 1$ GeV with the KLOE detector, PhD thesis (Universität Karlsruhe), IEKP-KA/2009-8

[9] M. Adinolfi *et al.* [KLOE Collaboration], Nucl. Instrum. Meth. A **488** (2002) 51

[10] M. Adinolfi *et al.* [KLOE Collaboration], Nucl. Instrum. Meth. A **482** (2002) 364

[11] D. Leone, PhD thesis, KA-IEKP-2007-7 (2007)

[12] C. Amsler *et al.* [Particle Data Group], Phys. Lett. B **667** (2008) 1

[13] S. Müller, G. Venanzoni, KLOE Memo 305

[14] M. Adinolfi *et al.* [KLOE Collaboration], Nucl. Instrum. Meth. A **492** (2002) 134

[15] B. Valeriani, PhD thesis, KA-IEKP-2005-14 (2005)

[16] F. Nguyen, *KLOE Memo* **294** (2004)

[17] R. Brun et al., *CERN Program Library Y250* (1995)

[18] R. Barlow and C. Beeston, *Comp. Phys. Comm.* **77**, 219 (1993)

[19] S. Baker and D. Cousins, *Nucl. Inst. Meth.* **221**, 437 (1984)

[20] O. Shekhovtsova et al., private commnication

[21] S. Giovanella, S. Miscetti, KLOE Note 213 (2006) and private comm.

[22] S. Müller, *Messung des Wirkungsquerschnitts* $\sigma(e^+e^- \to \pi^+\pi^-)$ *mit dem KLOE Detektor*, PhD Thesis, Universität Karlsruhe (TH) (2004), IEKP-KA/2004-20

[23] M. Moulson and S. Müller, *KLOE Memo* **288** (2004)

[24] M. Adinolfi et al. [KLOE collaboration], Nucl. Instrum. Meth. A 492 (2002) 134

[25] G. D'Agostini, *Nucl. Instrum. Meth. A* **362**, 487 (1995)

[26] G. D'Agostini, URL `http://www.roma1.infn.it/dagos/bayes_distr.txt`

[27] C. Gatti, M. Palutan and T. Spadaro, *KLOE Note* **209** (2004)

[28] H.Czyż et al., private communication

[29] F. Ambrosino *et al.* [KLOE coll.], Eur. Phys. J. C **47** (2006) 589

[30] C. M. Carloni Calame *et al.*, Nucl. Phys. B **584** (2000) 459

[31] F. Ambrosino *et al.* [KLOE coll.], Nucl. Instrum. Meth. A **534** (2004) 403.

[32] G. Balossini *et al.*, Nucl. Phys. B **758** (2006) 227

[33] S. Binner, J.H. Kühn and K. Melnikov, *Phys. Lett. B* **459**, 279 (1999)

[34] H. Czyż, A. Grzelińska, J. Kühn, G. Rodrigo, *Eur. Phys. J. C* **27**, 563 (2003)

[35] A. Höfer, J. Gluza and F. Jegerlehner, *Eur. Phys. Jour. C* **24**, 51 (2002)

[36] $\Delta\alpha_{\rm had}(s)$ values are kindly provided by F. Jegerlehner, `http://www-com.physik.hu-berlin.de/~fjeger/alphaQEDn.uu` (2003)

[37] Data tables and covariance matrices: `http://www.lnf.infn.it/kloe/ppg`

[38] F. Ambrosino et al. (KLOE Coll.), *Phys. Lett. B* **670**, 285 (2009)

[39] J.S. Schwinger, "Particles, Sources, and Fields. VOL. 3", *Redwood City, USA: ADDISON-WESLEY (1989) 318 P. (Advanced Book Classics Series)*

[40] O. Shekhovtsova, G. Venanzoni, G. Pancheri *Comput. Phys. Commun.* **180***, 1206 (2009)*

[41] S. Ivashyn, H. Czyż, A. Korchin *Acta Phys. Polon.* **B40***, 3185 (2009)*

[42] C. Unkmeir *et al.*, *Phys. Rev.* **D61***, 034002 (2000)*

[43] T. Fuchs *et al.*, *Czech. J. Phys.* **52***, B135 (2002)*

[44] F. Jegerlehner, Nucl. Phys. Proc. Suppl. **162** (2006) 22

[45] S. I. Eidelman and F. Jegerlehner, Z. Phys. C **67** (1995) 585.

[46] R. R. Akhmetshin et al. (CMD-2 Collaboration), *Phys. Lett. B* **648**, 28 (2007)

[47] R. R. Akhmetshin et al. [CMD-2 Coll.], *JETP Lett.* **84** 413 (2006)

[48] M. N. Achasov et al. (SND Coll.), *Jour. Exp. Theor. Phys.* **103**, 380 (2006)

[49] S. Brodsky and E. de Rafael, Phys. Rev. **168** (1968) 1620

[50] B. E. Lautrup and E. de Rafael, Nuovo Cimento **1A** (1971) 238

[51] B. Aubert *et al.* [BABAR Collaboration], Phys. Rev. Lett. **103** (2009) 231801

[52] K. Hagiwara et al, *Phys. Rev. B* **649**, 173 (2007)

[53] M. Passera, *Phys. Rev. D* **75**, 013002 (2007)

[54] A. Czarnecki, B. Krause and W.J. Marciano, *Phys. Lett. D* **52**, 2619 (1995)

[55] C. Bruch, A. Khodjamirian and J. H. Kuhn, Eur. Phys. J. C **39** (2005) 41

[56] J. H. Kuhn and A. Santamaria, Z. Phys. C **48** (1990) 445.

[57] G. J. Gounaris and J. J. Sakurai, Phys. Rev. Lett. **21** (1968) 244.

[58] R. R. Akhmetshin *et al.* [CMD-2 Collaboration], Phys. Lett. B **527** (2002) 161

[59] $\Delta\alpha_{\rm had}(s)$ values by F. Jegerlehner, `http://www-com.physik.hu-berlin.de/~fjeger/alphaQED.tar.gz` (2010)